Inaugural dissertation

for

obtaining the doctoral degree

of the

Combined Faculty of Mathematics, Engineering and Natural Sciences

of the

Ruprecht - Karls - University

Heidelberg

Presented by

Yannick Stahl, M.Sc.

born in Alfeld (Leine), Germany

Oral examination 28.03.2025

Meta-analysis of genome-wide CRISPR screenings reveals host dependency and restriction factors of the SARS-CoV-2 replication cycle

Referees: Prof. Dr. Dr. Ralf Bartenschlager

Prof. Dr. Michael Boutros

Acknowledgements

During my Ph.D., I received generous support from colleagues, friends, and family who taught me invaluable lessons, helped me through challenging times, and made this journey memorable. This paragraph is dedicated to them.

First, I want to thank Dr. Ralf Bartenschlager, who has mentored me closely during this journey and taught me the essence of being a virologist. The most valuable lesson I have learned from Ralf is what I refer to as “thinking like a virus”. Even though this statement is biologically speaking more than inaccurate, Ralf has taught me how to rationally interpret my experimental results, creatively design experiments, think of necessary controls and most importantly to put scientific insights into a greater context and question their meaning and relevance. *Thank you for everything you gave me on the way, Ralf!* Second, I want to thank Dr. Berati Cerikan, who taught me essential technical skills and conducted the CRISPR/Cas9 screenings fundamental to my dissertation. Our shared perspectives have made him a close friend. *Thank you for every lesson you have taught me, Berati!*

The project presented within this dissertation would not have been possible without the active support of many collaborators. The CRISPR/Cas9 screenings that laid the foundation for this project were analyzed in the laboratory of Dr. Michael Boutros. Therefore, I would like to thank Dr. Michael Boutros, Dr. Luisa Henkel, and Dr. Florian Heigwer for their ongoing efforts to support this project and my scientific development. I would also like to thank the laboratory of Dr. Oliver Fackler for the repeated help during the course of this project. *Collaborating with you has been highly instructive and pleasant!*

I also want to extend my gratitude to many other collaborators that I had the chance to support during my time in Heidelberg. This includes the group of Dr. Christoph Dieterich. It was a pleasure to work with Dr. Shirin Doroudgar, Dr. Maja Bencun, and Dr. Etienne Boileau and I have learned many valuable lessons from these collaborations. In addition, I had the opportunity to support the group of Dr. Johan Neyts at KU Leuven. This was the first time I had the chance to dive into antiviral drug development and the experience and skills of Johan and his group have made this time truly meaningful. Therefore, I would like to thank Dr. Johan Neyts, Dr. Manon Laporte and Dr. Dirk Jochmans for this exciting opportunity. A third collaboration with the lab of Dr. Britta Brügger allowed me to explore the world of lipids and study their relevance for viral infections. In the light of this I would like to extend my gratitude to Dr. Britta Brügger

and Rosangela Silva Santos. *I have truly enjoyed working with all of you and hope that our paths will cross again in the future.*

Doing a Ph.D. can be challenging and it will be even more challenging without a network of support provided by colleagues. Fortunately, I joined a lab with incredible colleagues, many of which have become dear friends over the past few years. I therefore want to thank all past and present members of the Bartenschlager lab, the Department of Molecular Virology, and the Division of Virus-associated Carcinogenesis at the German Cancer Research Center. During the countless times I was in the need of help, I do not recall a single time that I was turned down by anyone in our department. I would also like to express my gratitude to the members of my thesis advisory committee, Dr. Viet Loan Dao Thi and Dr. Steeve Boulant that have guided my research throughout the past years. In addition, I want to thank Dr. Frauke Mücksch for agreeing to participate in my defense committee. I also want to mention a couple of colleagues that have conquered a special place in my heart: Alessandro Manetto, Leon Hennecke, Alina Rosinski, Philipp Ralfs, Teresa Lavacca, Dominik Kiemel, and Samy Sid Ahmed. *You have repeatedly proven to be true friends that I can rely on at all times.* Furthermore, I want to mention the group of people that keeps this department running. This includes the excellent administrative support provided by Pilar Milla, Dr. Sandra Bühler, Fredy Huschmand, Dr. Ilka Rebhan, and Dr. Katrin Woll. In addition, I want to thank Marie Bartenschlager, Ulrike Herian, Sabine Scholl and Uta Haselmann for the unmatched technical support in the lab.

I also want to mention my family that has supported my journey ever since. Most importantly this includes my parents Marjana and Dirk Stahl. I lack the words to express my gratitude to my brother, Bojan Stahl, who has been a bottomless well of support throughout my entire life. This likely would not have been possible without my brothers family. Therefore, I would like to thank Mila Stahl and Vesna Marković-Stahl. My grandmother, Zorka Ivković, has taught me the value of family and friendship. Finally, I also want to thank the family of my wife that has become a part of my own family during the time I have been working on this project. *I am extremely grateful to have you and will never be able to find the right words to thank you for everything you have done for me. Hvala vam što ste me uvijek podržavali i što ste uvijek bili tu za mene.* Special thanks also to my lifelong friends Julian Scholt, Fabio Schaper, Giorgia Mannella, Johannes Schwarze, and Merlin Scherff. *Without you I would not have had the strength and confidence to follow my dreams.*

Lastly, my deepest gratitude to my wife, Iva Stahl, for her unconditional love and support. *I look forward to what our common future holds in store for us.*

Summary

SARS-CoV-2, the etiologic agent that causes COVID-19, remains a global threat to public health. Understanding the complex interplay between SARS-CoV-2 and its host cell is fundamental to identify novel targets for antiviral or anti-inflammatory therapy. Being provided with two genome-scale CRISPR/Cas9 loss-of-function screenings that were performed in the lung epithelial cell lines A549-ACE2 and Calu-3, I set out to identify analogies between the loss-of-function screenings conducted in our laboratory and previously published screenings that were performed in other cellular models of infection. The rationale behind this approach was to determine which host cell factors have conserved functions during SARS-CoV-2 infection in a variety of cell lines and might therefore be physiological contributors to SARS-CoV-2 propagation and pathogenesis. I employed thresholding to identify factors that exhibited proviral function in all of the six analyzed loss-of-function screenings.

This approach yielded 24 potential host cell factors of which angiotensin converting enzyme 2 (ACE2), the primary receptor of SARS-CoV-2, showed the highest average enrichment, validating this approach. The remaining 23 factors have not been described in the context of SARS-CoV-2 infection so far. Due to its interesting location in the late endosome and its prominent involvement in membrane trafficking and endosome biogenesis, I selected RAB9A for detailed validation and mechanistic investigation. In addition, TIMM17B, an integral component of the TIM23 complex that imports presequence containing proteins into the mitochondrial matrix, was validated. RAB9A supported SARS-CoV-2 infection in a variety of cell lines and using a variety of virus isolates. As evidenced by a reduction of SARS-CoV-2 infection of cells depleted of the RAB9A guanine nucleotide exchange factor DENND2D, RAB9A's proviral activity seems to require the conversion of its inactive GDP-bound form to active GTP-bound RAB9A. Furthermore, and in line with previous reports, RAB9A depletion resulted in morphological changes of the cellular lysosome population, confirming an involvement of RAB9A in endo-lysosome biogenesis. Interestingly, ectopic expression of the host protease TMPRSS2 that is required for SARS-CoV-2 entry at the plasma membrane mitigated the observed reduction in SARS-CoV-2 infection in RAB9A-depleted cells, indicating a specific involvement of RAB9A during endocytic entry, which can proceed in the absence of TMPRSS2 and instead requires the endosomal activity of cathepsin proteases. This assumption was confirmed by means of propagation-deficient vesicular stomatitis virus pseudotypes. Consistently, RAB9A depletion increased SARS-CoV-2 uptake, followed by a retention of virions in the late endosomal and lysosomal compartment, likely indicating deficits

in the initiation of fusion during entry. The relevance of RAB9A for the fusion of SARS-CoV-2 with membranes of the late endosome was confirmed employing lentiviral pseudotypes.

Interestingly, the second host cell factor identified in the meta-analysis, TIMM17B, does not support but significantly suppress SARS-CoV-2 infection in A549-ACE2 and Calu-3 lung epithelial cells, arguing that it is a restriction factor. It remains unclear how TIMM17B-targeting sgRNAs became enriched in all six analyzed loss-of-function screenings. Mechanistic follow-up studies show that TIMM17B is most likely involved in the early stages of the viral life cycle. However, the enhancement of entry in the absence of TIMM17B is very moderate, suggesting that TIMM17B might restrict other steps of SARS-CoV-2 replication. Further investigation will be necessary to address this question.

In summary, by integrating the results of various CRISPR/Cas9 screenings I was able to identify RAB9A as a SARS-CoV-2 dependency factor that supports fusion during entry into various cellular models. In addition, TIMM17B was identified to be a SARS-CoV-2 restriction factor affecting, at least in part, the early stages of the viral life cycle. The meta-analysis approach used here will aid to identify relevant host cell factors and reduce the number of false-positive hits caused by technical or cell line specific artifacts.

Zusammenfassung

SARS-CoV-2, der Erreger, der COVID-19 verursacht, bleibt eine globale Bedrohung für die öffentliche Gesundheit. Das Verständnis der komplexen Wechselwirkungen zwischen SARS-CoV-2 und seiner Wirtszelle ist grundlegend, um neue Angriffspunkte für antivirale oder entzündungshemmende Therapien zu identifizieren. Nachdem mir die Ergebnisse zweier genomweiter CRISPR/Cas9 Knockout-Screenings bereitgestellt wurden, die in unserem Labor in den Lungenepithelzelllinien A549-ACE2 und Calu-3 durchgeführt wurden, verfolgte ich das Ziel, Analogien zwischen diesen Screenings aus unserem Labor und zuvor veröffentlichten Screenings zu identifizieren, die in anderen zellulären Infektionsmodellen durchgeführt wurden. Die rationale Grundlage dieses Ansatzes war herauszufinden, welche Wirtszellfaktoren während einer SARS-CoV-2 Infektion in verschiedenen Zelllinien konservierte Funktionen aufweisen und daher physiologische Beiträge zur Vermehrung und Pathogenese von SARS-CoV-2 leisten könnten. Durch das Setzen von Schwellenwerten identifizierte ich Faktoren, die in allen sechs analysierten Knockout-Screenings eine provirale Funktion zeigten.

Dieser Ansatz ergab 24 potenzielle Wirtszellfaktoren, von denen das Angiotensin-konvertierende Enzym 2 (ACE2), der primäre Rezeptor von SARS-CoV-2, die höchste durchschnittliche Anreicherung in infizierten Zellen zeigte und damit diesen Ansatz validierte. Die übrigen 23 Faktoren wurden bislang nicht im Zusammenhang mit SARS-CoV-2 Infektionen beschrieben. Aufgrund der interessanten Lokalisation im späten Endosom und der prominenten Rolle im Membrantransport sowie bei der Endosomen Biogenese wählte ich RAB9A für detaillierte Validierungen und mechanistische Untersuchungen aus. Außerdem wurde TIMM17B, eine integrale Komponente des TIM23 Komplexes, der für den Import von Präsequenz-enthaltenden Proteinen in die mitochondriale Matrix verantwortlich ist, im Kontext der SARS-CoV-2 Infektion validiert. RAB9A unterstützte die SARS-CoV-2 Infektion in verschiedenen Zelllinien und mit verschiedenen Virusisolaten. Wie durch die reduzierte Infektion von Zellen, denen der RAB9A-spezifische Guaninnukleotidaustauschfaktor DENND2D fehlte, belegt wurde, scheint die provirale Aktivität von RAB9A die Umwandlung seiner inaktiven GDP-gebundenen Form in die aktive GTP-gebundene Form zu erfordern. Darüber hinaus führte, wie bereits in der Literatur beschrieben, der Verlust von RAB9A zu morphologischen Veränderungen in der Lysosomen Population der Zelle, was eine Rolle von RAB9A bei der Endo-Lysosomen-Biogenese bestätigt. Interessanterweise verhinderte die ektopische Expression der Wirts-Protease TMPRSS2, die für den Eintritt von SARS-CoV-2 an der Plasmamembran erforderlich ist, die beobachtete Reduktion der Infektion in RAB9A-

depletierten Zellen. Dies deutet auf eine spezifische Rolle von RAB9A während des endozytischen Zelleintritts hin, der in Abwesenheit von TMPRSS2 stattfinden kann und stattdessen die endosomale Aktivität von Cathepsin-Proteasen erfordert. Diese Annahme wurde durch den Einsatz von propagationsdefizienten Pseudotypen des Vesikulären Stomatitis-Virus (VSV) bestätigt. Die Depletion von RAB9A erhöhte die Aufnahme von SARS-CoV-2, gefolgt von einer Retention der Virionen im späten endosomalen und lysosomalen Kompartiment, was auf Defizite bei der Initiation der Fusion während des Zelleintritts hinweist. Die Relevanz von RAB9A für die Fusion von SARS-CoV-2 mit den Membranen des späten Endosoms wurde durch den Einsatz von lentiviralen Pseudotypen bestätigt.

Überraschenderweise hat eine Validierung eines zweiten Wirtszellfaktors, der durch die Meta-Analyse identifiziert wurde, TIMM17B, gezeigt, dass TIMM17B den SARS-CoV-2 Lebenszyklus nicht unterstützt, sondern inhibiert, was darauf hindeutet, dass TIMM17B ein Restriktionsfaktor ist. Es bleibt dabei jedoch zunächst unklar, wie TIMM17B sgRNAs trotz antiviraler Aktivität TIMM17Bs in den sechs Knockout-Screenings angereichert werden konnten. Mechanistische Untersuchungen deuten darauf hin, dass TIMM17B in frühe Phasen des viralen Lebenszyklus involviert ist. Allerdings ist der Anstieg des Zelleintritts in der Abwesenheit TIMM17Bs sehr moderat, sodass es möglich erscheint, dass TIMM17B auch andere Phasen des SARS-CoV-2 Replikationszyklus hemmt. Weitere Experimente werden nötig sein um diese Frage zu beantworten.

Durch die Integration der Ergebnisse verschiedener CRISPR/Cas9 Screenings war ich dazu in der Lage RAB9A als Wirtszellfaktor zu identifizieren, der die Fusion während des Zelleintritts in verschiedene Zelllinien unterstützt. Außerdem wurde TIMM17B als SARS-CoV-2 Restriktionsfaktor identifiziert, der zumindest teilweise frühe Ereignisse des viralen Lebenszyklus inhibiert. Die Herangehensweise der Meta-Analyse solcher Datensätze, die in dieser Studie verwendet wurde, wird es erleichtern relevante Wirtszellfaktoren zu identifizieren und die Zahlen von falsch-positiven Treffern zu reduzieren, die auf technische oder Zelllinien-spezifische Artefakte zurückzuführen sind.

Table of contents

List of figures

List of tables

List of abbreviations

Abbreviation	Meaning
ACE2	Angiotensin converting enzyme 2
APS	Ammonium peroxydisulfate
ARDS	Acute respiratory distress syndrome
BSA	Bovine serum albumin
cDNA	Complementary DNA
COVID-19	Coronavirus disease 2019
CTSB	Cathepsin B
CTSL	Cathepsin L
DMEM	Dulbecco's Modified Eagle Medium
DMV	Double membrane vesicle
E	Envelope protein
ER	Endoplasmic reticulum
FBS	Fetal bovine serum
FDR	False discovery rate
GAP	GTPase-activating protein
GEF	Guanine nucleotide exchange factor
GMEM	Glasgow's Minimum Essential Medium
HPV	Human papillomavirus
M	Membrane protein
M6PR	Mannose-6-phosphate receptor
MEM	Minimum Essential Medium
MERS-CoV	Middle East respiratory syndrome coronavirus
MOI	Multiplicity of infection
M^{pro}	Main protease
N	Nucleocapsid protein
NEAA	Non-essential amino acids
NPC1/2	Niemann-Pick disease, type C1/C2
NSP	Non-structural protein
NT	Non-targeting
ORF	Open reading frame
PEI	Polyethyleneimine
PFA	Paraformaldehyde
PL^{pro}	Papain-like protease
pURT	Pico units reverse transcriptase
PVDF	Polyvinylidene fluoride
S	Spike protein
SARS-CoV	Severe acute respiratory syndrome coronavirus

SARS-CoV-2	Severe acute respiratory syndrome coronavirus 2
SDS	Sodium dodecyl sulfate
SG-PERT	SYBR Green PCR-enhanced reverse transcriptase assay
siRNA	Small interfering RNA
TIM	Translocase of the inner membrane
TMPRSS2	Transmembrane serine protease 2
TOM	Translocase of the outer membrane
VOC	Variant of concern
VSV	Vesicular stomatitis virus
VSVΔG	Vesicular stomatitis virus with glycoprotein deletion (encoding GFP and FLuc)
WHO	World Health Organization

I. Introduction

I.1 Origin and emergence of SARS-CoV-2

In December 2019 an outbreak of pneumonia of unknown origin was observed in Wuhan, China[1]. The aetiologic agent causing this novel disease was identified as a coronavirus, which was later named Severe Acute Respiratory Syndrome Coronavirus 2 (SARS-CoV-2) due to its high similarity to SARS-CoV, which emerged in 2002[1–4]. SARS-CoV-2 is the third highly pathogenic coronavirus that emerged in the last 25 years. Besides the emergence of SARS-CoV in 2002[5], a subsequent outbreak of Middle East Respiratory Syndrome Coronavirus (MERS-CoV) followed in 2012 in Saudi Arabia[6]. SARS-CoV-2 is expected to originate from Asian *Rhinolophus* bats in which many closely related viruses were identified[7–11]. The initial cases that were observed in Wuhan clustered around the Huanan market in Wuhan, where live animals are traded[12–15], suggesting a zoonotic origin of the virus. This is furthermore supported by the observation of elevated antibody titers against SARS-like coronaviruses in animal traders in 2003[13,16]. In 2020 two bat coronaviruses with high sequence identity were detected in two Asian bat species, RaTG13 (96% identity) and RmYN02 (93.3% identity)[13,17,18]. In addition, multiple other SARS-CoV-2-like sequences were isolated from palm civets and pangolins in South-East Asia which may indicate the existence of an intermediate host that enabled the transmission of an ancestral SARS-CoV-2-like virus from the reservoir in bats to humans[19].

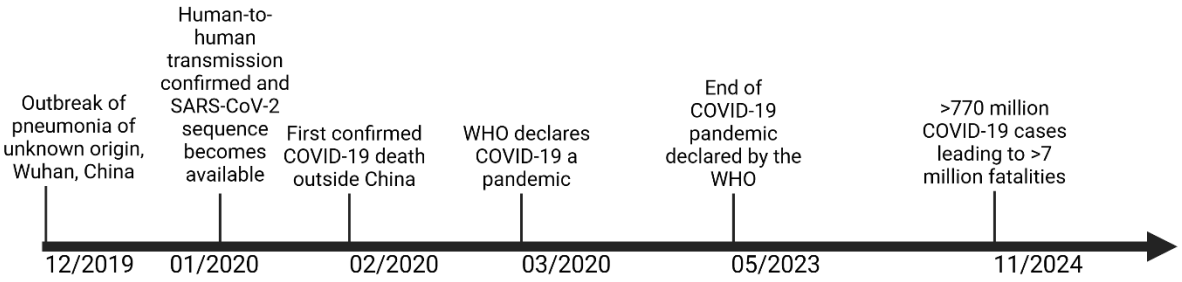

Figure 1: Timeline of the COVID-19 pandemic. Selected events are displayed. The data was obtained from the CDC Museum COVID-19 Timeline[20]. This timeline was created using BioRender.com.

After the emergence of SARS-CoV-2 in Wuhan, China, the virus spread readily throughout China and was detected in other countries shortly after. In January 2020 human-to-human transmission of SARS-CoV-2 was confirmed and the city of Wuhan was placed under lockdown[20]. In addition, the first coronavirus disease 2019 (COVID-19) cases outside China were reported by the health authorities of Thailand, Japan and the Republic of Korea[20]. By

March 2020, SARS-CoV-2 had caused more than 100,000 cumulative COVID-19 cases and was officially declared a pandemic by the World Health Organization (WHO)[1,20]. As of today (November 4th 2024), more than 770 million COVID-19 cases have been registered worldwide, leading to more than 7 million deaths[21]. While the first measures to control the COVID-19 pandemic were of non-pharmaceutical nature, the development of vaccines and antiviral drugs quickly commenced[22]. Through a global effort to reduce the spread of COVID-19 employing both, non-pharmaceutical interventions such as the wearing of masks and social distancing and large vaccination campaigns, the number of severe COVID-19 cases was markedly reduced by spring 2023. The COVID-19 pandemic was declared to be over by the WHO on May 5th 2023[23]. A representative timeline of selected events that occurred during the COVID-19 pandemic is shown in Figure 1. Currently, SARS-CoV-2 continues to circulate globally in an endemic manner, highlighting the need to advance scientific research on this important novel pathogen.

I.2 Pathogenesis of COVID-19

One of the key features that allowed SARS-CoV-2 to spread rapidly around the world was the possibility of airborne transmission by individuals that had not yet developed symptoms, which is commonly referred to as presymptomatic transmission[24]. Presymptomatic transmission prevents the successful isolation of infected individuals prior to the transmission to secondary patients and therefore complicates the design of measures that successfully interrupt transmission chains and the spread of the virus. As the virus replicates primarily in the upper and lower respiratory tract[25], it is mainly transmitted by the respiratory route either by airborne or droplet transmission[26,27]. The transmissibility of viruses can be measured by determining the reproduction number which describes the expected number of transmissions to susceptible individuals from one infected patient. For SARS-CoV-2, an increase in the transmissibility was observed with the emergence of novel variants of concern (VOC). While the VOC Alpha had a reproduction number of 1.22, Delta showed an increase to 1.38 and for Omicron isolates an even higher reproduction number of 1.9 was observed, emphasizing the adaptation of SARS-CoV-2 to human-to-human transmission[28]. A similar trend is observed in the secondary attack rate of SARS-CoV-2 that is a measure for the likelihood of transmission in the instance of certain exposure[29]. The secondary attack rate is usually determined in households in which one member was diagnosed as SARS-CoV-2 positive by tracking the transmission from this index patient to secondary patients. A relatively quick increase in the secondary attack rate of SARS-CoV-2 was observed early in the pandemic between January and July 2020 which correlates well with the emergence of the D614G mutation in the Spike protein (S) that enhances

transmissibility[29,30]. Smaller increases in the secondary attack rate were still evident after July 2020 that correlated with the emergence of novel SARS-CoV-2 VOCs[29].

Table 1: List of known COVID-19-associated medical complications and their likelihood of occurrence. These data were extracted from BMC Best Practice[31].

Complication	**Likelihood**
Post-intensive care syndrome	High
Thrombosis	High
Cardiovascular complications	High
Acute kidney injury	High
Post-COVID-19 syndrome	Medium
Post-COVID-19 vaccination: myocarditis/pericarditis	Medium
Acute liver injury	Medium
Neurologic complications	Medium
Cardiac arrest	Medium
Pregnancy-related complications	Medium
Sepsis/septic shock	Low
Disseminated vascular coagulation	Low
Acute respiratory failure	Low
Air leak	Low
Cytokine release syndrome	Low
Multisystem inflammatory syndrome in children (MIS-C)	Low
Post-COVID-19 vaccination: vaccine-induced immune thrombocytopenia and thrombosis (VITT) and other thromboembolic events	Low
Aspergillosis	Low
Mucormycosis	Low
Candidemia	Low
Pancreatic injury	Low
Immune thrombocytopenia	Low
Thyroid disorders	Low
Gastrointestinal complications	Low
Acute hair loss	Low
Lower urinary tract complications	Low
Parosmia	Low

COVID-19 is less lethal than previous highly pathogenic coronaviruses, such as SARS-CoV and MERS-CoV[32]. The case fatality rate of SARS-CoV infections was estimated to be around 11%[32]. An even higher case fatality rate between 26% and 35.8% was observed in patients infected with MERS-CoV[32]. COVID-19 resulted in a global case fatality rate of approximately 2.2%[32], but the pathogenicity of the recently emerged variants differs greatly and exhibits a trend to decreasingly severe infections[33]. COVID-19 mainly manifests in fever, cough, muscle soreness and fatigue[34]. Besides typical respiratory symptoms COVID-19 can include non-respiratory manifestations leading to neurological (e.g. loss of smell and taste) or gastrointestinal symptoms (e.g. diarrhea and vomiting)[35–38]. Under certain circumstances

COVID-19 can progress to a severe or life-threatening disease with complications affecting multiple organ systems[31]. A hallmark of severe COVID-19 is the acute respiratory distress syndrome (ARDS) that is evidenced by reduced respiratory rate and blood oxygen saturation and that can be life threatening or induce lasting pathological changes such as pulmonary fibrosis[39]. In contrast to common belief, pulmonary complications during COVID-19 are observed less frequently than cardiovascular complications (e.g. thromboembolic events and myocarditis), multi-organ involvement including liver and kidney injury, neurological manifestations (e.g. acute cerebrovascular disease, encephalitis and ataxia) or even viral sepsis[31,37,40–47]. An overview of the COVID-19-associated complications and their likelihoods can be found in Table 1. At the moment it is not fully understood if these widespread non-pulmonary manifestations during COVID-19 are a direct result of viral replication in the respiratory tract or other tissues or if the excessive release of proinflammatory cytokines during severe COVID-19 may induce dysfunction of other organ systems. Another possible explanation for the multi-organ manifestations might be thromboembolisms that are often observed in the context of COVID-19 that might restrict the blood circulation to other organs like kidney and liver[48]. There is evidence for active viral replication in non-respiratory tissues. For instance, SARS-CoV-2 RNA of negative polarity (an intermediate RNA species that can only be detected during active replication) was detected in the myocardium of patients with severe COVID-19[49]. In addition, gastrointestinal infection and the shedding of infectious virus in stool was reported to occur in COVID-19 patients[50]. Invasion of the central nervous system by SARS-CoV-2 was described in SARS-CoV-2 infected golden hamsters[38]. While the presence and activity of SARS-CoV-2 in these organ systems does not establish a causal link between replication in these tissues and the cardiological, neurological and gastrointestinal manifestations, a correlation between the susceptibility of these tissues and the clinical presentation is obvious. In addition to these acute manifestations, COVID-19 can progress to a chronic and highly heterogenous disease that is referred to as post-COVID-19 syndrome or long COVID[31]. Post-acute sequelae (also referred to as post-viral syndrome) after severe respiratory infection are not uncommonly observed after pneumonia of non-SARS-CoV-2 etiology or even non-respiratory viral infections[51]. Current evidence suggests an extremely high prevalence of post-acute sequelae after COVID-19 ranging from 20-25% of COVID-19 patients[47,52]. In summary, the clinical presentations of COVID-19 are extremely diverse and complicate the diagnosis and treatment guidance of COVID-19. The active replication of SARS-CoV-2 in extrapulmonary tissues, evidence of increased rates of thromboembolic events and the excessive release of proinflammatory cytokines indicate a multicausal pathogenesis of COVID-

19 during which different organ systems can be impacted by the numerous consequences of SARS-CoV-2 infection.

I.3 Molecular characteristics of SARS-CoV-2

SARS-CoV-2 is an enveloped positive sense RNA virus and belongs to the family of *Coronaviridae* and to the genus *Betacoronavirus*[53]. The viral particle contains four structural proteins: S, Membrane (M), Envelope (E) and Nucleocapsid (N)[53]. A schematic of a SARS-CoV-2 virion can be found in Figure 2 A. S is the viral glycoprotein responsible for the interaction with the host cell receptor of SARS-CoV-2, angiotensin converting enzyme 2 (ACE2)[54]. S occurs in homotrimers in the viral envelope that are formed during the viral assembly process[55]. During the viral life cycle, S undergoes two subsequent proteolytic cleavages[56]. The first proteolytic cleavage is performed in a polybasic cleavage site by the host protease furin at the S1/S2 boundary of S during egress, which was shown to enhance the infectivity of progeny virus[56]. The emergence of this polybasic cleavage site is a feature that differentiates SARS-CoV-2 from the previously emerged SARS-CoV and might explain the drastically enhanced transmissibility of SARS-CoV-2[56]. Upon proteolytic activation of S at the S2' site by either transmembrane serine protease 2 (TMPRSS2) or by cathepsin proteases in the late endosome, S can induce fusion of the viral envelope with host membranes, such as the plasma membrane or the membrane of the endosomal compartment[54]. The M protein is the most abundant protein present in the viral envelope and a key contributor to the *de novo* assembly of viral particles[57]. The E protein is the smallest structural protein of SARS-CoV-2 and might function as a viroporin, but the functional importance of E has not yet been fully elucidated[58]. N is the only non-structural protein that is not incorporated into the viral envelope. Instead, its primary function lies in the encapsidation of the genomic viral RNA and the antagonism of host interferon responses[59–61].

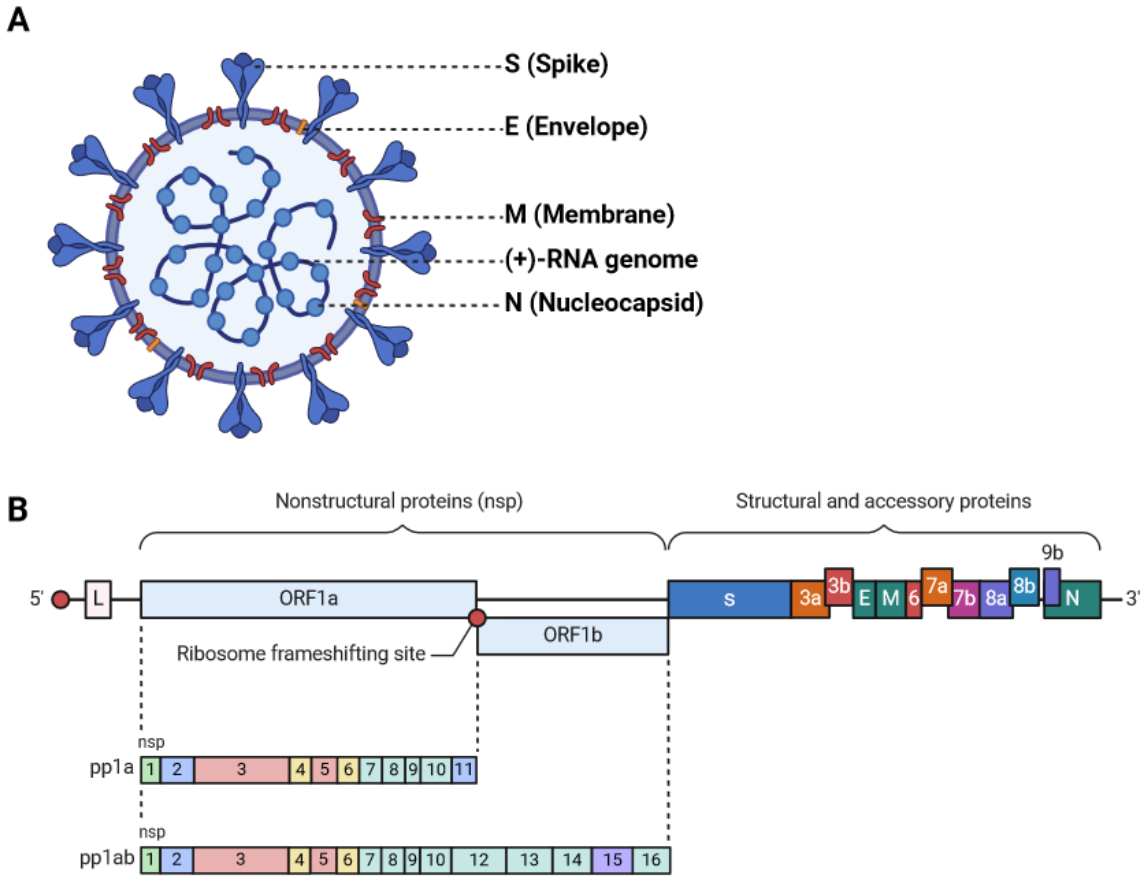

Figure 2: Virion structure and genome organization of SARS-CoV-2. A) A schematic overview of a SARS-CoV-2 virion. The structural proteins and the positive-sense RNA genome are highlighted. B) Genome organization of SARS-CoV-2. This schematic was created using BioRender.com.

The genome of SARS-CoV-2 is approximately 30 kb in length, of positive polarity and contains a 5'-cap and 3'-poly-A tail[62–64]. This genome encodes a total of 29 putative proteins, of which 25 are non-structural (NSP) and accessory proteins[64,65]. Approximately two thirds of the viral genome are occupied by the open reading frames (ORF) ORF1a and ORF1b encoding the replicase-transcriptase complex (NSP1-16) that is necessary for the initiation of genome replication and for the generation of subgenomic transcripts[64,65]. The remaining third of the viral genome encodes the four structural proteins and accessory proteins[64]. A schematic of the genome organization of SARS-CoV-2 is shown in Figure 2 B.

I.4 The life cycle of SARS-CoV-2

The SARS-CoV-2 life cycle is initiated by an interaction between the S1 domain of S in the viral envelope and its cellular receptor ACE2[54]. Upon receptor binding, SARS-CoV-2 can employ two distinct entry pathways to enter target cells[54,66]. In the presence of the host protease TMPRSS2, S is proteolytically activated at the S2' site by TMPRSS2 on the plasma membrane, enabling the direct fusion of the viral envelope with the plasma membrane that is performed by

the S2 domain of S (Figure 3 A)[54,66]. In the absence of TMPRSS2, S keeps interacting with ACE2, triggering the internalization of the virions by receptor-mediated endocytosis[54,66]. The internalized virus particles are trafficked to the late endosome where they encounter cathepsin B or L (CTSB, CTSL). Upon proteolytic activation of S by these proteases fusion between the viral envelope and the endosomal membrane is induced (Figure 3 B)[54,66,67]. Cathepsins are endolysosomal proteases that require an acidity-catalyzed autoproteolytic activation to be converted to their active form, which accounts for the pH-dependency of the endocytic entry route of SARS-CoV-2[55,68].

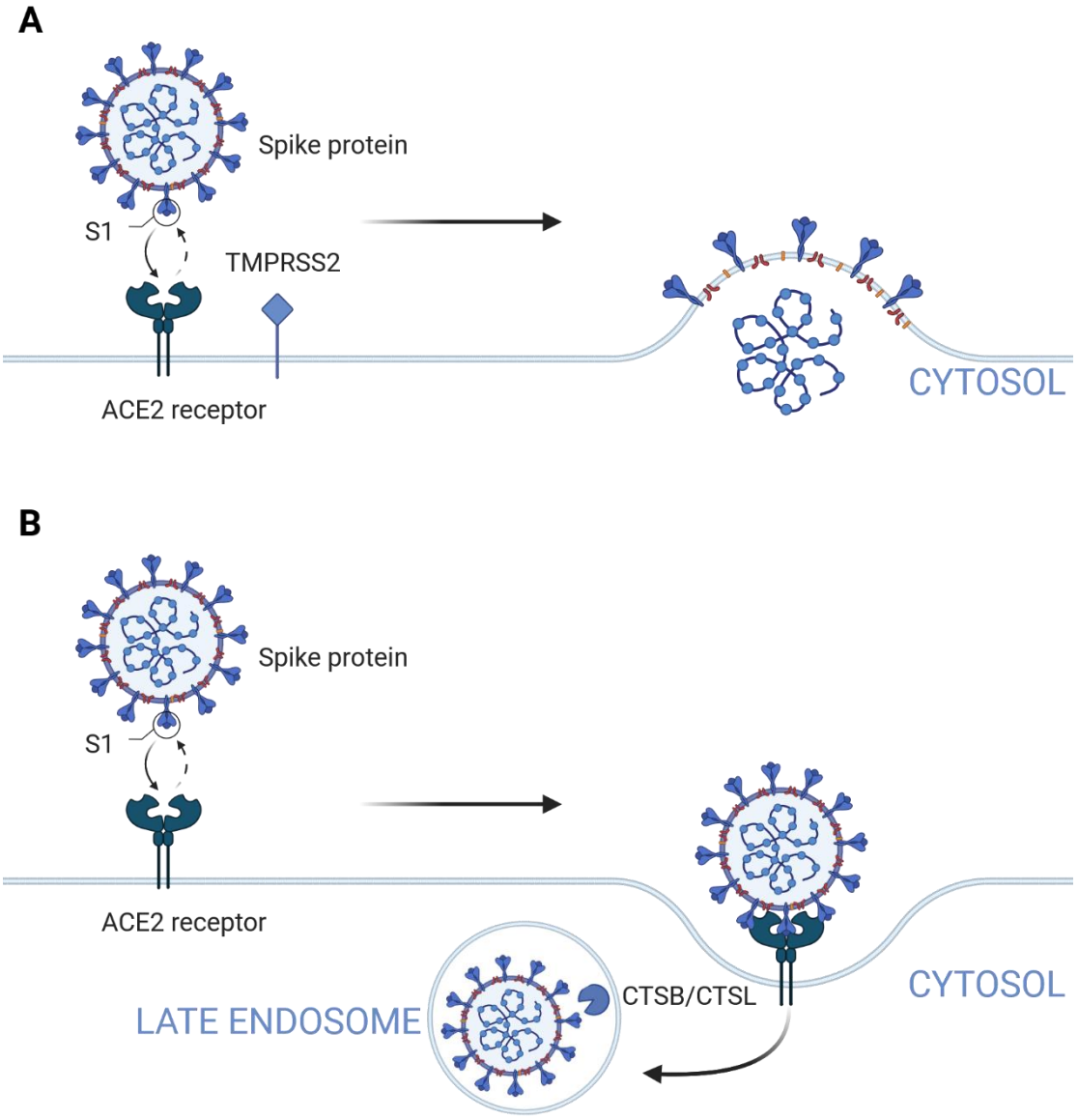

Figure 3: Schematic representation of the two major entry pathways that SARS-CoV-2 can employ to enter cells. A) The preferred entry route is mediated by the proteolytic activation of the SARS-CoV-2 S protein by TMPRSS2 on the plasma membrane. B) In TMPRSS2-deficient cells, SARS-CoV-2 can enter cells through receptor-mediated endocytosis. During this entry pathway the S protein is proteolytically activated by cathepsin proteases in the late endosome. This schematic was created using BioRender.com.

After the viral ribonucleoprotein complex is released into the cytosol, ORF1a and ORF1b of the viral genomic RNA are translated into the replicase polyprotein that is proteolytically cleaved into the distinct NSPs required for replication and transcription[64]. These cleavages are performed by either one of the two viral proteases: the papain-like protease (PL^{pro}; NSP3) or the main protease (M^{pro}; NSP5)[64,69,70]. NSP1 is involved in controlling host protein translation by binding the 40S ribosomal subunit and blocking the mRNA channel[71]. This process is mitigated by the full-length SARS-CoV-2 5' untranslated region, suggesting a selectivity of viral protein synthesis over host cell synthesis in SARS-CoV-2 infected cells[71]. With the emergence of the mature NSPs, the next step in the viral life cycle is the establishment of double membrane vesicles (DMVs) which are the replication organelles of SARS-CoV-2 located in proximity to the endoplasmic reticulum (ER) membrane[72]. The biogenesis of DMVs depends on the presence of two NSPs: NSP3 and NSP4[73]. In addition, NSP3 and NSP4 seem to form pores that span both membranes of the DMVs, likely creating a channel for the release of synthesized genomic and subgenomic RNAs into the cytosol[73,74].

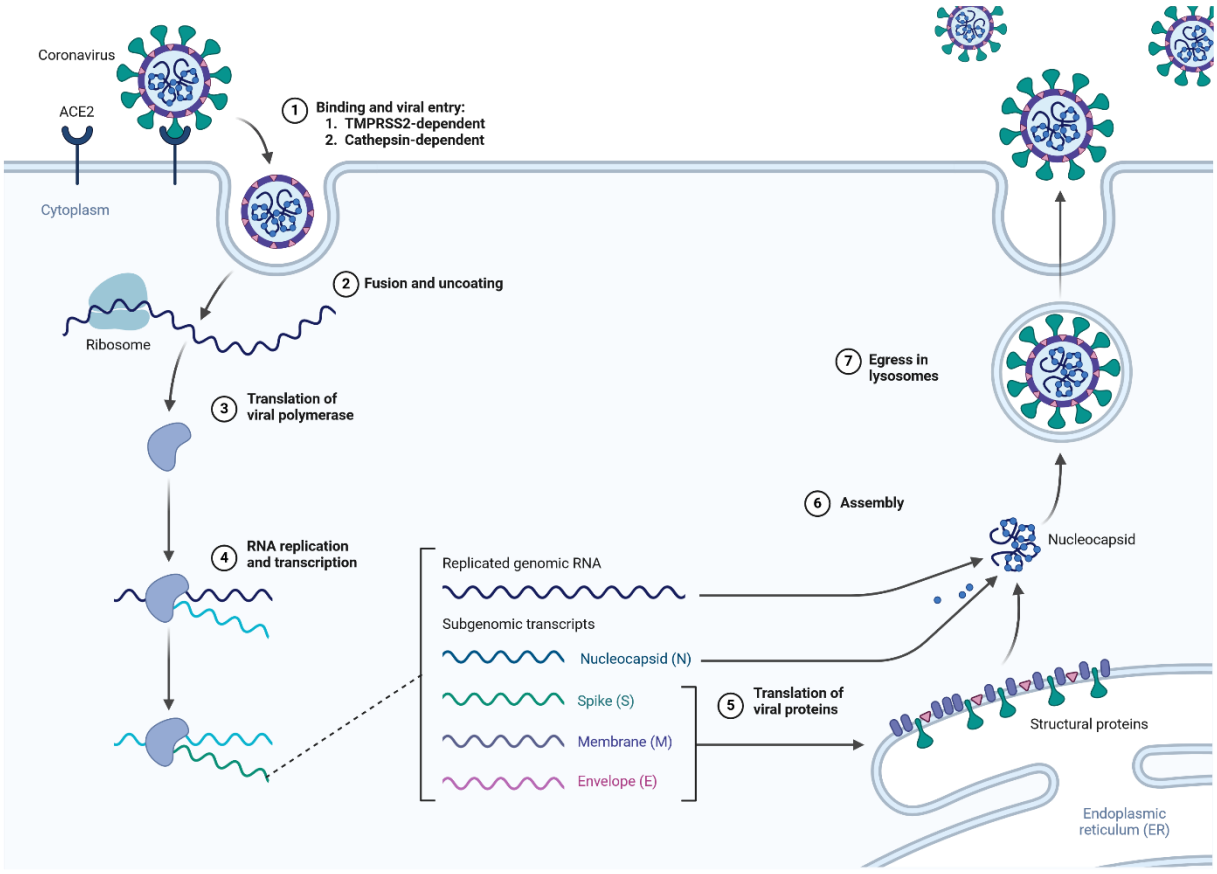

Figure 4: Schematic representation of the SARS-CoV-2 life cycle. The SARS-CoV-2 life cycle is initiated by an interaction of the SARS-CoV-2 S protein with its cellular receptor ACE2[54]. Following receptor binding, S is proteolytically activated by TMPRSS2 or endosomal cathepsins[54,67]. Upon successful entry, the viral RNA is translated, allowing the establishment of DMVs, which are the compartment of viral transcription and replication[73,74]. After replication, novel virions are assembled in

the ER-Golgi-intermediate compartment that can egress the cell in deacidified lysosomes[57,75]. This schematic was generated using BioRender.com.

After genome replication, novel viral genomic RNAs are encapsidated by the N protein, followed by assembly of viral particles at the ER-Golgi-intermediate compartment[57]. This process is mainly controlled by M, which recruits the other structural components of SARS-CoV-2 virions to the assembly sites[57]. During assembly, a conformational switch in M controls the membrane curvature at the assembly sites that is necessary for the formation of novel particles[57]. The newly synthesized virions subsequently egress the cell in deacidified lysosomes[75]. A schematic of the SARS-CoV-2 replication cycle is shown in Figure 4.

I.5 Genome-wide loss-of-function screenings for the identification of viral host factors

Genome-wide loss-of-function screenings for the identification of SARS-CoV-2 host dependency factors have proved to be a useful tool for non-biased screening of dependency factor candidates. These screenings are based on CRISPR/Cas9 genome editing technology that enables the selective inactivation of cellular genes and the subsequent assessment of the necessity of these genes for the replication of viruses[76]. An overview of all CRISPR/Cas9 screenings that were performed in the context of SARS-CoV-2 infection is shown in Table 2.

Table 2: Overview of CRISPR/Cas9 screenings that have been conducted in the context of SARS-CoV-2 infection.

Publication	**Year**	**Description**	**Cell line**
Wei *et al.*[77]	2020	Genome-wide loss-of-function screen	Vero E6
Wang *et al.*[78]	2020	Genome-wide loss-of-function screen	Huh7.5.1-ACE2-TMPRSS2
Daniloski *et al.*[79]	2020	Genome-wide loss-of-function screen	A549-ACE2
Schneider *et al.*[80]	2020	Genome-wide loss-of-function screen	Huh7.5
Hoffmann *et al.*[81]	2020	Interactome-wide loss-of-function screen	Huh7.5
Zhu *et al.*[82]	2021	Genome-wide loss-of-function screen for the identification of factors during endocytic entry	A549-ACE2
Baggen *et al.*[83]	2021	Genome-wide loss-of-function screen	Huh7
Rebendenne *et al.*[84]	2022	Genome-wide bidirectional screen	Vero E6, Calu-3, Caco-2
Grodzki *et al.*[85]	2022	Genome-wide loss-of-function screen	Vero E6, HEK293T-ACE2
Biering *et al.*[86]	2022	Genome-wide bidirectional screen	Calu-3
Israeli *et al.*[87]	2022	Genome-wide loss-of-function screen	Calu-3

Chan *et al.*[88]	2022	Genome-wide loss-of-function screen	Vero E6, Calu-3, Huh7, UM-UC-4, HEK293T-ACE2-TMPRSS2
Danziger *et al.*[89]	2022	Genome-wide activation screen	A549-ACE2
Mac Kain *et al.*[90]	2022	ISG-wide loss-of-function screen	A549-ACE2
Ugalde *et al.*[91]	2022	Genome-wide loss-of-function screen for the identification of factors during entry	Calu-1-ACE2
Feng *et al.*[92]	2023	Genome-wide activation screen	HeLa
Pagis *et al.*[93]	2023	Genome-wide loss-of-function screen	HESC-derived cells
Yousefi *et al.*[94]	2023	Genome-wide loss-of-function screen	IGROV-1
Loo *et al.*[95]	2023	Genome-wide activation screen for the identification of S binders	HEK293T
Bragazzi Cunha *et al.*[96]	2023	Focused loss-of-function screen (833 genes of interest included)	Calu-3
Hossain *et al.*[97]	2023	Genome-wide loss-of-function screen for the identification of factors during entry	HEK293T-ACE2
Sakai *et al.*[98]	2024	Genome-wide loss-of-function screen	A549-ACE2
Yan *et al.*[99]	2024	Genome-wide loss-of-function screen	HEK293T
Frasson *et al.*[100]	2024	Genome-wide loss-of-function screen	Calu-3

Using CRISPR/Cas9 technology multiple host factors involved in various stages of the viral life cycle were identified[101]. During entry, SARS-CoV-2 relies on the presence of the cell surface receptor ACE2[54]. Proteins that regulate intracellular ACE2 trafficking therefore play a critical role as SARS-CoV-2 dependency factors. Multiple factors that regulate ACE2 levels at the plasma membrane have been identified: RAB7A[79], VPS29[82], VPS35[82], COMMD3[82] and NUAK2[102]. Besides ACE2, SARS-CoV-2 can employ a set of auxiliary receptors to enter target cells. For instance, it was shown that the receptor binding domain of S is able to interact with TMEM106B, enabling entry into ACE2-negative cells[83,103]. A similar mode-of-action was established for NRP1, a known binder of substrates cleaved by the host protease furin, such as S[104]. Endocytic entry can also be enabled in cells expressing CD147[105]. In addition, opsonized SARS-CoV-2 particles are able to enter certain immune cells such as monocytes and macrophages through FCγR-dependent internalization[106]. Upon receptor binding S is primed by TMPRSS2 on the cell surface or by cathepsin proteases in the late endosome, allowing S to switch into its fusion conformation[54,67]. During canonical TMPRSS2-dependent entry, the activity of TMPRSS2 is regulated by AP1G1[84,86]. The endocytic entry seems to be supported by a variety of host cell proteins. Niemann-Pick disease, type C1 and C2 (NPC1 and NPC2) are known cholesterol transporters that are involved in the extraction of cholesterol from cellular

endosomes during their maturation[107]. During infection these proteins seem to specifically support the endocytic entry of SARS-CoV-2[78,79,82]. In addition, vacuolar ATPases that contribute to the acidification of the late endosome and therefore enable the proteolytic activation of cathepsin proteases that are required for S priming have been shown to be important host dependency factors during endocytic entry[79]. Due to an involvement of TMEM106B in the acidification of endosomes, it seems plausible that TMEM106B promotes both entry pathways through independent mechanisms[83,108]. Multiple other factors, including proteins of the HOPS complex and mannose-6-phosphate receptors (M6PR), involved in endo-lysosome function were revealed to be dependency factors of SARS-CoV-2 involved in endocytic entry[53].

In addition to these factors involved in SARS-CoV-2 entry, multiple proteins have been shown to support later stages of the viral life cycle. The autophagy related genes VMP1 and TMEM41B have been shown to support the biogenesis of DMVs, the replication organelles of SARS-CoV-2[109]. Other proteins that have been proposed to support SARS-CoV-2 RNA replication are the sterol synthesis regulators SREBP1 and SREBP2[78,80,110,111]. However, the precise mode-of-action by which these factors support SARS-CoV-2 infection remains to be elucidated. Multiple proteomic analyses have furthermore established a link between protein regulators of transcription and mRNA stability and SARS-CoV-2 infection[112–116]. For instance, the stress granule components G3BP1/2 and PABPC1 have been detected in SARS-CoV-2 virion preparations[114]. During SARS-CoV-2 infection, the G3BP proteins seem to support the establishment of virion assembly sites[114].

As expected, given the large number of viral proteins encoded in the SARS-CoV-2 genome, the virus has countless contact sites to cellular proteins that are being hijacked to support various intracellular processes that are required for virus propagation. These proteins can support various stages of the viral life cycle and might even be involved in multiple stages through independent mechanisms, as it seems to be the case for TMEM106B.

I.6 Cellular function of RAB9A

To date, approximately 60 RAB GTPases were identified in mammals that are involved in membrane trafficking processes between various cellular organelles[117]. Amongst these, RAB9A is a small RAB GTPase involved in the retrograde transport of proteins from the late endosome to the trans-Golgi network[118,119]. The protein contains a C-terminal dual cysteine residue that enables prenylation and therefore allows the protein to be anchored into cellular membranes, which is an essential property of all RAB GTPases[120]. RAB9A exists in an active and inactive form, depending on the association with GTP or GDP, respectively[121,122]. The exchange of GDP to GTP on RAB9A, that converts the protein from its inactive GDP-bound state to its active GTP-bound state, is catalyzed by the guanine nucleotide exchange factors (GEF) DENND2A and DENND2D[122]. A schematic overview of the physiological function of RAB9A is shown in Figure 5.

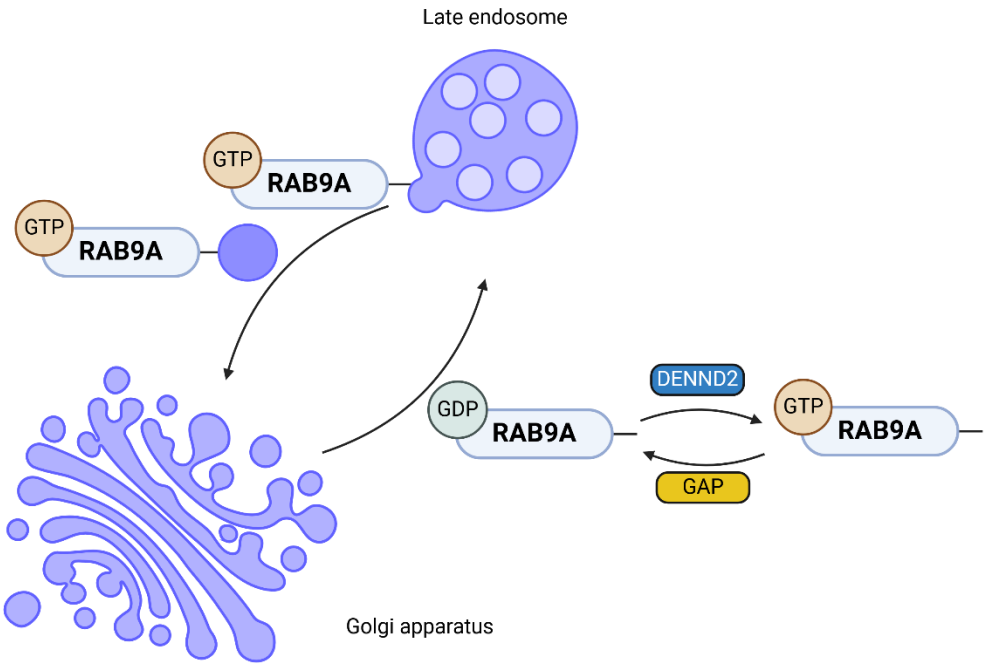

Figure 5: Schematic overview of the cellular function of RAB9A. RAB9A was shown to regulate the retrograde transport of proteins from the late endosome to the trans-Golgi network[118,119]. This process depends on an association of RAB9A with GTP[121,122]. The conversion of RAB9A from its inactive GDP-bound form to its active GTP-bound form is catalyzed by DENND2[122]. This schematic was created using BioRender.com.

Besides its canonical involvement in membrane trafficking, RAB9A is essential for the correct biogenesis of cellular lysosomes and morphological alterations of the endo-lysosomal compartment can be observed in RAB9A-depleted cells[123,124]. In addition, an involvement of

RAB9A in the regulation of the molecular membrane organization of the late endosome seems very likely. RAB9A overexpression was previously shown to be able to compensate deficits in endosomal trafficking of M6PRs in the absence of NPC1, the protein required to extract cholesterol from endosomal membranes during their maturation[125,126]. In addition, it was shown that endosomal cholesterol accumulation sequesters RAB9A, indicating that RAB9A is recruited to endosomes with high cholesterol content[125,126]. Not much research was conducted to understand the possible involvement of RAB9A as a host dependency factor during viral infections. However, a recent study demonstrates that RAB9A supports human papillomavirus (HPV) entry[127], which is further supported by a previous small interfering RNA (siRNA) screening for the identification of HPV entry factors[128]. HPV entry mainly depends on inactive GDP-bound RAB9A[127]. Moreover, RAB9A depletion by siRNA transfection results in reduced vaccinia virus infection[129,130]. It seems unlikely that RAB9A supports HPV and poxvirus infections through the same mode-of-action, as enveloped viruses like poxviruses induce fusion with cellular membranes by mechanisms that differ greatly from the membrane penetration that is performed by non-enveloped viruses like HPV[131]. Nevertheless, these findings indicate that through its convenient localization at the late endosome and its regulation of protein and lipid composition of the endosomal compartment, RAB9A is a host dependency factor exploited by various viral pathogens.

I.7 Cellular function of TIMM17B

Mitochondrial protein import relies on two major protein complexes[132]. The translocase of the outer membrane (TOM) complex located in the outer mitochondrial membrane mediates the import of all proteins with mitochondrial localization[132]. This includes proteins that are integrated into the outer mitochondrial membrane or imported into the intermembrane space but also all proteins that are destined to reach the inner mitochondrial membrane or the mitochondrial matrix[132]. Inner membrane and matrix targeting proteins containing the respective presequence are further transported by the translocase of the inner membrane (TIM) 23 complex is situated in the inner mitochondrial membrane[132]. Upon successful import into the matrix, the presequence of these proteins is cleaved by the mitochondrial processing peptidase[133]. A schematic overview of the mitochondrial protein import process is shown in Figure 6.

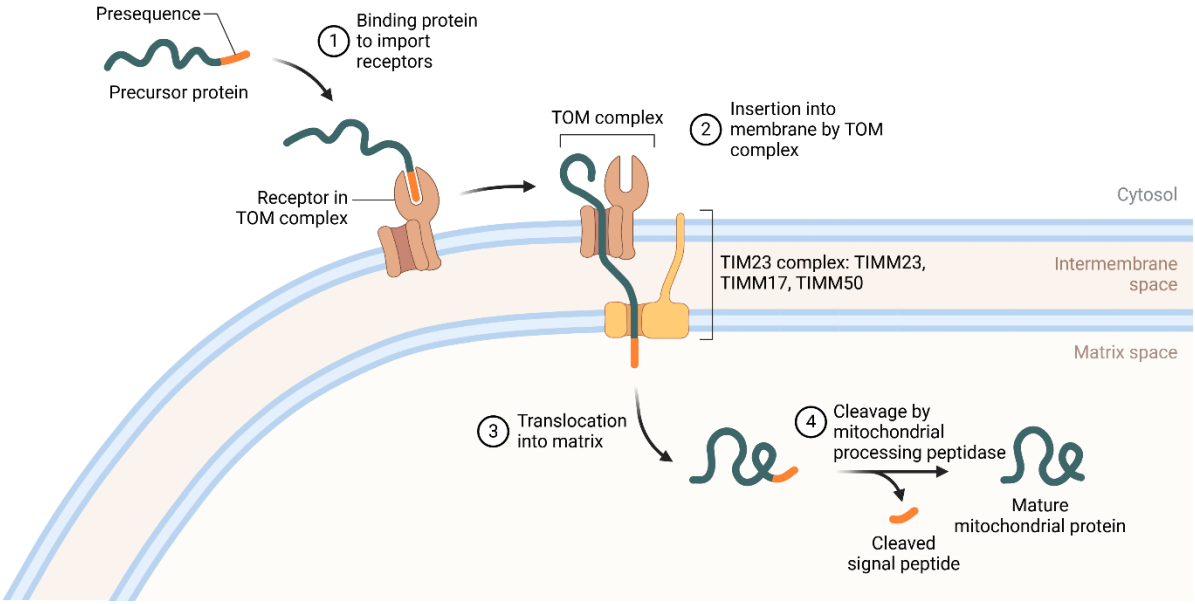

Figure 6: Schematic overview of the involvement of the TOM and TIM23 complexes in the import of presequence containing proteins into the mitochondria. During the first step an interaction (1) between the presequence and the TOM complex is formed allowing the import of the presequence containing protein into the intermembrane space[132] (2). If the imported protein contains a matrix localization sequence it subsequently interacts with the TIM23 complex in the inner mitochondrial membrane and is either inserted into the inner mitochondrial membrane or imported into the mitochondrial matrix[132] (3). Upon successful import a mitochondrial processing peptidase cleaves off the signal peptide, giving rise to the mature matrix proteins[133] (4). This schematic was created using BioRender.com.

The TIM23 complex possesses three core components: TIMM23, TIMM17 and TIMM50[132]. However, multiple other proteins have been shown to be associated with the TIM23 complex and may possess auxiliary function for mitochondrial protein import[132]. While TIMM23 is sufficient to form pores in the inner membrane, these channels are lacking selectivity towards peptides containing presequences[134,135]. Only upon hetero-oligomerization with TIMM17 a twin-pore structure that resembles the physiological TIM23 complex can be observed[134,136]. The C-terminal domain of TIMM17 seems to be critical for correct oligomerization with TIMM23 and hence for the correct formation of the fully selective and functional TIM23 complex[134,136]. The presequences of matrix-targeting proteins contain multiple positive charges that can interact with negative charges in TIMM17[137]. Due to the membrane potential between the intermembrane space and the mitochondrial matrix the TIM23 channel needs to be voltage gated which depends on the N-terminal domain of TIMM17B[134,136]. Conclusively, TIMM17B is the major determinant for the selectivity of mitochondrial protein import into the matrix.

II. Objectives

Prior to the start of this project, two independent genome-wide CRISPR/Cas9 loss-of-function screenings for the identification of SARS-CoV-2 host dependency factors were performed in A549-ACE2 and Calu-3 lung epithelial cells in the laboratory of Dr. Ralf Bartenschlager. The screenings were conducted by Dr. Berati Cerikan in collaboration with Dr. Florian Heigwer and Dr. Luisa Henkel from the laboratory of Dr. Michael Boutros (DKFZ, Germany). For the screening, a self-developed lentiviral sgRNA library was used[138]. Upon transduction with the sgRNA library, the cells were infected with SARS-CoV-2 and incubated until a significant cytopathic effect was evident in the infected culture. Subsequently, genomic DNA was extracted and subjected to Illumina sequencing to identify the barcoded sgRNAs that are enriched when compared to the library control. Observed enrichments in the abundance of specific sgRNAs inversely correlate with the cells' susceptibility to SARS-CoV-2 infection and allow the identification of proviral genes. To identify dependency factors required for SARS-CoV-2 infection of various cell models, I aimed to integrate the data generated by these two loss-of-function screenings with the data of four previously published SARS-CoV-2 CRISPR/Cas9 screenings performed in a variety of cell lines[77–80]. To this end, my objective was to identify factors enriched above certain thresholds in all six screens included in this analysis. To confirm the relevance of potential hits identified by this approach, I set out to perform a detailed validation of the potential dependency factors in a variety of cell lines and using different virus isolates. After confirming the dependency of SARS-CoV-2 on the presence of the identified factors, I planned to elucidate the detailed molecular mechanism by which SARS-CoV-2 infection is supported by this particular host cell factor. This includes the identification of the precise step of the viral life cycle that is supported by the novel dependency factor and the elucidation of molecular determinants of the dependency factor's proviral activity. Furthermore, I aimed to investigate a potential relationship between the identified dependency factors and previously characterized host factors to identify cellular pathways that are central for distinct steps of the SARS-CoV-2 life cycle.

III. Materials

Table 3: Antibodies

Antibody	**Host**	**Manufacturer**	**Article number**
Anti-ACE2	Rabbit	Sino Biological	10108-T24
Anti-Calnexin	Rabbit	Enzo Life Sciences	ADI-SPA-860-F
Anti-CTSB	Rabbit	Cell Signaling Technology	D1C7Y
Anti-CTSL	Goat	R&D Systems	AF952
Anti-goat IgG HRP	Rabbit	Sigma Aldrich	A5420-5X1ML
Anti-LAMP1	Mouse	Invitrogen	14-1079-80
Anti-mouse IgG Alexa Fluor-568	Donkey	Thermo Fisher	A-10037
Anti-Nucleocapsid	Mouse	Sino Biological	40143-MM05
Anti-Nucleocapsid	Rabbit	Rockland	200-401-A50
Anti-RAB7A	Rabbit	Cell Signaling Technology	2094S
Anti-RAB9A	Rabbit	Cell Signaling Technology	D52G8
Anti-rabbit IgG Alexa Fluor-488	Donkey	Thermo Fisher	A-21206
Anti-rabbit IgG AlexaFluor-568	Donkey	Thermo Fisher	A-10042
Anti-rabbit IgG HRP	Goat	Sigma Aldrich	A6154-5X1ML
I1-Hybdridoma supernatant	Mouse	Homemade	-

Table 4: Chemicals, reagents and kits

Reagent or kit	**Manufacturer**	**Article number**
2-Mercaptoethanol	Sigma Aldrich	M6250-250ML
2-propanol	Honeywell	33539
Ammonium chloride	Roth	5470.1
Ammonium peroxidisulfate (APS)	VWR	21300.260
Ampicillin	VWR	0339-EU-25G
Anhydrous acetic acid	Roth	3738.1
Bacto-Trypton	Becton	80965
Bafilomycin A1	Sigma Aldrich	5084090001
Benzonase Nuclease	Merck	70664

Blasticidin	Thermo Fisher	R21001
Bovine serum albumin (BSA)	Merck	A3294-50G
Bromophenol blue	Waldeck	4F-057
Carbenicillin	Roth	6344.3
CellTiter-Glo 2.0	Promega	G9241
Crystal violet	Sigma Aldrich	HT90132-1L
Cycloheximide	Sigma Aldrich	C7698-5G
DMEM	Gibco	41965-039
E-64d	MedChem Express	HY-100229-10mM
Fetal bovine serum (FBS)	Capricorn	FBS-11A
Fluoromount-G	Thermo Fisher	00-4968-02
Formaldehyde solution 37-41%	Thermo Fisher	F/1501/PB15
Gene Blazer *In Vivo* Detection Kit	Thermo Fisher	12578134
GeneRuler 1kb DNA ladder	Thermo Fisher	SM0313
Geneticin (G418) sulfate	Santa Cruz	sc-29065B
Gentamicin	Thermo Fisher	15750037
Glycerol	Honeywell	15523
GoTaq® G2 Hot Start Taq Polymerase	Promega	M7406
HEPES Buffer Solution (1M)	Gibco	15630-056
High Capacity cDNA Reverse Transcription kit	Thermo Fisher	#4374967
Hoechst33342	Sigma Aldrich	B2261-100MG
Hygromycin B	Thermo Fisher	10687010
Immobilon-P 0.45 µM PVDF membranes	Merck	IPVH00010
iTaq universal SYBR Green Supermix	BioRad	1725124
Lenti-X Concentrator	TaKaRa	631231
Lipofectamine 2000	Invitrogen	11668-019
Lipofectamine RNAiMAX	Invitrogen	13778-150
Lysotracker Red DND-99	Thermo Fisher	L7528
MEM non-essential amino acids (NEAA) (100 x)	Gibco	11140050
Methanol	Honeywell	32213
MIDORI Green Advance DNA stain	NIPPON Genetics	MG04
Mifepristone	Sigma Aldrich	M8046-500MG

Milk powder	Roth	T145.2
NucleoBond PC500	Machery-Nagel	740574.50
NucleoSpin Gel and PCR Clean-up	Machery-Nagel	740609.250
NucleoSpin Plasmid	Machery-Nagel	740588.250
NucleoSpin RNA Plus	Machery-Nagel	740984.250
NucleoSpin Tissue Mini kit	Machery-Nagel	740952.50
OptiMEM	Gibco	31985-047
Orange G	Sigma Aldrich	75380
Paraformaldehyde (PFA)	Sigma Aldrich	16005-1KG-R
Phusion Flash High-Fidelity PCR Master Mix	Thermo Fisher	F548S
Polyethylenimine (PEI)	Polysciences	23966-100
Poly-L-lysine solution	Sigma Aldrich	P4832-50mL
Potassium chloride	Sigma Aldrich	31248-1KG
Potassium hydroxide	Labochem	LC-4929.1
Precision Plus Protein Dual Color Standards	Bio-Rad	#1610374
Probenecid	Invitrogen	P36400
Puromycin	Merck	P 883
qScript XLT One-Step RT-qPCR Tough Mix	Quantabio	95132-02K
RiboLock RNase Inhibitor	Thermo Fisher	EO0381
Rotiphorese 40% acrylamide/bisacrylamide mix (29:1)	Roth	A515.1
Sodium chloride	Roth	9265.2
Sodium dodecyl sulfate (SDS)	SERVA	20765.03
TEMED	ITW Reagents	A1148
Tris	Roth	4855.2
Tris-HCl	Roth	9090.2
Triton X-100	Merck	108603
Trypsin/EDTA	Merck	T4174
Tween-20	Roth	9127.1
UltraPure Agarose	Invitrogen	16500500
VELOCITY DNA Polymerase	Bioline	BIO-21098
Versene	Gibco	15040-033
Western Lightning Plus	Perkin Elmer	NEL104001EA

Yeast extract	Roth	89784
Zeocin	Thermo Fisher	R25001

Table 5: Cell lines and bacteria

Cell lines	**Source**	**Identifier/reference**	**Antibiotic**
293T	ATCC	CRL-3216™	-
A549	ATCC	CCL-185™	-
A549-ACE	-	Cortese *et al.,* 2020[72]	500 µg/mL geneticin
A549-ACE2-Cas9	This study	-	500 µg/mL geneticin 5 µg/mL blasticidine
A549-ACE2-TMPRSS2	-	Prasad *et al.,* 2023[102]	500 µg/mL geneticin 10 µg/mL blasticidine
BHK-G43	Gert Zimmer, University Bern	Zettl *et al.,* 2020[139]	500 µg/mL hygromycin B 1 mg/mL zeocin
Calu-3	ATCC	HTB-55™	-
Calu-3-Cas9	This study	-	10 µg/mL blasticidine
E. coli DH5α	Invitrogen	18258-012	-
HeLa	ECACC	93021013	-
HeLa-ACE	This study	-	10 µg/mL blasticidine
Huh7	-	Nakabayashi *et al.,* 1982[140]	-
I1-Hybridoma	ATCC	CRL-2700™	-
Vero E6	ATCC	CRL-1586™	-

Table 6: Viruses

Virus isolate	Source	Identifier/reference
SARS-CoV-2 B.1.1.529	Patient isolate from University Hospital Heidelberg	Benning *et al.*, 2022[141]
SARS-CoV-2 B.1.617.2	Patient isolate from University Hospital Heidelberg	Benning *et al.*, 2022[141]
SARS-CoV-2 BavPat1/2020	Christian Drosten/European Virus Archive	SKU:026V-03883
Vesicular stomatitis virus (VSV) ΔG-S/G	Gert Zimmer, Bern University	Zettl *et al.*, 2020[139]

Table 7: Software

Software	Source	URL
CellProfiler 4.2.1	Broad Institute[142]	https://cellprofiler.org/
CellProfiler Analyst	Broad Institute[143]	https://cellprofileranalyst.org/
ColocJ	Karl Rohr [144]	https://ieeexplore.ieee.org/stamp/stamp.jsp?arnumber=10124215
ColocQuant	Karl Rohr [144]	https://ieeexplore.ieee.org/stamp/stamp.jsp?arnumber=10124215
Flowing Software 2.5.1	Turku Bioscience	https://bioscience.fi/services/cell-imaging/flowing-software/
GelAnalyzer 19.1	Istvan Lazar Jr. and Instvan Lazar Sr.	http://www.gelanalyzer.com/?i=1
GraphPad Prism 8.4	GraphPad Software	https://www.graphpad.com/
GTEx	Broad Institute	https://gtexportal.org/home/
Ilastik 1.3	Anna Kreshuk[145]	https://www.ilastik.org/index.html
ImageJ	NIH	https://imagej.nih.gov/ij/download.html

JACoP	Fabrice P. Cordelières and Susanne Bolte[146]	https://imagej.net/plugins/jacop
Mageck 0.5	Li *et al.*[147]	https://sourceforge.net/projects/mageck/
R 4.3.2	R-Core[148]	https://cran.r-project.org/
R/fgsea	Korotkevich *et al.*[149]	https://www.bioconductor.org/packages/release/bioc/html/fgsea.html
R/tidyverse	Hadley Wickham[150]	https://www.tidyverse.org/
Visual Basic for Applications (VBA)	Microsoft	-
Zen	Zeiss	https://www.zeiss.com/microscopy/en/products/software/zeiss-zen.html

Table 8: Plasmids

Plasmid	**Source**	**Description/reference**
Lenti-Cas9-2A-Blast	Jason Moffat, University of Toronto	Lentiviral construct encoding Cas9[151]
pCMV_Gag-Pol	Didier Trono, EPFL	Lentiviral packaging construct
pCMV3_SARS-CoV-2_Spike_dCTD3	This study	Codon-optimized SARS-CoV-2 S with deleted C-terminal domain 3
pCMV-ΔR8.91	Marco Binder, DKFZ[152]	Encodes HIV gag-pol
pMD2_VSV-G	Didier Trono, EPFL	Lentiviral packaging construct
pMM310	Barbara Müller, University Hospital Heidelberg	Expression construct encoding a Vpr-BLAM fusion protein[153]
pTet-BSD-v2-ACE2	Vibhu Prasad, University Hospital Heidelberg[102]	Lentiviral construct for ACE2 expression

pWPI_PuroR_EF1a_TMPRSS2	This study	Lentiviral construct for TMPRSS2 expression

Table 9: Primers for RT-qPCR. *Primer sequences for the detection of TIMM17B were obtained from the Harvard Primer Bank (Primerbank ID: 269784612c2).

Primer name	**Sequence (5'-3')**
ACE2 For	CAGGAAATGTTCAGAAAGCA
ACE2 Rev	TCTTAGCAGAAAAGGTTGTG
DENND2A For	ATTGGCTGACAAGGTCAAGGT
DENND2A Rev	ACTCTAGCGTGAGGTTGTGG
DENND2D For	CCTGGACTCCCACCTAGAAC
DENND2D Rev	CACTGAGACAAGGTGCTGAGA
HPRT For	CCTGGCGTCGTGATTAGTG
HPRT Rev	ACACCCTTTCCAAATCCTCAG
Leader For	TCCCAGGTAACAAACCAACCAACT
N For	TTACAAACATTGGCCGCAAA
N Probe	FAM-ACAATTTGCCCCCAGCGCTTCAG-BHQ1
N Rev	GCGCGACATTCCGAAGAA
ORF7A Rev	AAATGGTGAATTGCCCTCGT
RAB9A For	GCCGCGAGGGTTCTTGA
RAB9A Rev	TGGAAGAGCTGGGTATCAAACTT
RT For	TCCTGCTCAACTTCCTGTCGAG
RT Rev	CACAGGTCAAACCTCCTAGGAATG
TIMM17B For*	CCCAGATTGGAGGTAGCTTCG
TIMM17B Rev*	TGTGTAGCGAGTGAGGAGGAT

Table 10: Buffers, media and solutions

Buffer/medium/solution	**Composition**
APS solution	10% (w/v) ammonium persulfate in distilled water
DMEM comp.	Dulbecco's Modified Eagle Medium (DMEM) with 10% (v/v) fetal bovine serum (FBS), 100 U/mL penicillin, 100 µg/mL streptomycin, and non-essential amino acids
Laemmli buffer	375 mM Tris-HCl, 50% glycerol, 9% SDS, 9% 2-mercaptoethanol, 0.03% bromophenol blue in distilled water
LB agar	1 L LB medium with 20 g agar, autoclaved
LB medium	1 L distilled water with 10 g Bacto-Trypton, 5 g yeast extract and 2.5 g NaCl, autoclaved
Orange G loading dye	30% glycerol, 69.8% distilled water, 0.2% Orange G
Paraformaldehyde (PFA) solution	4% PFA dissolved in PBS
PBS	140 mM NaCl, 8 mM Na_2HPO_4, 2 mM NaH_2PO_4 in distilled water
PBS-T	PBS, 0.02 % (v/v) Tween-20
Resolving gel buffer (for SDS-PAGE)	1.5 M Tris-HCl (pH 8.8), 0.4% (w/v) SDS in distilled water
Stacking gel buffer (for SDS-PAGE)	1 M Tris-HCl (pH 6.8), 0.8% (w/v) SDS in distilled water
TAE (50x; for agarose gels)	2 M Tris-HCl (pH 8.3), 2 M anhydrous acetic acid, 50 mM EDTA in distilled water
TBS-T	25 mM Tris-HCl, 150 mM NaCl, 2 mM KCl, 0.1% Tween-20 in distilled water, pH 7.4
TGS (for SDS-PAGE)	25 mM Tris, 192 mM glycine, 0.1% SDS in distilled water, pH 8.3
Wet blot transfer buffer	150 mM glycine, 25 mM Tris (pH 8.3), 20% (v/v) methanol in distilled water

Table 11: Devices and machines

Device/machine	**Manufacturer**
BD FACSCelesta Cell Analyzer	BD Biosciences
C1000 Touch light cycler	Bio-Rad
Celldiscoverer7	Zeiss
Centrifuge 5417R	Eppendorf
Centrifuge 5424	Eppendorf
Centrifuge 5424R	Eppendorf
Centrifuge 5427R	Eppendorf
CFX Opus 96 light cycler	Bio-Rad
ChemoCan Imager 3.2	Intas Science Imaging Instruments
FlexCycler2	analytik Jena
HERAsafe HS12 laminar flow hood	Heraeus
Incubation shaker Multitron Pro	INFORS HT
Labotect C200 incubator	Labotect
LSM900 with Airyscan2	Zeiss
Mini-PROTEAN Tetra System	Bio-Rad
Mithras LB 940 plate luminometer	Berthold Technologies
MULTIFUGE 3 S-R	Heraeus
Nanodrop Lite	Thermo Fisher
OmniaTap ultrapure water system	Stakpure GmbH
PowerPac HC power supply	Bio-Rad
Thermomixer comfort	Eppendorf
Thermomixer compact	Eppendorf

Table 12: Plastic material

Material	Manufacturer
10 cm dishes	Corning
15 cm dishes	Falcon
24-well plates	Corning
6-well plates	Corning
96-well plates (white well)	Greiner Bio-One
96-well plates	Corning
96-well plates (glass bottom, black well)	iBL

IV. Methods

IV.1 Re-transformation of *E. coli* and plasmid isolation

For the re-transformation of high copy plasmids in competent *E. coli* DH5α (F– φ80*lac*ZΔM15 Δ(*lac*ZYA-*arg*F)U169 *rec*A1 *end*A1 *hsd*R17(rK–, mK+) *pho*A *sup*E44 λ–*thi*-1 *gyr*A96 *rel*A1), 1 µL of plasmid solution was mixed with 100 µL of competent *E. coli.* The mixture was incubated 20 min on ice and plated out on LB-agar plates with the respective antibiotic for selection. The next day, a 5 mL LB medium culture in a polypropylene tube was inoculated with a colony of the plate and incubated at 37°C overnight to allow bacteria growth. The bacteria were then transferred to Eppendorf tubes, pelleted by centrifugation at 11,000 x g for 30 s and plasmid DNA was isolated using the NucleoSpin Plasmid kit (Macherey-Nagel).

IV.2 Plasmid sequencing

For Sanger-sequencing of inserted regions of plasmids, the SupremeRun service of Eurofins Genomics was employed. The Full Plasmid Sequencing Service of Microsynth was furthermore used to confirm the identity and quality of entire plasmids. For both sequencing services, the samples were prepared according to the manufacturer's instructions.

IV.3 Cell culture

All cells were incubated at 37°C in a humidified environment with 5% CO_2, unless specified otherwise. A549, 293T, Vero E6, and HeLa cells were cultured in Dulbecco's Modified Eagle Medium (DMEM) enriched with 10% (v/v) fetal bovine serum (FBS), 100 U/mL penicillin, 100 µg/mL streptomycin, and non-essential amino acids (NEAA) (referred to as complete DMEM). Calu-3 cells were grown in DMEM supplemented with 20% (v/v) FBS, 100 U/mL penicillin, 100 µg/mL streptomycin, NEAA, and 1 mM sodium pyruvate. Vesicular stomatitis virus (VSV) G-expressing BHK-G43 cells were maintained in Glasgow's Minimum Essential Medium (GMEM) with 10% (v/v) FBS; these cells were treated with 500 µg/mL hygromycin B and 1 mg/mL zeocin every fifth passage. I1-Hybridoma cells for the production of monoclonal antibodies targeting VSV G were cultivated in Minimum Essential Medium (MEM) with Hanks' Balanced Salt Solution and 20% (v/v) FBS in a humidified 100% air atmosphere. The supernatant from I1-Hybridoma cells, containing anti-VSV-G antibody and used for the neutralization of VSV G during pseudovirus production, was centrifuged at 100 x g for 5 minutes, filtered through a 0.45 µm syringe filter, aliquoted, and stored at -20°C. Cell viability was measured in 96-well plates using the CellTiter-Glo 2.0 kit (Promega).

IV.4 Knock-down by siRNA transfection

Knockdown was achieved through reverse transfection using 35 nM ON-TARGETplus siRNA pools (Horizon Discovery), each consisting of 4 siRNAs per gene. Transfection was carried out with Lipofectamine RNAiMAX (Invitrogen) following the manufacturer's protocol. The transfection mixture was prepared in OptiMEM and allowed to incubate for 20 minutes at room temperature. Cells were then added to the transfection mixture and seeded for the experiment. For the characterization of TIMM17B, single siRNAs (Horizon Discovery) were transfected using the protocol described above.

IV.5 Generation of overexpression cell lines by lentiviral transduction

For the generation of lentivirus suspensions encoding a gene of interest, $1.5x10^6$ 293T cells were seeded into 6-well plates and incubated overnight to allow adhesion. On the next day, the cells were transfected with 3 µg pCMV-Gag-Pol, 1.5 µg pMD2-VSV-G and 3 µg of the lentiviral vector of interest using polyethyleneimine (PEI). After 24 h the culture medium was replaced and the lentivirus containing supernatant was harvested on the consecutive day by filtration through a 0.45 µm filter. Lentivirus suspensions were stored in -80°C until the day of transduction.

To generate overexpressing cell lines, $3x10^5$ target cells were seeded into 6-well plates and incubated overnight. On the next day, the culture medium was discarded and 1 mL lentivirus suspension were added onto the cells. The cells were incubated for 24 h before fresh culture medium containing the respective antibiotics for selection of the target cells was added onto the cells. After completed selection, the cells were frozen and stored in liquid nitrogen.

IV.6 Virus isolation, propagation and titration

The SARS-CoV-2 strain BavPat1/2020 (passage 2) was generously provided by Christian Drosten (Charité Berlin, Germany) via the European Virus Archive (Ref-SKU: 026V-03883). The B.1.617.2 ("Delta" variant) and B.1.1.529 ("Omicron" variant) virus strains were isolated and propagated from oropharyngeal swabs of SARS-CoV-2 positive patients at the University Hospital Heidelberg[141]. Both SARS-CoV-2 BavPat/2020 and B.1.617.2 were amplified through passaging in Vero E6 cells, with the virus titers determined by plaque assays in the same cell line. The B.1.1.529 variant was propagated in Calu-3 cells, and its titer was measured using the TCID50 assay in Vero E6 cells.

IV.7 CRISPR loss-of-function screening in Cas9 expressing A549-ACE2 and Calu-3

To establish cells with stable Cas9 expression, A549-ACE2 and Calu-3 cells were transduced with lentiviral particles encoding Cas9, resulting in the A549-ACE2-Cas9 and Calu-3-Cas9 cell pools. A549-ACE2-Cas9 cells were plated in four 15 cm culture dishes and transduced the next day at an multiplicity of infection (MOI) of 0.1 with the lentiviral HD CRISPR sub-library A[154]. After transduction, the cells underwent selection with 2 µg/mL puromycin for 2 days to eliminate non-transduced cells. Following selection, three of the dishes containing library-transduced cells were infected with SARS-CoV-2 BavPat1/2020 at an MOI of 0.5, while one dish was maintained as a non-infected control. Genomic DNA of the cells was extracted using the NucleoSpin Tissue Mini kit (Macherey-Nagel). Samples infected with SARS-CoV-2 were harvested 7 days post-infection.

For the screening with Calu-3-Cas9 cells, four 15 cm culture dishes were seeded with cells, incubated overnight, and transduced with the lentiviral HD CRISPR sub-library A at an MOI of 1. Post-transduction, the cells were selected with 5 µg/mL puromycin for 5 days. Subsequently, three of the dishes were infected with SARS-CoV-2 BavPat1/2020 at an MOI of 0.1, while the non-infected control cells were harvested for genomic DNA extraction. SARS-CoV-2 infected cells were cultured for 14 days to enrich cells resistant to the virus. Genomic DNA was extracted, and the sequencing library was prepared as previously outlined by Henkel and colleagues[154]. Illumina sequencing was carried out at the Deep Sequencing Core Facility of the German Cancer Research Center. Three independent replicates were performed for each cell line.

IV.8 Computational analysis of CRISPR screening sequencing data

Raw sequencing reads were processed into raw counts using the count command from the MAGeCK software package (v 0.5)[147]. The data were then normalized for equal read depth and sgRNA recovery (Figure 7 B). Read counts were divided by the median read count of AAVS1 locus-targeting controls for each sample and multiplied by the median read count of the entire screening. A pseudo count of 1 was added to each read count to prevent zero inflation. To analyze differential mutant abundance, log2-fold changes were calculated for each sample relative to the plasmid control, and statistical significance was determined by comparing the log2-fold change distribution of each gene's sgRNAs to that of the non-targeting (NT) control sgRNAs. The false discovery rate (FDR) was estimated using the Benjamini-Hochberg method

on p-values derived from A549-ACE2 and Calu-3 cells. Screening quality was assessed by correlating normalized log2-fold changes at the gene level between replicates for A549-ACE2 and Calu-3 cells (Figure 7 C, D). Genes with a z-score-scaled log2-fold change greater than 0.2 and an FDR less than 5% were considered hits in the screening.

Given that CRISPR screening hit lists can be influenced by cell type[155], I employed thresholding to select factors that might have moderate effects in individual cell lines but play roles across various cell types and tissues targeted by SARS-CoV-2. To identify similarities between the CRISPR screenings that were performed in the course of this project and four published CRISPR screenings[77–80], I defined hits as factors enriched with a z-score >0.3 or a log2-fold change >0.2 in each screening. The comparative analysis was implemented using Visual Basic for Applications (Microsoft). Tissue-specific gene expression of the 24 identified factors was analyzed using the GTEx platform (Broad Institute).

Raw sequencing data are available via the European Nucleotide Archive study: PRJEB72772. Data and code for reproducing the raw screening data analysis and the comparative analysis of CRISPR screenings can be found at https://github.com/boutroslab/Supp_Stahl_2024.

IV.9 RT-qPCR

To extract total cellular RNA, the NucleoSpin RNA Plus kit (Macherey-Nagel) was utilized, and complementary DNA (cDNA) was synthesized using the High-Capacity cDNA Reverse Transcription Kit (Thermo Fisher), following the manufacturer's instructions. cDNA quantification was performed with the iTaq Universal SYBR Green Master Mix (Bio-Rad). The primers used are listed in Table 9, with HPRT1 serving as a housekeeping gene.

For quantifying SARS-CoV-2 particles bound to or internalized within target cells, RNA was extracted as described above, and viral genomic RNA was measured using the qScript XLT One-Step RT-qPCR Tough Mix (Quanta Biosciences). For normalization, cDNA was synthesized as previously described, and HPRT1 expression was quantified using the iTaq Universal SYBR Green Supermix (Bio-Rad).

IV.10 Immunofluorescence staining of SARS-CoV-2 infected cells

SARS-CoV-2 infected target cells were fixed with PBS-buffered formaldehyde solution (6%), then washed three times with PBS and permeabilized with PBS containing 0.2% Triton-X100 (v/v) for 15 minutes at room temperature. Following permeabilization, the cells were washed once with PBS-T (PBS, 0.02 % (v/v) Tween-20) and incubated for one hour in PBS-T with 2%

milk (w/v). Next, a mouse anti-N antibody (Sino Biological) was added, and the cells were incubated overnight at 4°C. The following day, the cells were washed three times with PBS-T, and a secondary anti-mouse IgG Alexa Fluor-568 (Thermo Fisher) was applied. This was followed by a one-hour incubation at room temperature, after which the cells were washed twice with PBS-T. Nuclear DNA was then stained with Hoechst 33342 (Sigma Aldrich) in PBS for 30 minutes at room temperature. Finally, the cells were washed three times with PBS-T, 100 µL of PBS were added to each well, and the cells were imaged using a Celldiscoverer 7 (Zeiss) with a 20x air objective. The percentage of N-positive cells was determined by thresholding with CellProfiler 4.2.1 (Broad Institute) using the "Identify primary objects" module.

IV.11 Generation of VSVΔG pseudoviruses

The production of VSV pseudotypes (VSVΔG) enveloped with the SARS-CoV-2 S or VSV G protein (VSVΔG-S and VSVΔG-G) was carried out following the protocol described by Zettl *et al.*[139]. Briefly, to create propagation-deficient VSVΔG-G expressing GFP and firefly luciferase, BHK-G43 cells were plated in 10 mL of GMEM with 10% FBS into a 10 cm-diameter dish and allowed to adhere overnight. The following day, the medium was replaced with GMEM containing 5% FBS, and 1 nM mifepristone (Sigma Aldrich) was added. The cells were then incubated for 6 h at 37°C to induce VSV G expression. After induction, the cells were infected with VSVΔG-G and incubated overnight at 37°C to facilitate pseudovirus production. The supernatant was filtered through 0.45 µm syringe filters, centrifuged at 200 x g for 5 minutes, and stored at -80°C.

For generating VSVΔG-S, a 10 cm-diameter dish was coated with poly-L-lysine. 293T cells were seeded in DMEM complete onto the coated dish and incubated overnight for adherence. The following day, the medium was replaced with pre-warmed DMEM complete, and the cells were transfected with a 1:2 ratio of pCMV3_SARS-CoV-2_Spike_dCTD3 and Lipofectamine 2000 (Invitrogen). Transfection was allowed to proceed for 24 hours to ensure adequate expression of the SARS-CoV-2 S protein. Subsequently, the cells were infected with VSVΔG-G for 2 hours at 37°C. After infection, the cells were washed to remove unbound VSVΔG-G, and 7.5 mL of 10% I1-Hybridoma cell supernatant (containing a neutralizing antibody against the VSV G protein) in DMEM complete were added to neutralize any remaining VSV G protein. The cells were incubated with the antibody for 30 minutes at 37°C, then 8 mL of DMEM complete were added, and the cells were incubated overnight at 37°C. The next day, the supernatant was harvested by filtration through a 0.45 µm syringe filter and stored at -80°C.

IV.12 Immunofluorescence staining of bound or internalized SARS-CoV-2

The fixed cells were washed three times with PBS and permeabilized using PBS containing 0.2% Triton-X100 (v/v) for 10 minutes at room temperature. Following permeabilization, the cells were washed again and incubated with PBS containing 1% BSA (w/v) for 1 h. This was followed by an overnight incubation with a 1:2,000 dilution of anti-N antibody (Rockland) in PBS with 1% BSA (w/v) at 4°C. The next day, the cells were washed and stained with a 1:2,500 dilution of anti-rabbit IgG Alexa Fluor-488 conjugated secondary antibody (Thermo Fisher) for 30 minutes at room temperature. After washing the cells three times, nuclear staining was performed using Hoechst 33342 (Sigma Aldrich) for 30 minutes. Finally, the cells were washed again and imaged with a Celldiscoverer 7 (Zeiss).

To quantify viral binding to the cells, the mean intensity of N staining was analyzed using CellProfiler 4.2.1. Background fluorescence, determined from non-infected A549 wild-type cells, was subtracted from each experiment, and any negative intensity values were set to zero. The number of N puncta in the cells was determined by pixel classification in Ilastik 1.3, and segmented N-positive puncta and nuclei were counted using the "IdentifyPrimaryObjects" module in CellProfiler 4.2.1. The number of N-positive puncta per nucleus was calculated. To correct for batch effects between experimental replicates, data were normalized to A549-ACE2 cells transfected with NT siRNA pools and infected with SARS-CoV-2.

For visualizing the co-localization of incoming virus with the lysosomal compartment, siRNA-transfected A549-ACE2 and A549 cells seeded on coverslips were immunostained as described above, with additional co-staining using a 1:100 dilution of mouse anti-LAMP1 antibody (Invitrogen) and a 1:1,000 dilution of anti-rabbit IgG Alexa Fluor-568 conjugated secondary antibody (Thermo Fisher). After staining, the cells were mounted on microscopy slides with Fluoromount-G (Invitrogen). Once mounted, the cells were imaged using super-resolution microscopy with a Zeiss Airyscan 2 LSM900 microscope equipped with a Plan-Apochromat 63x/1.4 Oil DIC objective. Co-localization analysis was performed by computing Mander's coefficients using the ImageJ JACoP plugin[146].

IV.13 Quantification of attached genomic SARS-CoV-2 RNA

To quantify SARS-CoV-2 genomes bound to A549-ACE2 cells transfected with RAB9A-targeting or NT siRNA pools, RT-qPCR-based quantification was performed according to a protocol adapted from Zárate et al.[156]. Briefly, the cells were transfected with siRNAs and then seeded onto 24-well plates. 48 hours post-transfection, the cells were washed twice with pre-warmed DMEM without additives and incubated for 30 minutes in warm DMEM without additives at 37°C. The culture medium was then replaced with PBS containing 1% BSA (w/v), and the plate was incubated for 1 hour at room temperature. Following this, the cells were washed with ice-cold PBS containing 0.5% BSA (w/v), and were inoculated with SARS-CoV-2 in ice-cold PBS with 0.5% BSA (w/v) at various MOIs. The virus was allowed to incubate with the cells for 1 hour at 4°C, after which the cells were washed three times with PBS containing 0.5% BSA (w/v). Finally, the cells were lysed, and RNA was extracted for analysis by RT-qPCR.

IV.14 Staining of cell-surface resident ACE2 for flow cytometry

HeLa-ACE2 cells transfected with siRNA pools targeting RAB9A, ACE2, or NT siRNAs were detached using Versene (Gibco). Following a 5 minute centrifugation at 700 x g at 4°C, the cells were resuspended in PBS containing 2% FBS (v/v) and incubated on ice for 30 minutes. The cells were then centrifuged for 5 minutes at 700 x g at 4°C and incubated with a 1:200 dilution of rabbit anti-ACE2 primary antibody (Sino Biologicals) in PBS with 2% FBS (v/v) on ice for 1 hour. After washing twice, the cells were stained with a 1:500 dilution of anti-rabbit IgG Alexa Fluor-568 antibody (Thermo Fisher) in PBS with 2% FBS (v/v) for 30 minutes on ice. The cells were washed twice again, fixed in 4% PBS-buffered formalin for 10 minutes at room temperature, and then washed twice to remove the fixative. The fixed cells were reconstituted in 200 µL of PBS with 2% FBS (v/v) and analyzed using a BD FACSCelesta Cell Analyzer (BD Biosciences). Data analysis was conducted with Flowing Software 2.5.1 (Turku Bioscience), and the proportion of ACE2-positive cells as well as the mean ACE2 fluorescence intensity of the total cell population were assessed.

IV.15 Western blot

Cells were lysed using a protein electrophoresis buffer composed of 375 mM Tris-HCl, 50% glycerol, 9% sodium dodecyl sulfate (SDS), 9% 2-mercaptoethanol, and 0.03% bromophenol blue. Protein separation was performed by gel electrophoresis using 10% SDS polyacrylamide gels in TGS buffer (25 mM Tris-HCl, 192 mM glycine, 0.1% SDS, pH 8.3) at 90 V. Proteins were then transferred to a methanol-activated polyvinylidene fluoride (PVDF) membrane. After transfer, the membrane was blocked with TBS-T (25 mM Tris-HCl, 150 mM NaCl, 2 mM KCl, 0.1% Tween-20, pH 7.4) containing 5% (w/v) milk for 2 hours at room temperature. The PVDF membrane was then incubated overnight at 4°C with primary antibodies diluted in TBS-T with 5% (w/v) milk: 1:1,000 anti-CTSL (R&D Systems), 1:1,000 anti-CTSB (Cell Signaling Technology), 1:500 anti-RAB9A (Cell Signaling Technology), 1:500 anti-RAB7A (Cell Signaling Technology), or 1:2,000 anti-Calnexin (Enzo Life Sciences). Following incubation, the membrane was washed three times and probed with 1:2,000 anti-rabbit IgG HRP-conjugated secondary antibody (Sigma Aldrich) or 1:5,000 anti-goat IgG HRP-conjugated secondary antibody (Sigma Aldrich) in TBS-T with 5% (w/v) milk for 1 hour at room temperature. After three additional washes, bound antibodies were detected using Western Lightning substrate (Perkin Elmer) and imaged with an INTAS imaging machine. Western blot quantification was conducted using GelAnalyzer 19.1 software. To assess changes in the maturation of CTSB and CTSL, the integrated signal intensities for each lane were summed, and the percentage of each CTSB or CTSL species relative to the total cathepsin in each lane was calculated.

IV.16 Assessment of lysosome morphology

A549-ACE2 cells were transfected with RAB9A-targeting or NT siRNA pools and then seeded onto glass-bottom microchamber slides. The following day, the medium was replaced, and control cells were treated with 10 nM Bafilomycin A1, a lysosomal acidification inhibitor, for 24 hours. The cells were then stained with DMEM complete containing 50 nM Lysotracker Red DND-99 and 1:5,000 Hoechst 33342 for 20 minutes at 37°C. After staining, the cells were washed three times with PBS and maintained in DMEM without phenol red for imaging. Z-stacks of the cells were acquired using an LSM980 microscope with Airyscan 2 in confocal mode, and maximum projections of these z-stacks were generated. Image quantification was performed using the detection mode in ColocQuant and ColocJ[144].

IV.17 Fusion assay employing lentiviral pseudotypes

To evaluate SARS-CoV-2 fusion with the endosomal membrane, lentiviruses carrying active β-lactamase were utilized. For lentivirus production, 293T cells were seeded in 10 cm-diameter dishes and allowed to adhere overnight. The next day, the cells were co-transfected with 5 µg of pWPI_PuroR_empty, pCMV-ΔR8.91, pMM310, and 5 µg of either pMD2_VSV-G or pCMV3_SARS-CoV-2_Spike_dCTD3 using the PEI transfection reagent (Polysciences). Control lentiviruses lacking viral glycoproteins were also produced. Six hours post-transfection, the culture medium was replaced with DMEM complete containing 1:100 HEPES (1 M). After 48 hours, the cell supernatant was filtered through a 0.45 µm membrane filter, and the lentivirus suspension was concentrated 100-fold using the Lenti-X Concentrator (Takara Bio) according to the manufacturer's instructions. The concentrated lentivirus preparation was aliquoted and stored at -80°C. Titration of the lentivirus was carried out using a one-step SYBR-based Product Enhanced Reverse Transcriptase (SG-PERT) assay[157,158].

To assess SARS-CoV-2 fusion, HeLa-ACE2 cells were transfected with RAB9A-targeting or NT siRNA pools and seeded into poly-L-lysine coated 24-well plates. HeLa wild-type cells lacking ACE2 served as controls. 24 h post-transfection, the medium was replaced with fresh DMEM complete. 46 h post-transfection, the control cells were treated with 10 µM E-64d for 2 hours to inhibit cathepsin activity and prevent proteolytic activation of the SARS-CoV-2 S protein. All cells were then infected with $2x10^5$ pico units reverse transcriptase (pURT)/cell for lentiviruses with SARS-CoV-2 S protein or without glycoprotein, or $2x10^3$ pURT/cell for lentiviruses with VSV G protein by spinfection at 16°C at 1,500 x g for 30 minutes. Following this, the cells were incubated for 2 h at 37°C to allow lentiviral particle internalization and fusion with cellular membranes. The cells were washed once with PBS, and 200 µL of fresh DMEM complete was added. The cells were then loaded with CCF2-AM using the GeneBlazer In Vivo Detection Kit using the enhanced loading protocol, including treatment with probenecid. The plate was sealed with adhesive film and incubated at 11°C for 16 h to halt further fusion and allow β-lactamase-mediated conversion of CCF2-AM. After incubation, the cells were washed with PBS, trypsinized, and fixed with 4% formaldehyde for 10 minutes at room temperature. Post-fixation, the cells were washed, resuspended in 200 µL PBS, and analyzed by flow cytometry using a BD FACSCelesta Cell Analyzer (BD Biosciences). Data analysis was performed using Flowing Software 2.5.1 (Turku Bioscience). To improve reproducibility, the median fluorescence intensity at 450 nm (indicative of CCF2-AM converted by β-lactamase) was normalized to the fluorescence at 510 nm (indicative of non-metabolized

CCF2-AM). As the effect of RAB9A on VSV entry was previously ruled out, VSV G-pseudotyped virus fusion rates were used to correct for non-specific effects unrelated to SARS-CoV-2 fusion.

IV.18 Statistical analysis

Statistical analysis of data was performed with the GraphPad Prism software package (version 8.4).

V. Results

In order to identify novel SARS-CoV-2 host dependency factors, two genome-wide CRISPR/Cas9 loss-of-function screenings were conducted in Cas9 expressing A549-ACE2 and Calu-3 cells, respectively. These screenings were provided at the start of this project and then used for a computational integration with the data of four published CRISPR screenings[77–80]. In the following chapter, the results of the CRISPR/Cas9 screenings will be briefly discussed.

V.1 CRISPR/Cas9 screenings in Cas9 expressing A549-ACE2 and Calu-3 cells identify novel SARS-CoV-2 dependency factor candidates

The results of the following chapter were not generated during the course of this dissertation and were provided to me prior to the start of this project. The CRISPR/Cas9 loss-of-function screenings discussed in this chapter were conducted by Dr. Berati Cerikan in the laboratory of Dr. Ralf Bartenschlager in collaboration with Dr. Florian Heigwer and Dr. Luisa Henkel from the laboratory of Dr. Michael Boutros.

In order to identify novel SARS-CoV-2 dependency factor candidates, two independent genome-wide CRISPR/Cas9 loss-of-function screenings were conducted in Cas9-expressing A549-ACE2 and Calu-3 lung epithelial cells (Figure 7 A). For each of the three independent replicates of the two screenings, a new cell population was transduced with the lentiviral HD CRISPR sub-library A, followed by the assessment of the library coverage by relative quantification of the recovered sgRNAs compared to the sgRNA abundance in the library. A good representation of the sgRNA library and a comparable read-depth was observed in both cell lines. However, a lower efficiency of transduction became evident in the screening performed in Calu-3-Cas9 cells by lower library coverage in some samples (Figure 7 B). In addition, a good correlation between the three independent experimental replicates was observed in A549-ACE2-Cas9 cells (Figure 7 C) while the correlation between replicates was lower but still considerable in Calu-3-Cas9 cells (Figure 7 D).

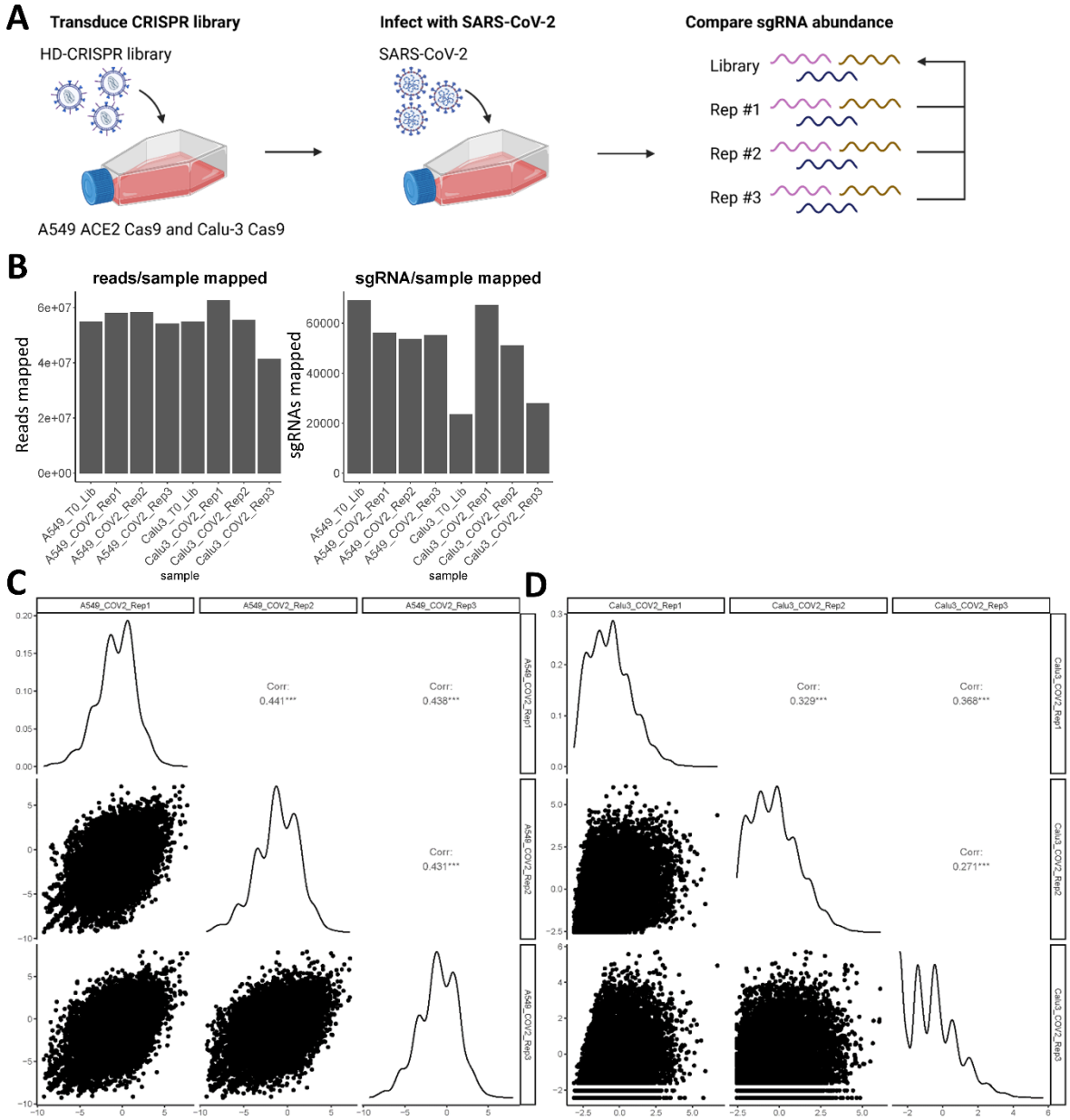

Figure 7: Two whole-genome loss-of-function CRISPR/Cas9 screenings were conducted in Cas9-expressing A549-ACE2 and Calu-3 cells to identify novel SARS-CoV-2 host dependency factor candidates. A) Schematic representation of the two screenings that were conducted. The schematic was created using BioRender.com. B) A549-ACE2-Cas9 and Calu-3-Cas9 cells were transduced with the lentiviral HD CRISPR sub-library A[154] (A549-ACE2-Cas9: MOI 0.1; Calu-3-Cas9: MOI 1). The cells were selected with puromycin and infected with SARS-CoV-2 (A549-ACE2-Cas9: MOI 0.5; Calu-3-Cas9: MOI 0.1). Seven days (A549-ACE2-Cas9) or 14 days (Calu-3-Cas9) after infection, the genomic DNA of infected cells was extracted and barcode sequences were amplified by PCR followed by next-generation sequencing. The sgRNA barcode abundance was compared to the library to quantify the enrichment or depletion of certain barcodes upon SARS-CoV-2 infection. The read-depth was used as a surrogate to quantify the library coverage. C, D) The reproducibility of the CRISPR/Cas9 screening was assessed in A549-ACE2-Cas9 (C) and Calu-3-Cas9 (D) cells by estimation of the Pearson coefficients of gene-level log2-fold changes between replicate samples.

Both screenings revealed previously characterized entry factors of SARS-CoV-2 such as ACE2[159], CTSL[159], ATP6V1A[79] and RAB7A[79] (Figure 8 A, B). The most enriched sgRNAs in

SARS-CoV-2-infected A549-ACE2-Cas9 cells furthermore target TRAT1, FMO1, USP38, POMGNT2, GCM2, HAND2 and SLC25A13 (Figure 8 A; Github folder: "results/A549_results_crispr.txt"). In infected Calu-3-Cas9 cells, the most enriched sgRNAs target KLF8, MMP20, ZNRF3, RNF38, RXFP1 and PREX2 (Figure 8 B; Github folder: "results/Calu3_results_crispr.txt"). Interestingly, an enrichment of sgRNA sequences targeting many members of the v-type ATPase family including ATP6VA1, ATP6AP1, ATP6V1H, ATP6V0B, ATP6V1B2, ATP6V0D1, ATP6V1E1, ATP6V0C, ATP6V1D, ATP6V1F and ATP6V1G1 was observed in A549-ACE2-Cas9 cells (Figure 8 A; Github folder: "results/A549_results_crispr.txt"). These genes are involved in the regulation of endosome acidification that is required for the activation of cathepsin proteases during the endocytic entry of SARS-CoV-2 into A549 cells[160,161]. Surprisingly, a few sgRNAs targeting members of this family, such as ATP6V0D1 and ATP6AP1, were also enriched in SARS-CoV-2-infected Calu-3-Cas9 cells in which a TMPRSS2-dependent entry route that does not require the acidification of endosomes may be utilized by SARS-CoV-2[66], possibly indicating an involvement of v-type ATPases in other stages of the viral life cycle (Figure 8 B; Github folder: "results/Calu3_results_crispr.txt").

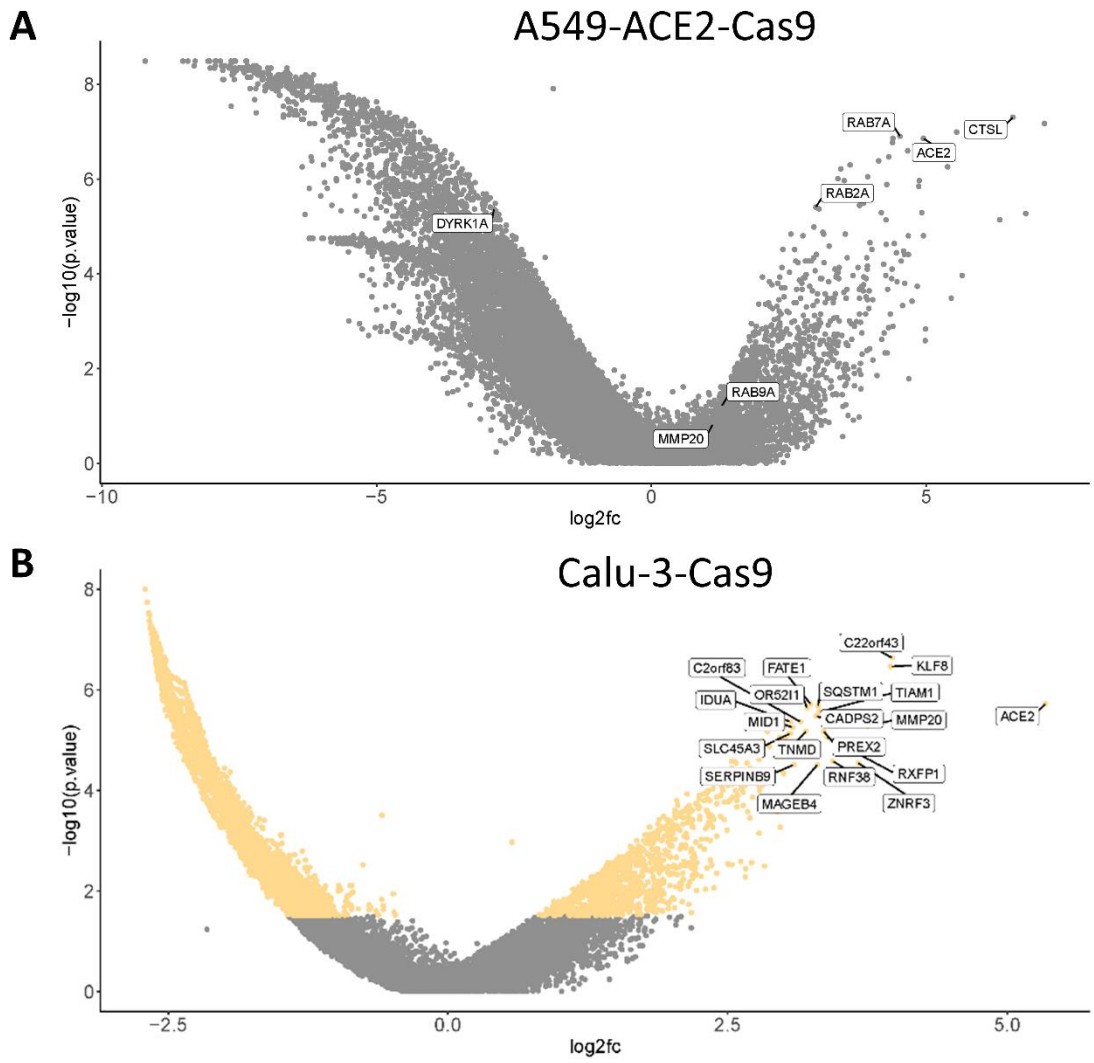

Figure 8: Genome-wide CRISPR/Cas9 loss-of-function screenings in A549-ACE2-Cas9 and Calu-3-Cas9 lung epithelial cells reveal novel SARS-CoV-2 dependency factor candidates. A) A549-ACE2-Cas9 cells were transduced with the lentiviral HD CRISPR sub-library A[154] at a MOI of 0.1. The cells were subsequently selected with puromycin for 2 days to enrich transduced cells and then infected with SARS-CoV-2 (strain BavPat1/2020; MOI: 0.5) for seven days. Genomic DNA of the cells was extracted, barcode sequences amplified by PCR and next-generation sequencing was performed to analyze barcode abundance. The sgRNA barcode abundance was compared to the library control to quantify the enrichment or depletion of certain barcodes upon SARS-CoV-2 challenge. Differential barcode abundance was measured as log2-fold change (log2fc) of SARS-CoV-2 infected cells over plasmid control (T0) and tested for statistically significant differences (p-value) by Wilcoxon rank sum test of each gene's sgRNA counts against the control sgRNAs. A volcano plot displaying the result of the three independent CRISPR/Cas9 screenings conducted in A549-ACE2-Cas9 cells is shown. B) Calu-3-Cas9 cells were transduced with the lentiviral HD CRISPR sub-library A[154] (MOI: 1), selected with puromycin for 5 days and subsequently infected with SARS-CoV-2 (strain BavPat1/2020; MOI: 0.1) for 14 days. Thereafter, genomic DNA was extracted, barcode sequences were amplified by PCR and differential barcode abundance assessed by next-generation sequencing. Differential barcode abundance over the plasmid control (T0) was quantified as log2fc. Statistical significance was assessed by Wilcoxon rank sum test as described above. A volcano plot showing the results of the three independent CRISPR/Cas9 screenings in Calu-3-Cas9 cells is shown.

V.2 Meta-analysis of genome-wide CRISPR/Cas9 loss-of-function screenings reveals RAB9A as a potential SARS-CoV-2 dependency factor

Given the results of the CRISPR/Cas9 screenings generated in the course of this investigation and the data of four published CRISPR/Cas9 screenings in various cell types[77–80], I aimed to identify factors enriched in all of the included CRISPR/Cas9 screenings, arguing that covering a broader range of cell types and screenings will increase the physiological relevance of the identified factors. To this end, I integrated the results of our screenings with the results of four published CRISPR/Cas9 screenings[77–80]. In the computational analysis I used promiscuous thresholding (z-score cut-off: 0.3; log2fc cut-off: 0.2) to identify the factors that are moderately enriched in each of the individual screenings (Figure 9 A). Only factors that are enriched above the threshold values in each of the screens were considered hits (Figure 9 A). I was able to identify 24 potential SARS-CoV-2 host cell dependency factors of which ACE2, the receptor of SARS-CoV-2[159], had the highest average enrichment (Figure 9 B, C). The remaining 23 genes have not yet been described in the context of SARS-CoV-2 infection. Because of the importance of RAB GTPases for the appropriate trafficking of cellular membranes[162] and previous reports demonstrating the importance of other endosomal RAB GTPases for SARS-CoV-2 infection[79], I selected RAB9A, a small RAS-related GTPase involved in the retrograde trafficking of proteins from the late endosome to the trans-Golgi network, for detailed characterization and mechanistic investigation.

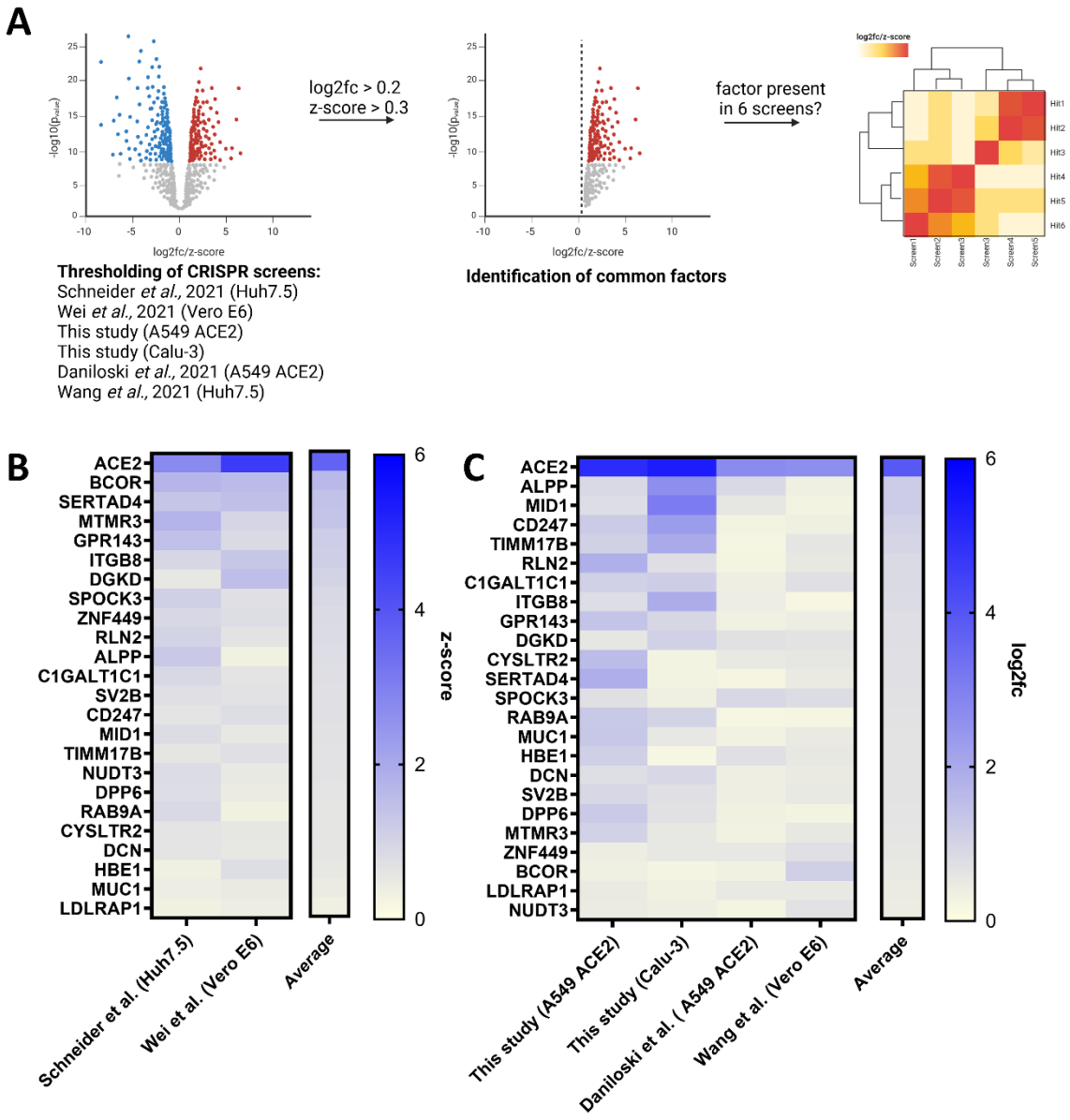

Figure 9: A meta-analysis of genome-wide CRISPR/Cas9 loss-of-function screenings identifies RAB9A as a potential SARS-CoV-2 dependency factor. A) Schematic representation of the computational comparison of CRISPR/Cas9 screenings using different cell lines. The two CRISPR/Cas9 screenings (performed in A549-ACE2-Cas9 and Calu-3-Cas9) conducted during the course of this project were compared to four CRISPR/Cas9 screenings that have been published previously[77–80]. The schematic was created using BioRender.com. Two of these screenings reported z-scores as a measure of sgRNA enrichment, while four of the included screenings used log2fc as a measure of sgRNA enrichment. Only factors enriched with a log2fc>0.2 or z-score>0.3 in each of the respective screenings were considered as hits. B) Heat map showing the z-score of each individual hit in the CRISPR/Cas9 screenings reporting z-scores as a measure of enrichment and the average z-score for each of the hits. The analysis was implemented utilizing the data of Schneider and colleagues generated at 37°C and the average z-scores reported by Wei and colleagues[77,80]. C) Heat map showing the log2fc of each individual hit in the CRISPR/Cas9 screenings reporting log2fc as a measure of enrichment and the average log2fc among the four screenings.

To confirm the expression of RAB9A in tissues that are relevant targets of SARS-CoV-2, I performed a tissue expression analysis of the 24 hits of the meta-analysis. I was able to confirm

a broad expression of RAB9A in all examined tissues, including primary target tissues of SARS-CoV-2 infection *in vivo*, such as the lung[163], heart[49] and gut[36] (Figure 10), further increasing the potential physiological relevance of RAB9A during SARS-CoV-2 infection.

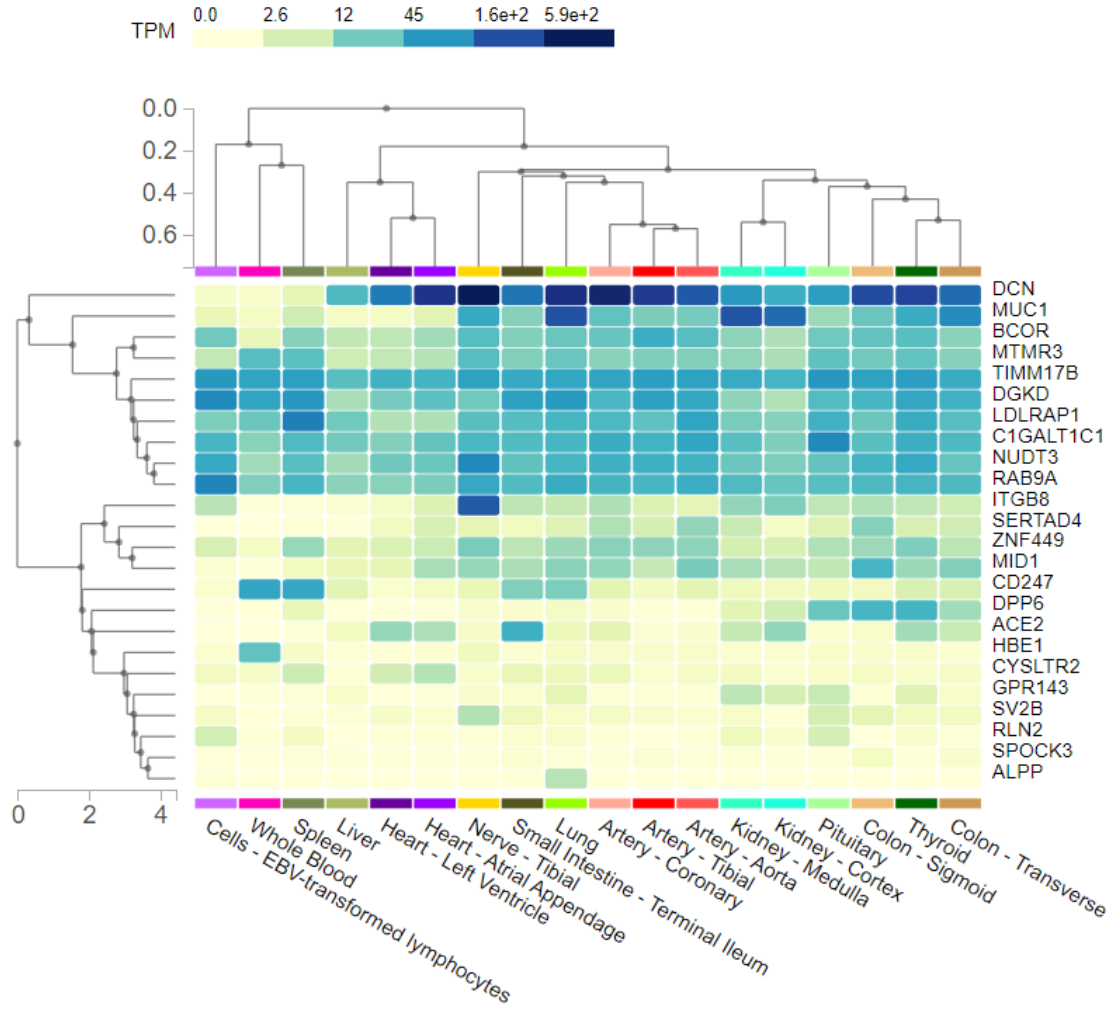

Figure 10: RAB9A is abundantly expressed in most tissues. A tissue expression analysis of the 24 hits identified by the meta-analysis of SARS-CoV-2 CRISPR/Cas9 loss-of-function screenings was performed using the GTEx platform (analysis performed on April 9th, 2024). A broad expression of RAB9A in all included tissues was observed. TPM, transcripts per million.

V.3 RAB9A is a SARS-CoV-2 dependency factor promoting the endocytic entry of SARS-CoV-2

In order to confirm the relevance of RAB9A for the infection of different cell lines with SARS-CoV-2, I transfected HeLa-ACE2 and naïve Huh7 cells with RAB9A-targeting or NT siRNA pools. Efficient knock-down was confirmed in both cell lines using RT-qPCR (Figure 11 A). Potential cytotoxic effects of RAB9A depletion on the two cell lines were excluded by quantification of the number of nuclei in the different conditions (Figure 11 B). 48 h after siRNA transfection, the cells were infected with SARS-CoV-2. Interestingly, I observed a

significant reduction of SARS-CoV-2-infected HeLa-ACE2 and Huh7 cells upon RAB9A depletion (Figure 11 C, D), indicating that RAB9A supports SARS-CoV-2 infection in these two cell lines. To test if RAB9A supports the infection of cells with other SARS-CoV-2 isolates, I infected RAB9A-depleted HeLa-ACE2 cells with SARS-CoV-2 B.1.617.2 (a Delta isolate) and SARS-CoV-2 B.1.1.529 (an Omicron isolate). 24 h.p.i. the cells were fixed and stained for the SARS-CoV-2 N protein to determine the percentage of SARS-CoV-2-infected cells. RAB9A promoted the infection of HeLa-ACE2 cells with both virus isolates, confirming the relevance of RAB9A for the infection of cells with newer SARS-CoV-2 VOCs (Figure 11 E, F).

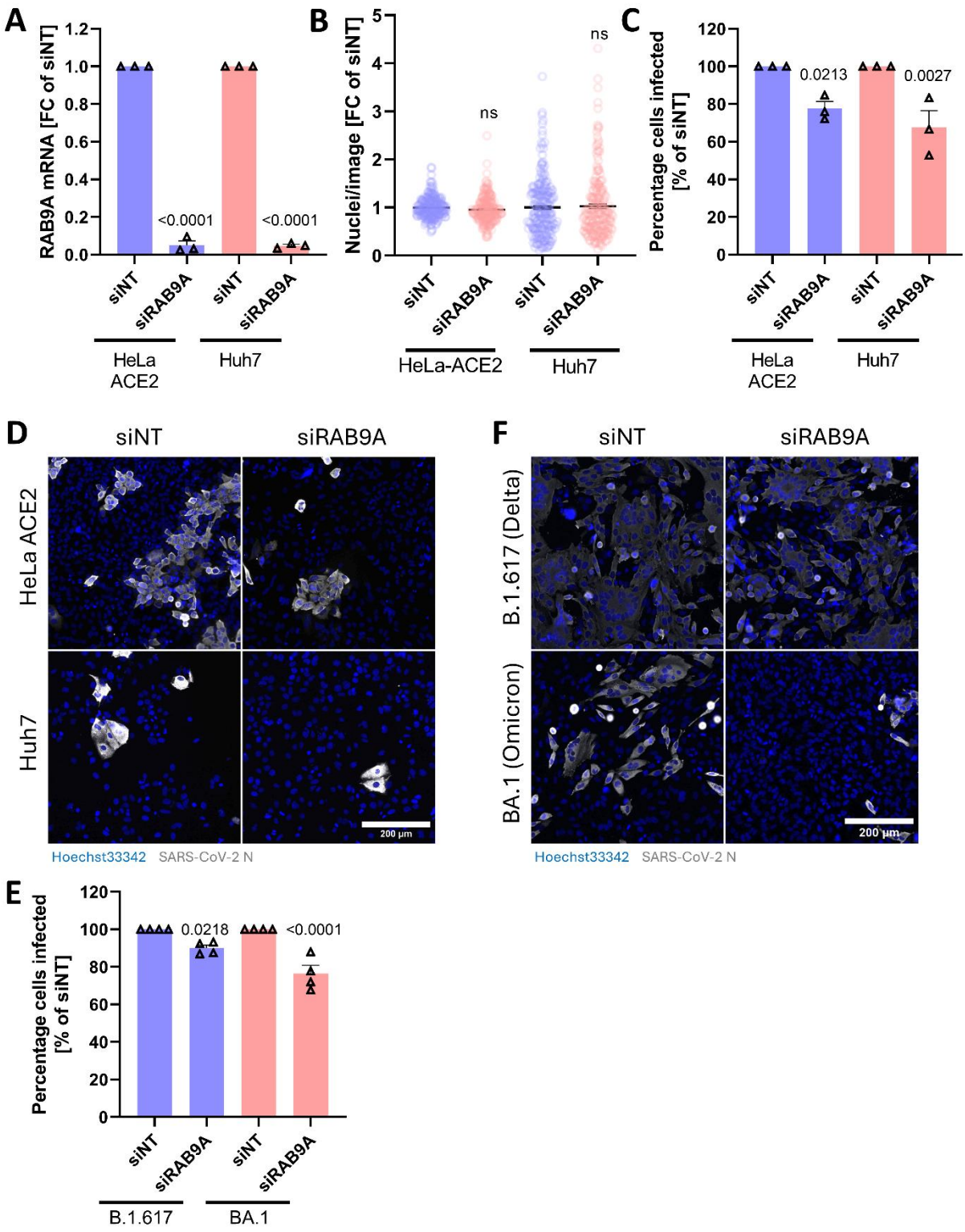

Figure 11: RAB9A supports SARS-CoV-2 infection in different cell types. A) To confirm the relevance of RAB9A in different cell types, HeLa-ACE2 and naïve Huh7 cells were transfected with RAB9A-targeting (siRAB9A) or NT siRNA pools. The efficiency of RAB9A depletion was determined by RT-qPCR. B) 48 h post siRNA-transfection, the cells were infected with SARS-CoV-2 (strain: BavPat1/2020; HeLa-ACE2 MOI 1; Huh7 MOI 5). 24 h.p.i. the cells were fixed, the nuclei were stained with Hoechst 33342. After image acquisition by fluorescence microscopy using a Zeiss Celldiscoverer7 microscope, the nuclei were segmented and quantified using the "IdentifyPrimaryObjects" module of CellProfiler 4.2.1 (Broad Institute) as a surrogate for cell viability. Each point represents one analyzed

image. N=3 independent experiments were performed. C) The percentage of SARS-CoV-2-infected cells was determined by anti-N immunostaining and subsequent fluorescence microscopy using a Zeiss Celldiscoverer7 microscope. The acquired images were analyzed using CellProfiler 4.2.1 (Broad Institute) by thresholding of the N signal as described above. D) Representative micrographs of SARS-CoV-2 infected HeLa-ACE2 and Huh7 cells that were depleted of RAB9A or not. E) To determine the relevance of RAB9A for the infection of cells with other SARS-CoV-2 isolates, HeLa-ACE2 cells were transfected with RAB9A-targeting (siRAB9A) or NT siRNA pools and subsequently infected with SARS-CoV-2 B.1.617.2 (MOI 1) and SARS-CoV-2 B.1.1.529 (MOI 5). 24 h.p.i. the cells were fixed and stained for the SARS-CoV-2 N protein. Micrographs were acquired using a Zeiss Celldiscoverer7 microscope and the percentage of SARS-CoV-2 infected cells was determined as described in C. F) Representative micrographs of SARS-CoV-2 B.1.617.2 and SARS-CoV-2 B.1.1.529 infected HeLa-ACE2 cells that were depleted of RAB9A or not. In A, C and E, each data point represents the results of one independent experimental replicate. Error bars indicate the SEM. Statistical significance was determined by ordinary one-way ANOVA with Šidák test. FC, fold change.

To understand whether RAB9A supports early or late events of the viral life cycle, I infected A549-ACE2 cells that were depleted of RAB9A or transfected with NT siRNA pools with SARS-CoV-2. The infection was terminated by fixation after 8 h to exclude the possibility of viral spread in the cell culture. The viral N protein was visualized by immunostaining and the percentage of infected cells determined by thresholding of the N signal. A significant reduction of SARS-CoV-2 infected cells was evident already at this early stage, indicating an involvement of RAB9A in early stages of the life cycle, such as entry or replication (Figure 12 A, B). SARS-CoV-2 can employ two distinct entry pathways to enter cells[66]. In the presence of the host protease TMPRSS2, the viral S protein can be proteolytically activated directly on the cell surface, leading to fusion of the viral envelope and the plasma membrane[66]. In the case that TMPRSS2 is absent on the cell surface, SARS-CoV-2 will bind its cellular receptor ACE2, followed by the endocytic uptake of the virions that are then transported to the late endosome[54,66]. In the endosomal compartment S can be proteolytically activated by either CTSB or CTSL, inducing the fusion of the viral envelope and the endosomal membrane[54,66,67]. To test the importance of these two distinct pathways for the phenotype observed upon RAB9A depletion, A549-ACE2 cells (in which entry is mediated by the endocytic uptake of SARS-CoV-2) and A549-ACE2-TMPRSS2 cells (in which fusion of SARS-CoV-2 with the plasma membrane is enabled through expression of TMPRSS2) were transfected with RAB9A-targeting or NT siRNA pools and the efficiency of the knock-down was confirmed (Figure 12 C). A marginal but significant cytotoxic effect of RAB9A depletion was observed in A549-ACE2 cells but not in A549-ACE2-TMPRSS2 cells (Figure 12 D). To test the relevance of these two entry pathways, the siRNA-treated cells were subsequently infected with propagation-deficient VSV encoding GFP that was pseudotyped either with SARS-CoV-2 S or VSV G as a control[164]. Interestingly, RAB9A supported the endocytic entry of VSVΔG-S into A549-ACE2 cells but had no impact on VSVΔG-S entry into A549-ACE2-TMPRSS2 cells, indicating a

predominant involvement of RAB9A in the endocytic entry pathway (Figure 12 E). In contrast, no impact of RAB9A depletion on the infection of the cells with VSVΔG-G was observed (Figure 12 E). To further solidify this, the results were confirmed using authentic SARS-CoV-2 which fully reflected the observations made using pseudovirus (Figure 12 F).

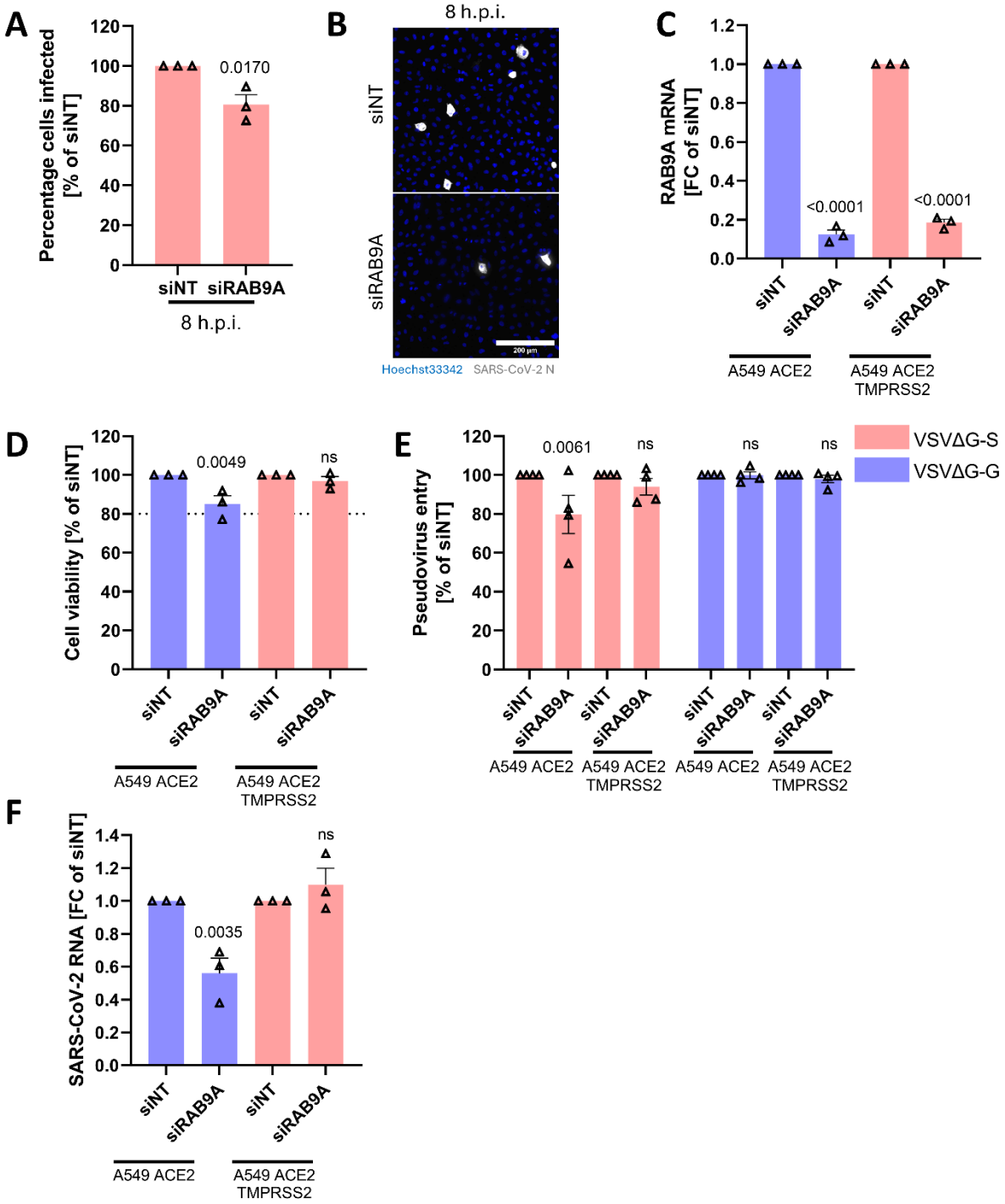

Figure 12: RAB9A supports the endocytic entry of SARS-CoV-2. A) To understand if RAB9A supports early or late events in the viral life cycle, A549-ACE2 cells were transfected with RAB9A-targeting (siRAB9A) or non-targeting (siNT) siRNA pools. 48 h.p.t. the cells were infected with SARS-CoV-2 (strain BavPat1/2020; MOI 5). 8 h.p.i. the cells were fixed to exclude the possibility of viral spread and immunostained against the viral N protein. Fluorescence micrographs were acquired using a Zeiss

Celldiscoverer7 microscope, followed by segmentation of the N signal by thresholding using CellProfiler 4.2.1 (Broad Institute). The percentage of infected cells was calculated. B) Representative micrographs of RAB9A-depleted or NT siRNA transfected A549-ACE2 cells that were infected with SARS-CoV-2 for 8 h. C) To determine if RAB9A supports SARS-CoV-2 entry, A549-ACE2 and A549-ACE2-TMPRSS2 cells were transfected with RAB9A-targeting or NT siRNA pools. The efficiency of RAB9A depletion was determined by RT-qPCR. D) The cell viability of these cells was determined using the CellTiter-Glo 2.0 kit (Promega). E) 48 h post siRNA transfection, the cells were infected with propagation-deficient VSV pseudotypes coding for GFP that were pseudotyped with SARS-CoV-2 S (VSVΔG-S) or VSV G (VSVΔG-G) as a control[139]. 24 h.p.i. pseudovirus entry was quantified by fluorescence microscopy utilizing a Zeiss Celldiscoverer7 microscope followed by quantification of the images. To this end, a random forest classifier that was trained in CellProfiler Analyst and employed in CellProfiler 4.2.1 was used. F) To confirm the results of the pseudovirus infection, A549-ACE2 and A549-ACE2-TMPRSS2 cells were depleted of RAB9A as described in C. Subsequently, the cells were infected with SARS-CoV-2 (strain BavPat1/2020; MOI 2). 24 h.p.i. the RNA of the cells was isolated and SARS-CoV-2 replication was determined by quantification of subgenomic Leader-ORF7a RNA by RT-qPCR. In all panels, data points indicate the results of one independent experimental replicate and were normalized to the values obtained for NT siRNA-treated cells. Error bars represent the SEM. Statistical significance was determined by unpaired t test (A), ordinary one-way ANOVA with Šidák test (C, D, F) or two-way ANOVA with Tukey test (E). FC, fold change.

V.4 RAB9A is not involved in SARS-CoV-2 attachment but regulates the internalization of SARS-CoV-2 virions

The endocytic entry route can be sub-divided into distinct stages, such as the attachment, the internalization, and fusion of virions. In order to understand the relevance of RAB9A for SARS-CoV-2 attachment and entry, A549-ACE2 cells were depleted of RAB9A or not, followed by infection with SARS-CoV-2 for 1 h in 4°C to synchronize the entry process. The cells were washed and either fixed immediately to study effects on virion attachment, or treated with cycloheximide to prevent the initiation of RNA replication followed by a shift of the cells to 37°C to allow the internalization of virions. Naïve A549 cells (A549 WT) that lack ACE2 expression were used as a control for this experiment. The viral N protein was visualized by immunostaining and fluorescence microscopy. When the cells were fixed directly after the incubation with SARS-CoV-2 for 1 h in 4°C, the attachment of virions to the cell boundaries was clearly visible (Figure 13; 0 h.p.i.). Interestingly, this was also the case in A549 WT, indicating that ACE2 is dispensable for the attachment of the virus that might be regulated by other factors such as proteoglycans[165] (Figure 13; 0 h.p.i.). When the cells were subsequently shifted to 37°C for 2 h a stark change in the N signal was observed, that now resembled discrete cytosolic puncta, likely representing endosomes loaded with SARS-CoV-2 virions (Figure 13; 2 h.p.i.). These puncta were only observed in cells expressing ACE2, highlighting the importance of ACE2 for the internalization of virions (Figure 13; 2 h.p.i.).

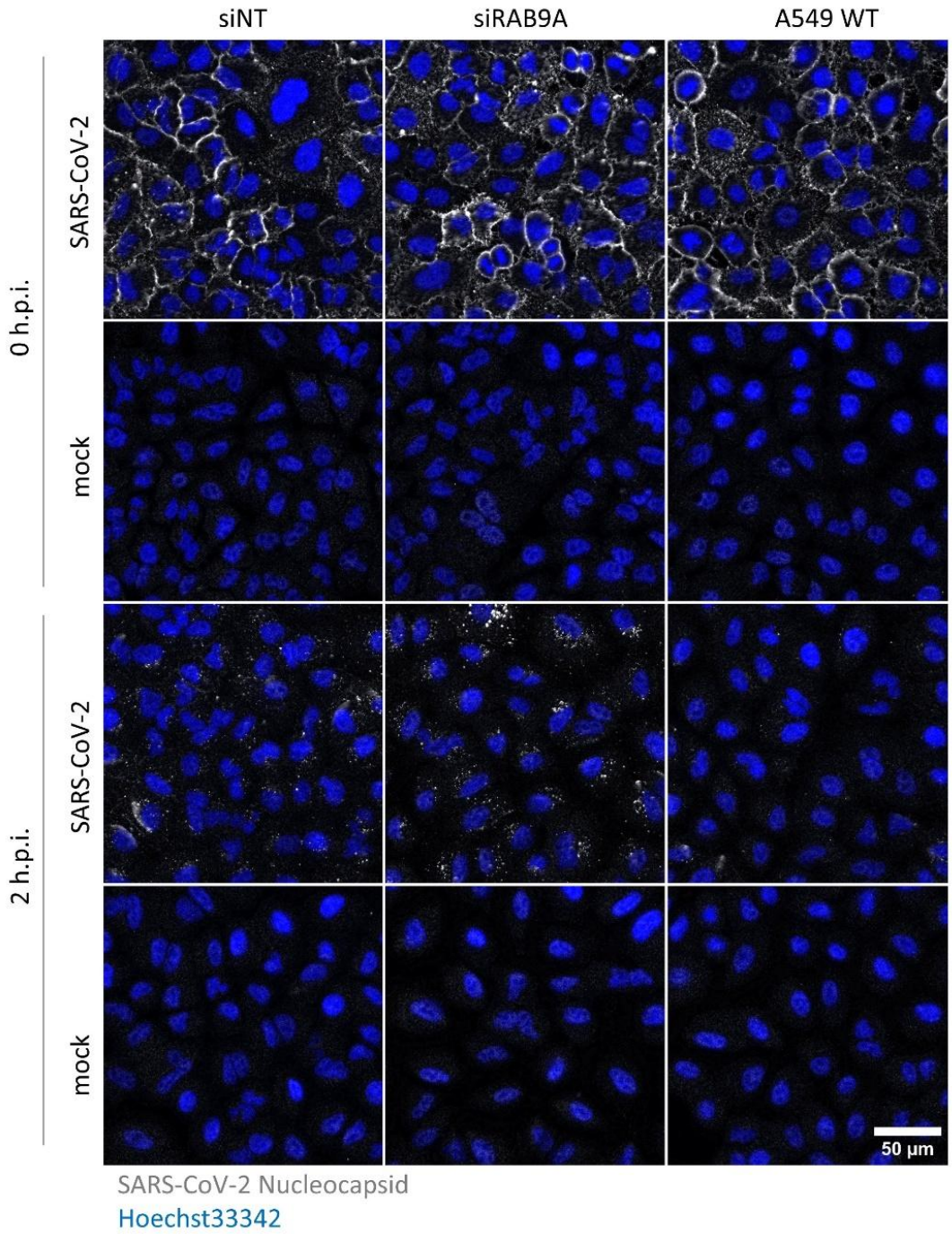

Figure 13: RAB9A depletion induces an accumulation of SARS-CoV-2 virions during entry. To understand the importance of RAB9A for the attachment and internalization of SARS-CoV-2, A549-ACE2 cells were transfected with RAB9A-targeting (siRAB9A) or NT siRNA pools (siNT). Naïve A549 (A549 WT) were used as a control. 48 h.p.t. the cells were inoculated with SARS-CoV-2 (strain: BavPat1/2020; MOI 50) and subsequently incubated 1 h in 4°C to synchronize the entry process. The cells were washed and either directly fixed to study the impact of RAB9A on virion binding (0 h.p.i.), or treated with 1 mM cycloheximide to prevent the initiation of RNA replication and shifted to 37°C for 2 h to allow the internalization of virions (2 h.p.i.), followed by extensive washing and fixation. The SARS-CoV-2 N protein was visualized by immunostaining and micrographs were acquired using a Zeiss Celldiscoverer7 microscope. Representative micrographs are shown. N=3 independent experiments were performed.

A quantification of cell-bound SARS-CoV-2 (representative images in Figure 13; 0 h.p.i.) by measuring the total N signal intensity revealed no significant differences between cells depleted of RAB9A or transfected with NT siRNA (Figure 14 A). To understand the impact of RAB9A for the internalization of SARS-CoV-2, the number of N-positive foci in the cells (representative images in Figure 13; 2 h.p.i.) were counted using machine learning. This revealed a significant increase in N-positive foci in SARS-CoV-2 infected cells that were previously depleted of RAB9A, likely indicating an intracellular retention of virions that might be unable to escape the endosomal compartment (Figure 14 B). Using RT-qPCR as an alternative read-out for both, binding and internalization, fully confirmed the observations made using microscopy (Figure 14 C and D). In addition, RAB9A did not influence the binding of SARS-CoV-2 to its target cells at different virus titers (Figure 14 E).

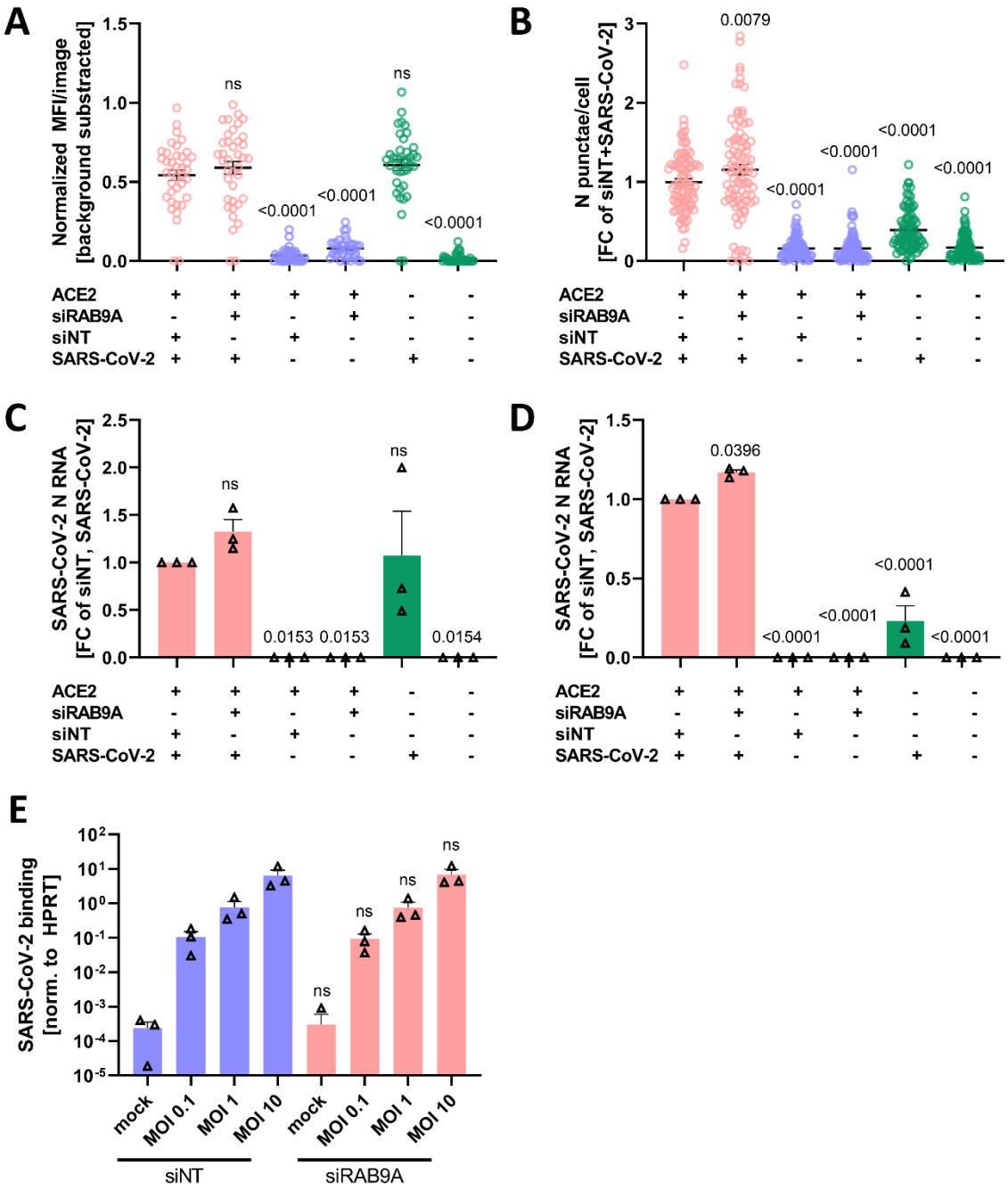

Figure 14: RAB9A regulates the internalization of SARS-CoV-2. To study the relevance of RAB9A for the binding and internalization of SARS-CoV-2, A549-ACE2 cells were transfected with 35 nM RAB9A-targeting or NT siRNA pools. A) Upon 48 h of depletion, the cells were infected with SARS-CoV-2 (strain: BavPat1/2020; MOI 50) and incubated 1 h at 4°C to synchronize the infection. Naïve A549 cells served as a control to test the importance of ACE2 for binding and internalization, respectively. After the incubation period, the cells were extensively washed, fixed and immunostained for the viral N protein. The total fluorescence intensity of the N signal was determined. B) The cells were infected as described in A. After the incubation at 4°C, the cells were extensively washed, treated with 1 mM cycloheximide to prevent the initiation of viral translation, and shifted to 37°C for 2 h to allow the internalization of the virus. Pixel classification in Ilastik and subsequent quantification of the segmentation using the "Identify primary objects" module in CellProfiler 4.2.1 were employed to quantify the number of N-positive puncta in the images. C) To corroborate the microscopy results, A549-ACE2 cells were transfected and infected as described above (MOI 10). After 1 h in 4°C, the total RNA of the cells was isolated and bound genomic SARS-CoV-2 RNA was quantified by RT-qPCR. D) The

cells were treated and infected as in C. After 1 h in 4°C, the cells were washed extensively and treated with 1 mM cycloheximide to prevent the onset of translation and replication. The cells were shifted to 37°C to allow the internalization of virions. After 2 h the total RNA of the cells was extracted and internalized viral RNA was quantified by RT-qPCR. E) To exclude the possibility that RAB9A supports virus binding at different virus concentrations, A549-ACE2 cells were depleted of RAB9A and subsequently infected with SARS-CoV-2 (strain: BavPat1/2020) at different MOIs. Virus binding was quantified after extensive washing by extraction of total RNA and measurement of bound viral genomic RNA by RT-qPCR. Error bars represent the SEM. Each data point in A and B represents one analyzed image from N=3 independent biological experiments. Each data point in C-E represents the results of one independent biological replicate. Statistical analysis was performed by ordinary one-way ANOVA with Dunnett test (A-D) or ordinary one-way ANOVA with Šídák test (E). FC, fold change.

Since SARS-CoV-2 binding did not depend on the presence of ACE2 (Figure 14 A, C), I next tested the impact of RAB9A depletion on surface-resident ACE2. To this end HeLa-ACE2 cells that have higher surface ACE2 levels than A549-ACE2 cells were transfected with RAB9A-targeting, ACE2-targeting or NT siRNA pools. HeLa wild-type cells that lack endogenous ACE2 expression served as a control. First, I confirmed that ACE2 is efficiently down-regulated by siRNA transfection and that HeLa wild-type cells do not express ACE2 (Figure 15 A). 48 h.p.t., surface-resident ACE2 was immunostained on life cells and quantified by flow cytometry. ACE2 depletion resulted in a moderate decrease in the MFI and proportion of ACE2-positive cells (Figure 15 B, C). The magnitude of the phenotype could be influenced by the sub-optimal depletion of ACE2 in HeLa cells with ectopic ACE2 expression (Figure 15 A). As expected, the surface-resident ACE2 signal was greatly reduced in HeLa wild-type cells (Figure 15 B, C) while depletion of RAB9A did not impact the levels of ACE2 on the plasma membrane (Figure 15 B, C). This indicates that the mechanism by which RAB9A promotes SARS-CoV-2 infection is independent of virion binding, receptor expression and trafficking and therefore also differs from the mechanism-of-action that is reported for RAB7A[79]. Instead, RAB9A seems to be involved in the endocytic transport of SARS-CoV-2 virions.

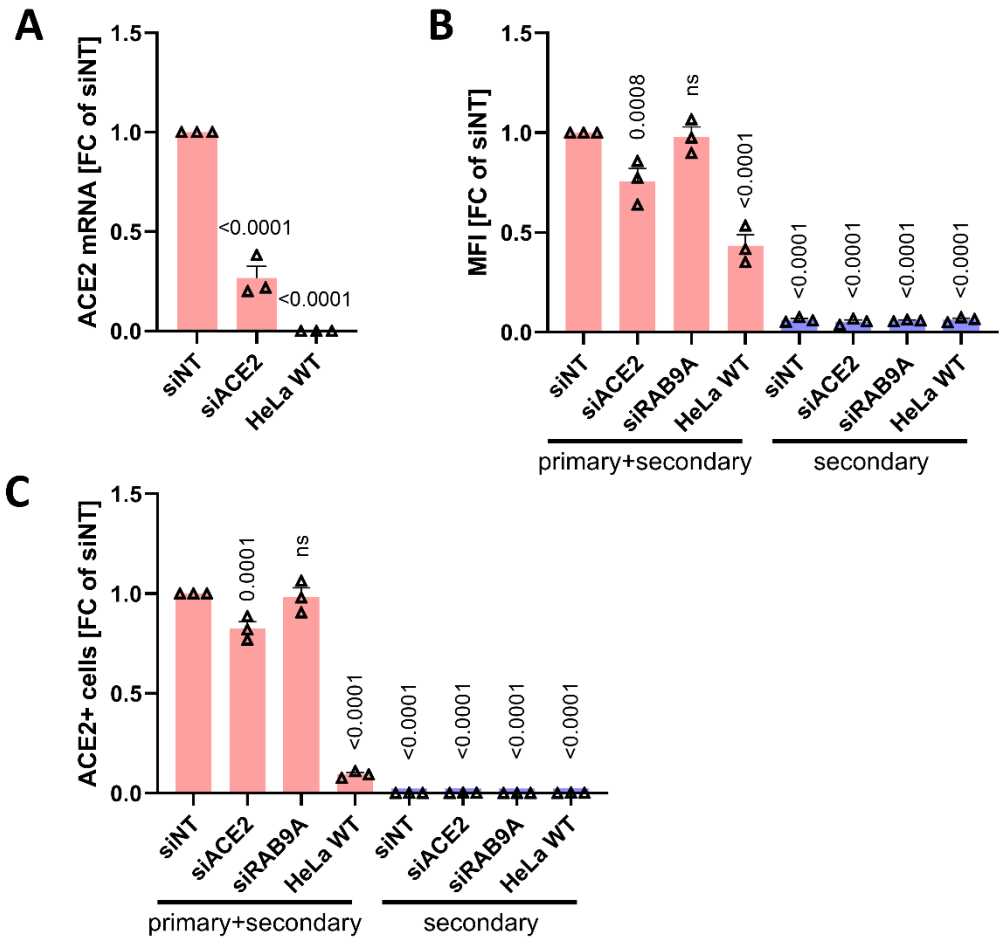

Figure 15: RAB9A does not influence intracellular ACE2 trafficking. A) HeLa-ACE2 cells were transfected with 35 nM RAB9A, ACE2 or NT siRNA pools. HeLa wild-type cells served as a control. 48 h.p.t. the efficiency of ACE2 depletion was determined by RT-qPCR. B) Surface ACE2 was stained on life cells and quantified by flow cytometry. The mean fluorescence intensity is shown. C) The proportion of ACE2-positive (ACE2+) cells was determined by flow cytometry. In all panels, one data point represents the mean of one experimental replicate. Error bars represent the SEM. Statistical analysis was performed by ordinary one-way ANOVA with Dunnett test (A-C). FC, fold change.

V.5 RAB9A depletion leads to accumulation of SARS-CoV-2 in the endo-lysosomal compartment

In order to confirm the role of RAB9A during the escape of SARS-CoV-2 from the endo-lysosomal compartment, I conducted an entry kinetic in A549-ACE2 cells that were depleted of RAB9A or not and stained the cells for SARS-CoV-2 N and the late endosome and lysosome marker LAMP1. A549 wild-type cells that do not express ACE2 served as a control. In brief, the cells were inoculated with SARS-CoV-2 and incubated 1 h in 4°C to synchronize the infection. Next, the cells were extensively washed and treated with 1 mM cycloheximide to prevent the initiation of viral translation and shifted to 37°C to allow the internalization of bound SARS-CoV-2. After 30 min in 37°C, discrete N-positive puncta were observed in the cell periphery in all inoculated conditions (Figure 16 A; 30 min). At this time point, N signal was still observed in wild-type A549 but the signal was lower as in ACE2-expressing A549 (Figure 16 A; 30 min). No co-localization of N and LAMP1 was observed (Figure 16 A; 30 min). After 60 min in 37°C, the number of N-positive puncta decreased and the existing puncta exhibited an increase in fluorescence intensity (Figure 16 A; 60 min). In addition, the puncta grew larger in size (Figure 16 A; 60 min). After 60 min no N signal was observed in SARS-CoV-2 infected A549 wild-type (Figure 16 A; 60 min). After 180 min in 37°C, just few N-positive puncta with strong fluorescence intensity were observed in the perinuclear region, likely representing SARS-CoV-2-loaded late endosomes (Figure 16 A; 180 min). As expected, the calculation of the Mander's co-efficient confirmed the lack of co-localization between N and LAMP1 after 30 min (Figure 16 B; 30 min). Interestingly, co-localization of N and LAMP1 was reduced in cells depleted of RAB9A after 60 min, possibly indicating deficits in the sub-cellular trafficking of the virions (Figure 16 B; 60 min). However, after 180 min increased co-localization between N and LAMP1 was observed in RAB9A-depleted cells (Figure 16 B; 180 min). This could indicate deficits during viral fusion which would explain the retention of virions in the endolysosomal compartment.

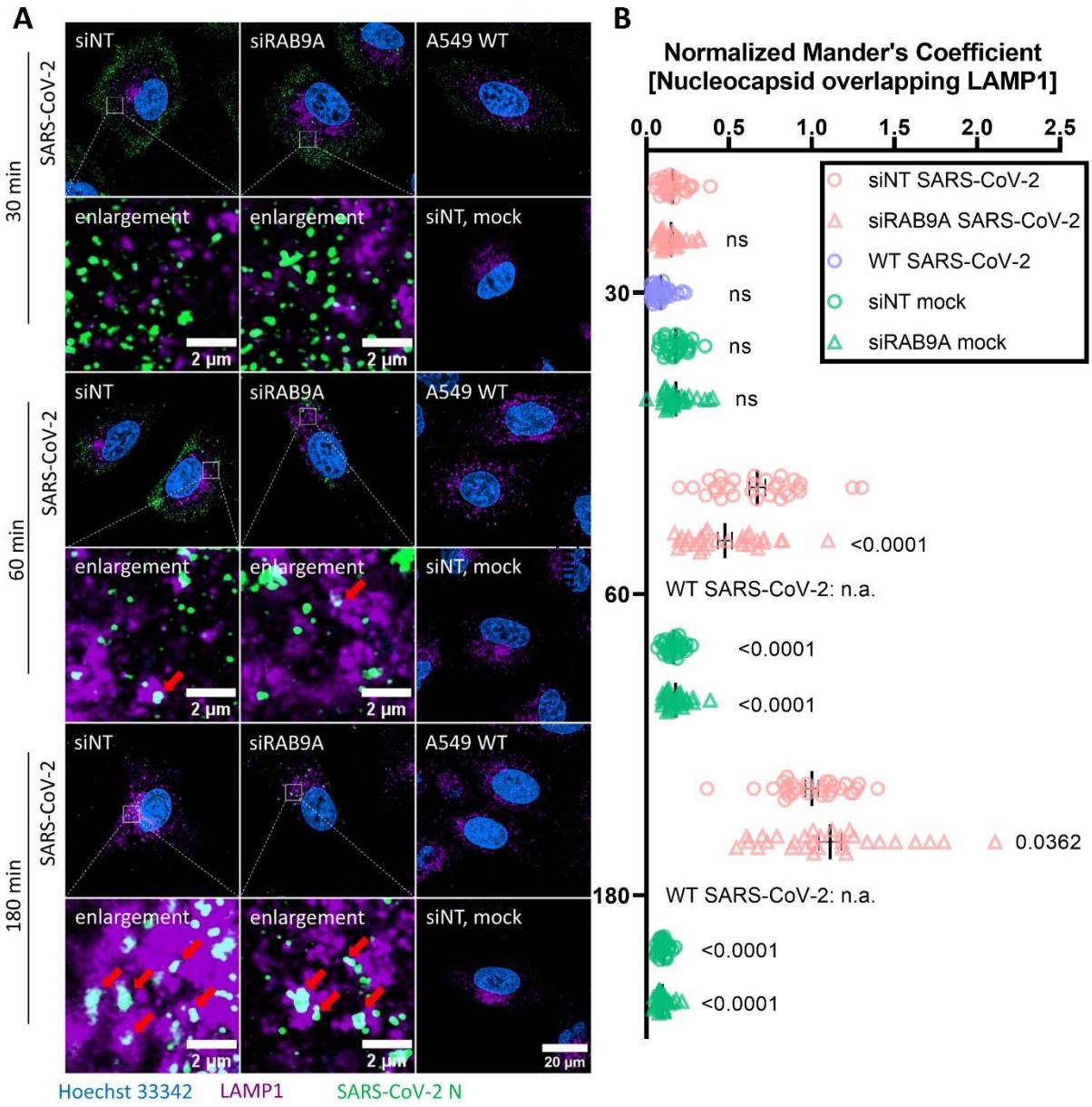

Figure 16: RAB9A depletion increases the co-localization of incoming SARS-CoV-2 with the lysosomal marker LAMP1. A) To determine the co-localization of incoming SARS-CoV-2 with the lysosome marker LAMP1, A549-ACE2 cells were transfected with 35 nM RAB9A-targeting or NT siRNA pools. 48 h.p.t. the cells were inoculated with SARS-CoV-2 (strain: BavPat1/2020; MOI 50). To synchronize the infection, the cells were incubated 1 h in 4°C. Afterwards, the cells were extensively washed, treated with 1 mM cycloheximide to prevent the initiation of viral translation and shifted to 37°C to allow the internalization of bound SARS-CoV-2. After 30, 60 or 180 min the cells were fixed and immunostained for LAMP1 and SARS-CoV-2 N. Micrographs were acquired using super-resolution microscopy using a Zeiss LSM900 microscope with Airyscan 2. Representative micrographs are shown. Enlarged areas are depicted under the corresponding overview micrograph. Red arrows indicate co-localization of N and LAMP1. B) Quantification of the co-localization of N and LAMP1 was performed by calculation of the Mander's co-efficient (N overlapping LAMP1). N=30 images from 3 independent experiments were quantified. Each data point shows the co-localization in one image. SARS-CoV-2 infected A549-ACE2 are depicted in pink, SARS-CoV-2 infected A549 wild-type cells lacking ACE2 expression in blue and mock infected A549-ACE2 are shown in green. SARS-CoV-2 infected A549 wild-type cells were only analyzed for the 30 min time point since the signal at the later time points did not allow

reliable quantification of co-localization due to low N signal. Error bars represent the SEM. Statistical significance was determined by 2-way ANOVA with Dunnett test (B).

V.6 The proviral RAB9A activity is supported by DENND2D

The activity of RAB GTPases in the trafficking of intracellular membranes depends on the hydrolysis of GTP to GDP[166]. The exchange of GDP to GTP, converting RAB GTPases from their inactive GDP-bound state to their active GTP-bound state, is catalyzed by GEFs and the hydrolysis of GTP is triggered by GTPase-activating proteins (GAPs)[121]. In the case of RAB9A, DENND2 proteins catalyze the exchange of GDP to GTP[127]. Two DENND2 isoforms have been shown to be able to selectively activate RAB9A: DENND2A and DENND2D (Figure 17 A)[122,127]. To understand if the GTPase activity of RAB9A is required to exert its proviral effect, I depleted A549-ACE2 cells of DENND2A and DENND2D, respectively. The knock-down was efficient for both factors (Figure 17 B, C) and significant but only marginal effects on the viability of the transfected cells were observed (Figure 17 D, E). Interestingly, DENND2A depletion did not impact SARS-CoV-2 replication (Figure 17 F) while DENND2D depletion reduced the levels of viral subgenomic Leader-ORF7 RNA to a similar extent as RAB9A depletion (Figure 17 G and Figure 12 F). To understand if DENND2D acts at the same stage of the viral life cycle as RAB9A, I depleted A549-ACE2 cells of DENND2D and quantified the entry of VSV that was pseudotyped with the SARS-CoV-2 S protein or the VSV G protein as a control. A significant reduction of VSVΔG-S entry was evident in A549-ACE2 cells depleted of DENND2D but the entry of VSVΔG-G was equally reduced, thus precluding clear conclusions about the role of DENND2D during entry (Figure 17 H). To confirm that DENND2D acts during an early stage of SARS-CoV-2 infection, I therefore infected A549-ACE2 cells that were previously transfected with DENND2D-targeting or NT siRNA pools with SARS-CoV-2 and terminated the infection after 8 h to exclude the possibility of virus spread and to exclusively interrogate the role of DENND2D during entry and replication. Already 8 h.p.i., DENND2D depletion resulted in a significant reduction of SARS-CoV-2 infected cells, indicating that similarly to RAB9A DENND2D acts during an early stage of the viral life cycle (Figure 17 I, J). In summary, these findings indicate that the GTPase activity of RAB9A is likely required to support SARS-CoV-2 entry and that the proviral activity of RAB9A requires the activity of DENND2D.

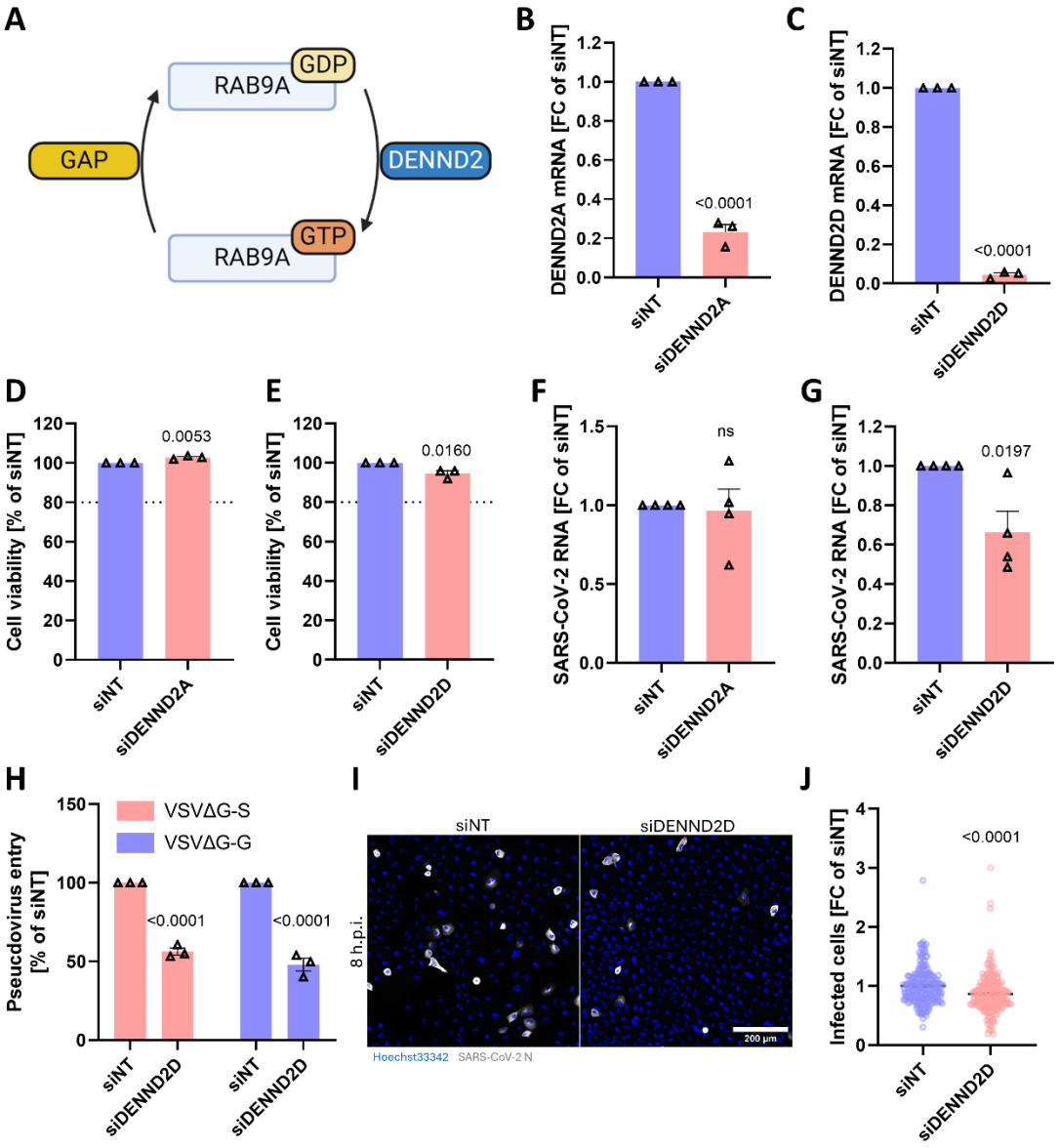

Figure 17: RAB9As GTPase activity is required for its proviral function and is supported by DENND2D. A) Schematic representation of the role of DENND2 proteins in the exchange of GDP to GTP on RAB9A, converting it from its inactive to active form. The schematic was created using BioRender.com. B, C) A549-ACE2 cells were transfected with 35 nM siRNA pools targeting DENND2A (B) or DENND2D (C) or NT siRNA pools as a control. The knock-down efficiency was quantified by RT-qPCR. D, E) Effects of DENND2A (D) and DENND2D (E) depletion on the cell viability were quantified using the CellTiter-Glo 2.0 kit (Promega). F, G) 48 h.p.t., the siRNA-transfected cells were infected with SARS-CoV-2 (strain: BavPat1/2020; MOI 1). 24 h.p.i. the intracellular RNA of the cells was extracted and viral replication determined by RT-qPCR against subgenomic Leader-ORF7 RNA. H) A549-ACE2 cells were transfected with DENND2D-targeting or NT siRNA pools. 48 h.p.t. the cells were infected with GFP-encoding VSV pseudotypes that were enveloped either with the SARS-CoV-2 S protein (VSVΔG-S) or the VSV G protein (VSVΔG-G) as a control. 24 h.p.i. pseudovirus entry was quantified by fluorescence microscopy. Quantification was performed using thresholding of the GFP signal in CellProfiler 4.2.1 (Broad Institute). I) A549-ACE cells were transfected with DENND2D-targeting or NT siRNA pools. 48 h.p.t. the cells were infected with SARS-CoV-2 (strain: BavPat1/2020; MOI 5). The cells were fixed 8 h.p.i. to exclude the possibility of virus spread. Immunostaining of the SARS-CoV-2 N protein was performed to quantify SARS-CoV-2 infection. Representative micrographs are shown. J) Quantification of the percentage of infected cells in I) using thresholding of the N signal

in CellProfiler 4.2.1 (Broad Institute). In B-H each data point represents an independent experimental replicate. In I and J, N=3 independent experimental replicates were conducted. Each data point in J represents one analyzed image. Error bars indicate the SEM. Statistical significance was determined using unpaired t-tests (B-G, J) or two-way ANOVA with Šídák-test (H). FC, fold change.

V.7 Cathepsin maturation is regulated independently of RAB9A

RAB9A was previously proposed to be involved in the post-translational processing of cathepsin proteases that is required to convert these proteases into their active form[167]. Cathepsins have been shown to mediate the proteolytical activation of S during endocytic entry and deficits in their maturation could therefore lead to reduced fusion during entry and induce an accumulation of virions in the endo-lysosomal compartment[54,66]. After translation the immature procathepsin is processed to single-chain cathepsin in the trans-Golgi network followed by a second autoproteolytic activation in the late endosome which is catalyzed by the acidic environment in this compartment[68]. Therefore, I interrogated the role of RAB9A during the maturation of CTSL and CTSB. To this end, A549-ACE cells were transfected with RAB9A-targeting or NT siRNA pools. 24 h.p.t. the control cells were treated with ammonium chloride to de-acidify the endosomal compartment and therefore stall the maturation of both cathepsins. RAB9A was efficiently depleted by siRNA transfection (Figure 18 A, B). The proteolytic activation of CTSL and CTSB was efficiently prevented by ammonium chloride treatment (Figure 18 A, C) but no impact of RAB9A on the relative abundance of mature CTSL and CTSB (Figure 18 C) or the total CTSL and CTSB content in the cells (Figure 18 D) was found. This indicates that RAB9A supports SARS-CoV-2 entry by a mechanism independent of the maturation of cathepsin proteases.

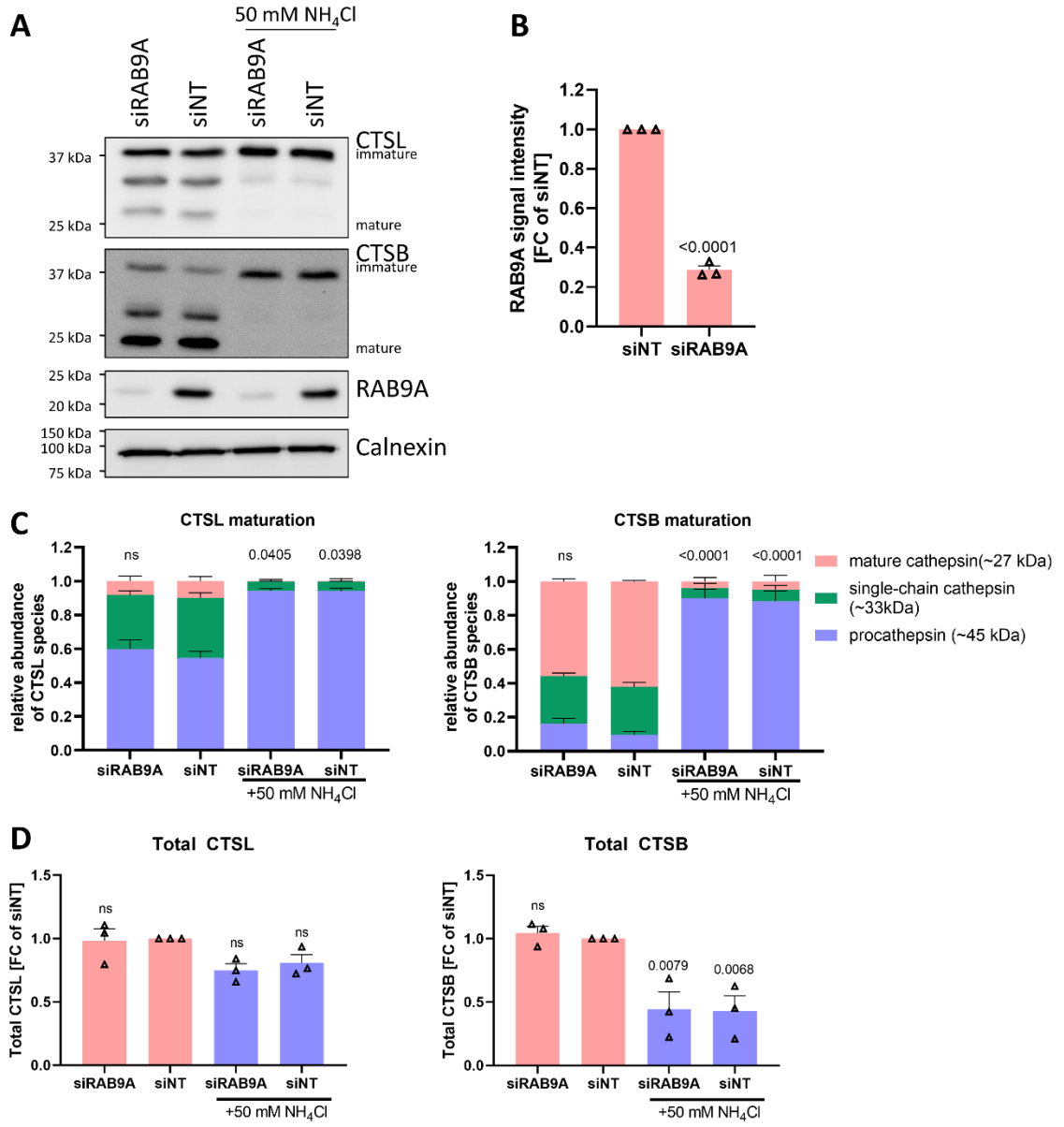

Figure 18: Cathepsins L and B mature independently of RAB9A. A) A549-ACE2 cells were transfected with 35 nM RAB9A-targeting or NT siRNA pools. 24 h.p.t. control cells were treated with 50 mM ammonium chloride to de-acidify the endosomes and stall the acidity-dependent maturation of cathepsins L and B. 48 h.p.t. the cell lysates were harvested and cathepsin L (CTSL), B (CTSB) and RAB9A expression were analyzed by Western Blot. Calnexin was used as a loading control. A representative Western Blot is shown. B) The efficiency of RAB9A depletion on protein level was quantified in A. C) The relative abundances of procathepsin, single-chain cathepsin and mature CTSL and CTSB were quantified from A. P-values indicate differences in the abundance of mature CTSL or CTSB. D) The total amount of CTSL and CTSB was calculated from A. Error bars represent the SEM. Each data point in B-D represents the results of an independent biological replicate. The statistical significance was determined by unpaired t-test (B), 2-way ANOVA with Dunnett test (C) or ordinary one-way ANOVA with Dunnett test (D). The values in B-D are normalized to those obtained from cells transfected with NT siRNA. FC, fold change.

In a previous study the authors demonstrated that the function of RAB9A during the maturation of cathepsins can be compensated by the endosomal RAB7A GTPase in RAB9A-KO cells[168]. To test for such compensation in the cellular model used in this study, I performed co-

transfections of RAB9A- and RAB7A-targeting siRNA pools into A549-ACE2 cells and investigated the maturation of cathepsin proteases. While the depletion of RAB7A and RAB9A by siRNA transfection into A549-ACE2 cells was very efficient, I observed an upregulation of RAB9A expression upon RAB7A depletion (Figure 19 B), possibly indicating the existence of a feedback loop that regulates the expression or degradation of RAB9A in the absence of RAB7A. Neither the depletion of RAB7A nor the co-depletion of RAB7A and RAB9A influenced the maturation of both, CTSL and CTSB (Figure 19 A, C). While no impact of the co-depletion of both GTPases was found on the relative abundance of CTSL and CTSB, the total cellular CTSL content was reduced in A549-ACE2 cells depleted of RAB7A or RAB7A and RAB9A (Figure 19 A, D), indicating that mainly RAB7A plays an important role during cathepsin maturation. Co-depletion of RAB7A and RAB9A did therefore not influence the relative abundance of mature CTSL and CTSB and their precursors but reduced the total abundance of CTSL, leading to a reduction of mature CTSL in the endosomal compartment which could in turn reduce the efficiency of SARS-CoV-2 fusion during the endocytic entry. However, besides the up-regulation of RAB9A in RAB7A-depleted cells no further evidence for a compensatory mechanism was found.

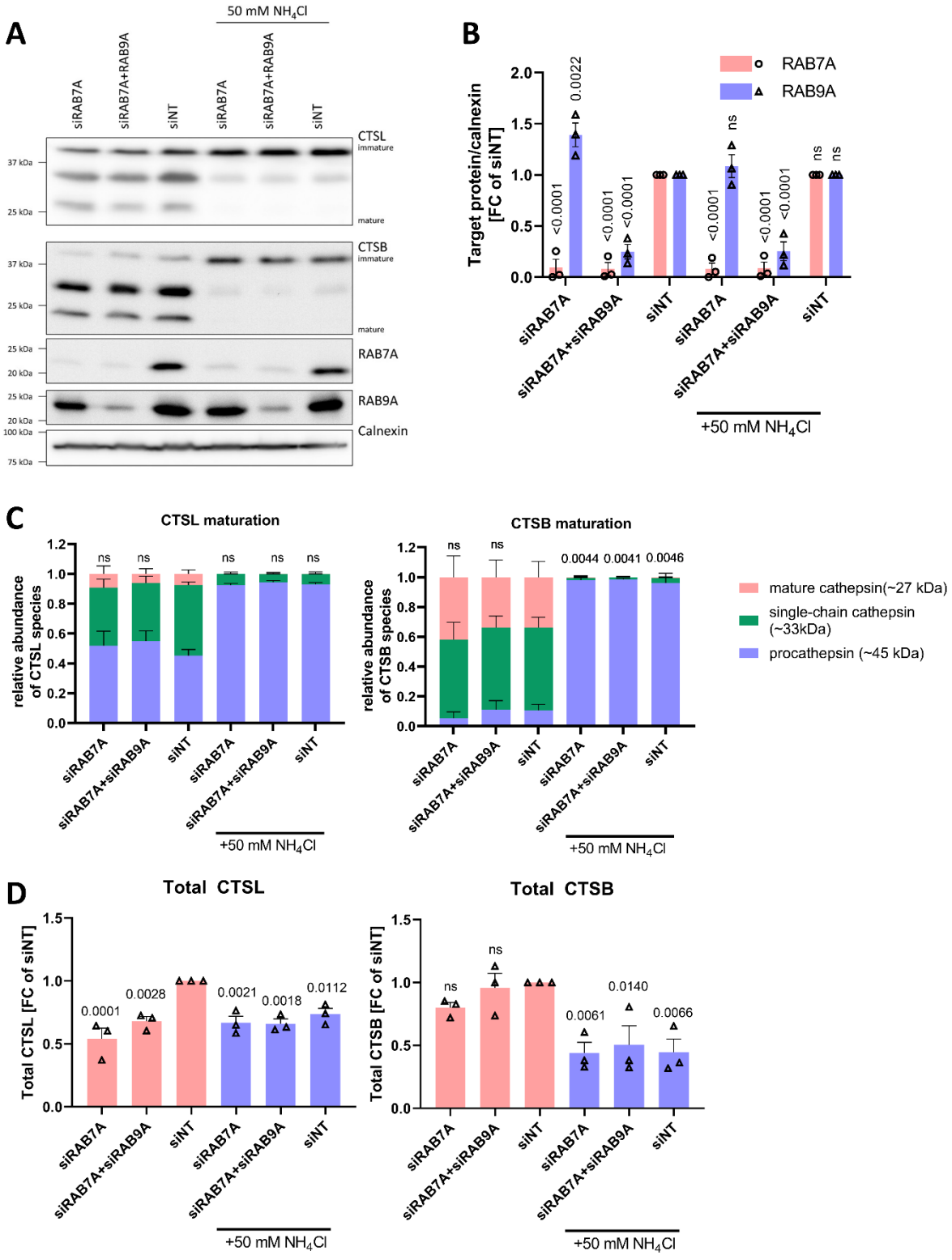

Figure 19: In contrast to RAB9A, RAB7A supports the intracellular maturation of cathepsin proteases. A549-ACE2 cells were transfected with siRNA pools targeting RAB7A, RAB9A and RAB7A or NT siRNA pools. 35 nM siRNA were used for single pool transfections while 17.5 nM of each siRNA pool were used for double knock-down, resulting in a total siRNA concentration of 35 nM per condition. 24 h.p.t. the control cells were treated with 50 mM ammonium chloride to deacidify the endo-lysosomal compartment and stall cathepsin maturation. 48 h.p.t. the cell lysates were harvested and

immunoblotting was used to quantify the expression of CTSL, CTSB, RAB7A and RAB9A. Calnexin was used as a loading control. A representative Western Blot is shown. B) Quantification of the knock-down efficiency of RAB9A and RAB7A on protein level. The indicated values were normalized to the calnexin control and to cells transfected with NT siRNA pools. C) The relative abundance of different CTSL and CTSB species was quantified in A. P-values indicate differences between mature CTSL and CTSB, respectively. D) Total CTSL and CTSB values were quantified by calculating the sum of the three cathepsin species in A. Error bars represent the SEM. N=3 independent experimental replicates were performed. Statistical significance was calculated by two-way ANOVA with Dunnett test (B, C) or ordinary one-way ANOVA with Dunnett test (D). FC, fold change.

V.8. Lysosome morphology and biogenesis are regulated by RAB9A

Previous reports suggest an involvement of RAB9A in the biogenesis of lysosomes[123], which could influence the ability of viruses to fuse with the endosomal membrane. To understand if the endo-lysosomal compartment undergoes changes in RAB9A depleted cells, I transfected A549-ACE2 cells with RAB9A-targeting or NT siRNA pools. 24 h.p.t. the control cells were treated with 10 nM Bafilomycin A1 to interfere with endosome acidification. On the next day the cells were stained with the pH-sensitive dye Lysotracker Red DND-99 that allows the visualization of acidic intracellular compartments. Lysotracker Red DND-99 fluorescence was efficiently suppressed by Bafilomycin A1 treatment, confirming the pH-dependency of the signal (Figure 20 A, B). In addition, the cytometric analysis revealed a significant increase in Lysotracker signal intensity in cells transfected with RAB9A-targeting siRNA (Figure 20 A, B). To understand if this increase in signal intensity stems from enlarged lysosomes, larger quantities of lysosomes or an increased fluorescence intensity in the existing lysosomes, I employed confocal fluorescence microscopy to study morphological changes in the cellular lysosome population. While no changes in the number of lysosomes per cell or the Lysotracker intensity was found, a significant enlargement of the lysosomes was evident in RAB9A-depleted cells (Figure 20 C-F). In summary, these findings confirm an involvement of RAB9A in the morphogenesis of the endo-lysosomal compartment which could in turn impact the efficiency of virus fusion with the endosomal membranes. Importantly, a dysregulation of late endosome biogenesis was previously shown by others, but the authors observed smaller endosomes in cells depleted of RAB9A[124].

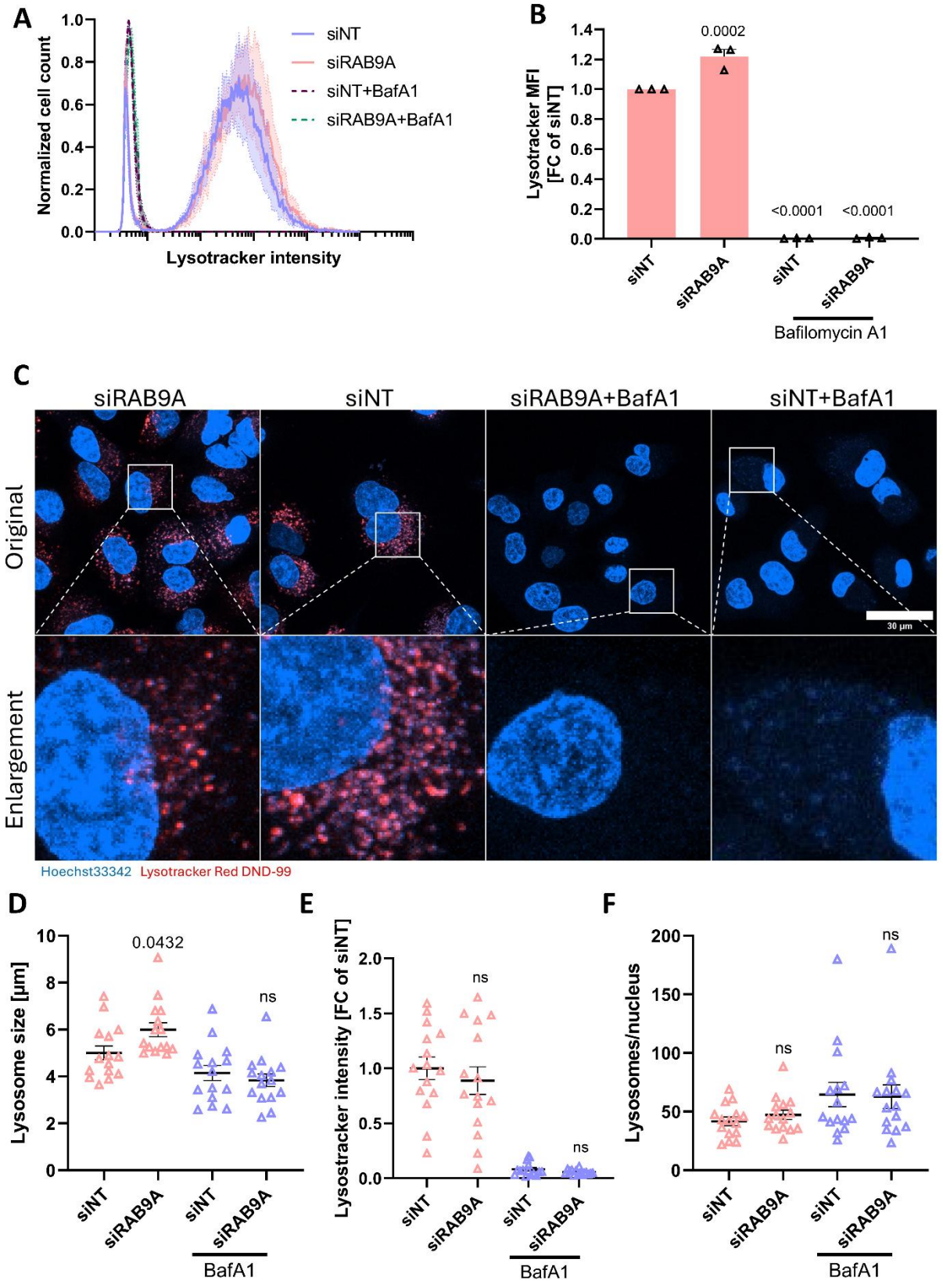

Figure 20: Lysosome size is regulated by RAB9A. A) A549-ACE2 cells were transfected with 35 nM RAB9A-targeting or NT siRNA pools. 24 h.p.t. control cells were treated with 10 nM of the lysosomotropic agent Bafilomycin A1 to interfere with lysosome acidification. 48 h.p.t. the cells were stained with the pH-sensitive dye Lysotracker Red DND-99 and analyzed by flow cytometry. A histogram showing the fluorescence intensity of the analyzed cells from three independent experiments

is shown. The shaded areas indicate the SEM. B) The mean Lysotracker Red DND-99 fluorescence intensity of the analyzed cells was quantified by flow cytometry. Each data point represents mean results of one independent biological experiment. C) To study morphological alterations in the intracellular lysosome population, confocal fluorescence microscopy was used. A549-ACE2 cells were transfected with RAB9A targeting or NT siRNA and treated with Bafilomycin A1, as described in A. Life cells were used for imaging. Z-stacks with 0.2 µm intervals were acquired. Representative maximum projections are depicted. The size (D), intensity (E) and quantity (F) of Lysotracker Red DND-99 stained lysosomes were quantified in the images shown in B. Error bars indicate the SEM. Data points in D-F indicate one analyzed image from N=3 independent experimental replicates. Statistical significance was determined by ordinary one-way ANOVA with Holm-Šídák test (B) or ordinary one-way ANOVA with Šídák test (D-F). FC, fold change.

V.9 RAB9A supports the fusion of SARS-CoV-2 virions with the membrane of the late endosome

The intracellular accumulation of virions (Figure 14 B, D) and the increase in co-localization of these virions with the lysosomal marker LAMP1 (Figure 16 A, B) in the absence of RAB9A indicate deficits in fusion during the endocytic entry of SARS-CoV-2. In order to confirm this, I transfected HeLa-ACE cells with RAB9A-targeting or NT siRNA pools. 46 h.p.t. the control cells were treated with the broad-spectrum cathepsin inhibitor E64-d to stall the activation of the S protein and to prevent the subsequent fusion of virions with the endosomal membrane[67]. To specifically interrogate virus fusion, I employed a previously described lentiviral pseudotype system that uses lentiviral particles containing a fusion protein of HIV-1 vpr and β-lactamase that upon completed fusion converts a fluorescence resonance energy transfer-enabled substrate with two fluorophores linked by a cephalosporin core in the infected cells, allowing an efficient quantification of pseudovirus fusion[158,169,170]. To control for effects not specific for fusion, I used lentiviral pseudotypes enveloped with the VSV G protein or without viral glycoprotein. 48 h.p.t. the cells were inoculated with the lentiviral pseudotype suspension for two hours, washed, loaded with CCF2-AM and incubated 16 h in 11°C to stall further virus fusion but allow the metabolization of CCF2-AM. After the incubation time, the cells were detached and analyzed by flow cytometry (Figure 21 A).

First, I confirmed efficient RAB9A depletion in HeLa-ACE2 cells on protein level (Figure 21 B, C). Using lentiviral pseudotypes enveloped with the SARS-CoV-2 S or VSV G protein, I was able to observe significant fusion with the target cells (Figure 21 D; VSV G and Spike) which was not the case for pseudotypes lacking a viral glycoprotein (Figure 21 D; no gp). As evidenced by the absence of signal in naïve HeLa cells, ACE2 was required for the fusion of lentiviral pseudotypes carrying the SARS-CoV-2 S protein (Figure 21 D; wt, Spike). In addition, fusion of S containing pseudotypes was efficiently suppressed by pre-treatment of the

cells with the cathepsin inhibitor E64-d, which specifically interferes with the fusion of virions that have entered the endocytic pathway (Figure 21 D; E64-d, Spike). RAB9A depletion had no impact on the fusion of pseudotypes enveloped with the VSV G protein or lacking a viral glycoprotein (Figure 21 E), confirming the findings made earlier using VSV pseudotypes (Figure 12 E). Importantly, the fusion of SARS-CoV-2 S containing lentivirus particles was moderately but significantly reduced in cells transfected with RAB9A-targeting siRNAs (Figure 21 F), confirming that RAB9A specifically supports the fusion of SARS-CoV-2 with the endosomal membrane.

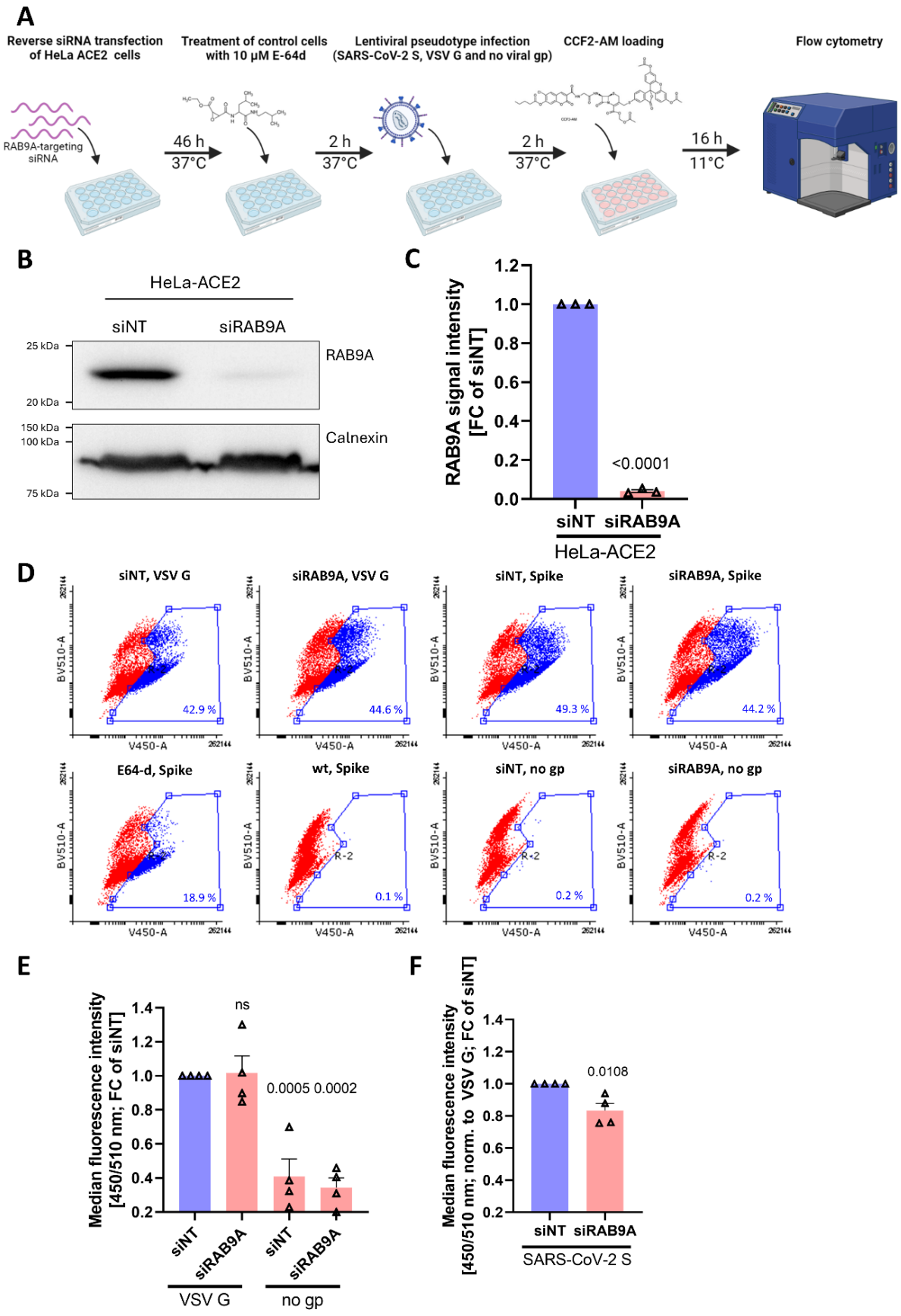

Figure 21: SARS-CoV-2 fusion with the endosomal membrane is supported by RAB9A. A) Schematic of the fusion assay employed to quantify fusion events between lentiviral pseudotypes containing active

β-lactamase within the virion and cellular membranes[170]. The lentiviral pseudotypes containing a fusion protein of HIV-1 vpr and β-lactamase were pseudotyped with the SARS-CoV-2 S protein or the VSV G protein as a control. The broad spectrum cathepsin inhibitor E64-d was used to stall S protein activation and subsequent fusion. In the event of virus fusion, the vpr-β-lactamase fusion protein will be released into the cytoplasm of the infected cell where it can metabolize the fluorescent CCF2-AM substrate, resulting in a quantifiable change in the emission spectrum of the dye[158,170]. Flow cytometry was used as a read-out. The schematic was generated using BioRender.com. B) HeLa-ACE2 cells were transfected with 35 nM RAB9A-targeting or NT siRNA pools. Immunoblotting was used to quantify the efficiency of RAB9A knock-down on protein level. C) Quantification of B. D) 46 h.p.t. the control cells were treated with 10 µM E64-d. After 2 h the cells were infected with vpr-β-lactamase containing lentiviral pseudotypes, enveloped with SARS-CoV-2 S or VSV G. Lentiviral particles without glycoprotein were used as a negative control. Representative scatter plots from the flow cytometric analysis are shown. N=4 independent experiments were conducted. E) The median fluorescence intensity (ratio of the fluorescence at 450 nm to 510 nm) of the control samples was analyzed to exclude potential effects of RAB9A depletion on the fluorescence in the control conditions. The data are shown as fold changes of cells transfected with NT siRNA pools and infected with lentiviral pseudotypes enveloped with VSV G. F) The median fluorescence intensity (ratio of 450/510 nm, normalized to VSV G pseudotype entry and the NT siRNA transfected cells) of cells infected with SARS-CoV-2 S pseudotyped lentiviruses was determined. Error bars represent the SEM. Each data point in C, E and F represents the results of one independent experiment. Statistical significance was determined by unpaired t-test (C, F) or ordinary one-way ANOVA with Dunnett test (E).

V.10 TIMM17B is a SARS-CoV-2 restriction factor that inhibits early stages of the SARS-CoV-2 life cycle

In addition to RAB9A, I have validated TIMM17B as another potential host cell factor candidate that was discovered in the meta-analysis described above (Figure 9 B, C). In order to validate the importance of TIMM17B for SARS-CoV-2 infection, I used a similar approach as for RAB9A. First, I confirmed the expression of TIMM17B in all tissues that are relevant targets of SARS-CoV-2 (Figure 10). Next, I transfected A549-ACE2 and A549-ACE2-TMPRSS2 cells with TIMM17B-targeting siRNA pools. The knock-down was highly efficient in both cell lines (Figure 22 A) and led to a significant but only marginal reduction in cell viability (Figure 22 B). Surprisingly, TIMM17B did not promote but strongly suppress SARS-CoV-2 replication in both tested cell lines (Figure 22 C). This also indicates that in contrast to RAB9A, TIMM17B restricts SARS-CoV-2 infection independently of the entry route (Figure 22 C). Therefore, I decided to validate the importance of TIMM17B in Calu-3 and HeLa-ACE2 cells. TIMM17B knock-down was very efficient in both cell lines (Figure 22 D). TIMM17B restricted SARS-CoV-2 replication in Calu-3 cells but not in HeLa-ACE2 cells (Figure 22 E), likely indicating a certain relevance of TIMM17B for SARS-CoV-2 infection in respiratory epithelial cells. Due to the higher magnitude of the phenotype observed upon TIMM17B depletion, I aimed to validate the specificity of the knock-down by transfection of A549-ACE2 cells with the single siRNAs that were included in the pools employed for previous experiments. Three out of four transfected siRNAs (#1-3) led to a strong decrease in TIMM17B expression 48 h.p.t., while one siRNA (#4) only led to a ~2-fold reduction in TIMM17B expression (Figure 22 F). No major effects of siRNA transfection on the viability of the cells was observed (Figure 22 G). Transfection of three out of four siRNAs (#2-4) resulted in reproducible increases in SARS-CoV-2 infection (Figure 22 H). To fully understand if these data indicate a specific relationship between TIMM17B expression and the cells' susceptibility to SARS-CoV-2 infection, I performed a linear regression analysis and observed a significant correlation between these two parameters (Figure 22 I), suggesting that TIMM17B restricts SARS-CoV-2 infection.

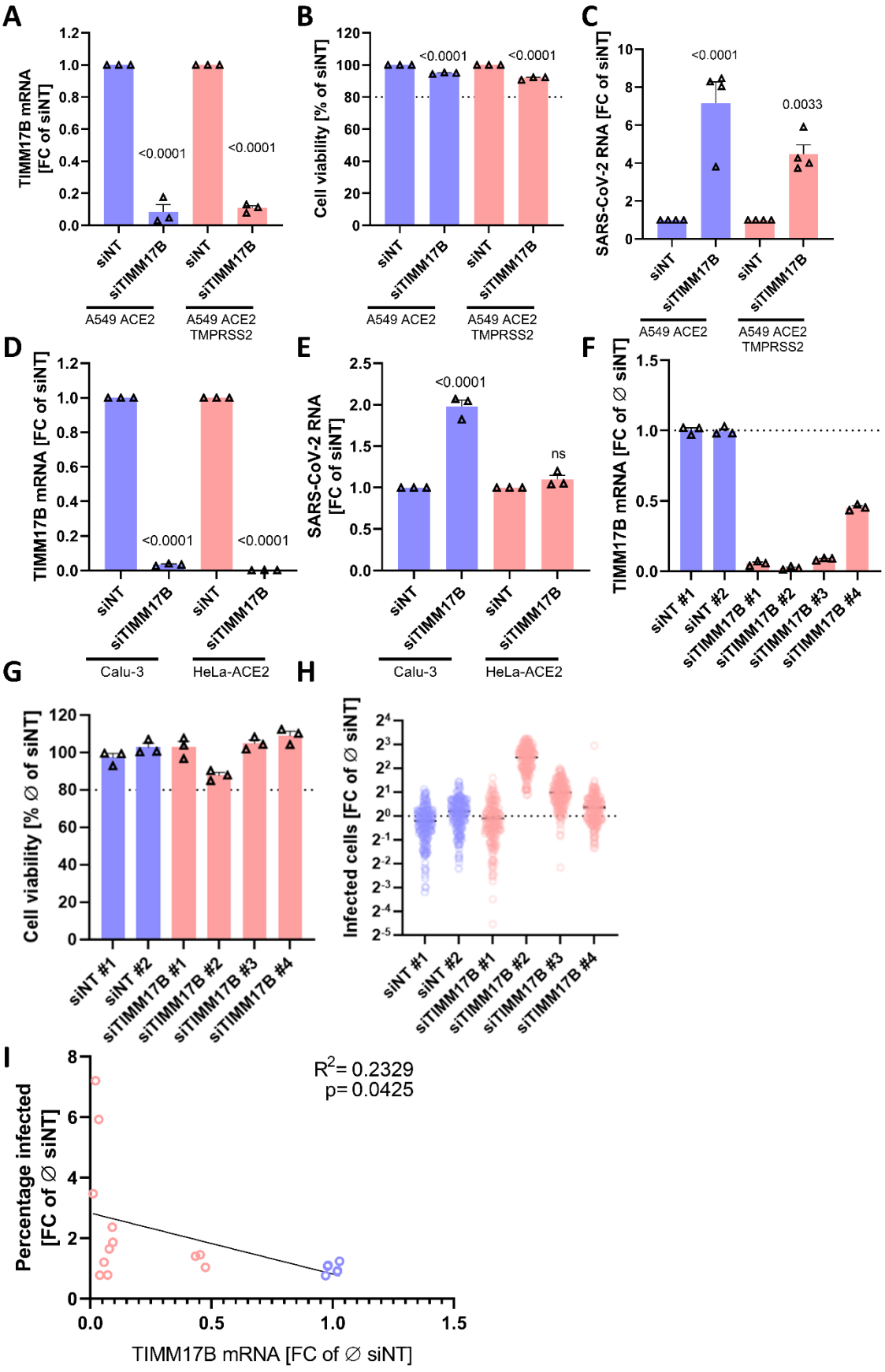

Figure 22: TIMM17B restricts SARS-CoV-2 infection in lung epithelial cells. A549-ACE2 and A549-ACE2-TMPRSS2 cells were transfected with 35 nM TIMM17B-targeting or NT siRNA pools. A) The

knock-down efficiency was determined by RT-qPCR. B) The cell viability of TIMM17B-depleted A549-ACE2 and A549-ACE2-TMPRSS2 cells was determined using the CellTiter-Glo 2.0 kit (Promega). C) The cells were subsequently infected with SARS-CoV-2 BavPat1/2020 (MOI 1). Viral replication in TIMM17B-depleted cells was determined by RT-qPCR against subgenomic Leader-ORF7A RNA as a surrogate of viral replication. To investigate the relevance of TIMM17B for the infection of other cell lines with SARS-CoV-2, I transfected Calu-3 and HeLa-ACE2 cells with 35 nM TIMM17B-targeting or NT siRNA pools. D) The knock-down efficiency was determined by RT-qPCR for both cell lines. E) The cells were subsequently infected with SARS-CoV-2 BavPat1/2020 (MOI 1). SARS-CoV-2 replication was quantified by RT-qPCR against subgenomic Leader-ORF7A RNA. In order to understand the relationship between intracellular TIMM17B levels and SARS-CoV-2 infection, I transfected the single siRNAs that were included in the pools employed for the experiments above into A549-ACE2 cells. F) The knock-down efficiency of each single siRNA was determined by RT-qPCR. G) The effect of the transfection of TIMM17B-targeting or NT siRNAs on the cell viability was determined using the CellTiter-Glo 2.0 kit (Promega). H) At 48 h.p.t. the cells were infected with SARS-CoV-2 BavPat1/2020 (MOI 1). Next, I assessed SARS-CoV-2 infection by anti-N immunostaining with subsequent fluorescence microscopy. The percentage of infected cells was determined using thresholding in CellProfiler 4.2.1 (Broad Institute). I) A regression analysis was employed to test for a potential correlation between TIMM17B expression and the cells' susceptibility to SARS-CoV-2 infection. Error bars represent the SEM. Each symbol in the panels A-G indicates the average results of one independent biological experiment. Each symbol in panel H indicates one analyzed image from N=3 independent experiments. Each symbol in panel I indicates average results of one transfected siRNA (relative TIMM17B expression and SARS-CoV-2 infection) observed in one experimental replicate (N=3 independent experiments were performed). Statistical significance was determined by ordinary one-way ANOVA with Šídák test (A-E). A simple linear regression analysis was performed for the statistical analysis of panel I. FC, fold change.

In order to understand which step of the SARS-CoV-2 life cycle is restricted by TIMM17B, I first tested the impact of TIMM17B depletion at 8 h.p.i. to exclude the possibility of viral spread. Already at this early stage a significant and prominent increase in SARS-CoV-2 infected cells became evident in TIMM17B depleted A549-ACE2 (Figure 23 A, B), suggesting that TIMM17B restricts either entry or replication of SARS-CoV-2. Propagation-deficient VSV pseudotypes encoding GFP were used to investigate a potential antagonism of SARS-CoV-2 entry by TIMM17B. Interestingly, TIMM17B restricted VSVΔG-S entry into A549-ACE2 and A549-ACE2-TMPRSS2 cells but had no impact on the infection of these cells with VSVΔG-G (Figure 23 C). While this indicates a specific restriction of SARS-CoV-2 entry by TIMM17B, the enhancement of SARS-CoV-2 pseudovirus entry in TIMM17B depleted cells was rather moderate (Figure 23 C) when compared to the magnitude of the phenotype observed at 8 h.p.i. (Figure 23 A). This may indicate that additionally to entry, TIMM17B may further restrict SARS-CoV-2 replication.

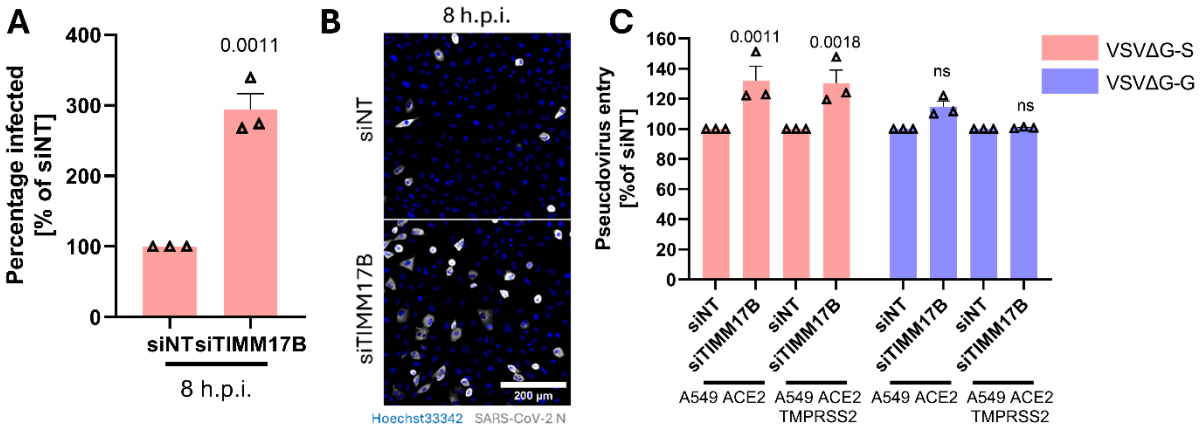

Figure 23: TIMM17B restricts early events of the SARS-CoV-2 life cycle. A) In order to understand if TIMM17B restricts early events of the SARS-CoV-2 life cycle, A549-ACE2 cells were transfected with 35 nM TIMM17B-targeting or NT siRNAs. 48 h.p.t. the cells were infected with SARS-CoV-2 BavPat1/2020 (MOI 5). In order to exclude the possibility of viral spread, the cells were fixed 8 h.p.i. and immunostained against the SARS-CoV-2 N protein. The percentage of infected cells was determined using thresholding of the N signal in CellProfiler 4.2.1 (Broad Institute). B) Representative micrographs of the anti-N immunostaining performed in A. C) In order to investigate whether TIMM17B restricts SARS-CoV-2 entry, propagation-deficient VSV pseudotypes encoding GFP were employed. The pseudovirus was enveloped with the SARS-CoV-2 S protein (VSVΔG-S) or the VSV G protein as a control (VSVΔG-G)[139]. 48 h post siRNA transfection, the A549-ACE2 cells were infected with the pseudoviruses. 24 h.p.i. the cells were fixed and images were recorded using a Celldiscoverer 7 microscope (Zeiss). The percentage of infected cells was determined by thresholding of the GFP signal in CellProfiler 4.2.1 (Broad Institute). Symbols in panels A and C indicate average results of one independent experimental replicate. Statistical significance was determined by unpaired t-test (A) or 2-way ANOVA with Tukey test.

VI. Discussion

VI.1 RAB9A is a host dependency factor for SARS-CoV-2

By integrating the data of two CRISPR/Cas9 loss-of-function screenings that were provided to me at the start of this project with the data of four published CRISPR/Cas9 screenings[77–80], I was able to identify 24 host dependency factor candidates with an expected broad relevance across different cell types and tissues. Amongst these, ACE2, the receptor of SARS-CoV-2[54], had the highest average score which is consistent with the bias of CRISPR/Cas9 screenings to reveal factors involved in viral entry. I selected RAB9A, a small RAS-related GTPase involved in the retrograde transport of proteins from the late endosome to the trans-Golgi network[118,119,124], for functional validation. RAB9A supported SARS-CoV-2 entry into various TMPRSS2-deficient cell lines, that rely on the endocytic uptake of SARS-CoV-2 for infection. Consistently, the promoting effect of RAB9A on SARS-CoV-2 entry was mitigated upon ectopic expression of TMPRSS2, suggesting a predominant involvement of RAB9A in the endocytic entry route. As illustrated in Figure 24, RAB9A did neither impact virion attachment nor ACE2 surface abundance, which was previously shown for a closely related RAB GTPase, RAB7A, that also localizes to the late endosome and was shown to have similar functions as RAB9A[79,168], suggesting that RAB9A supports SARS-CoV-2 infection through a different mode-of action as RAB7A. Instead, RAB9A depletion increased the rate of virus uptake but lead to a retention of internalized virions in the endo-lysosomal compartment. This suggests a regulatory role of RAB9A in the step of membrane fusion between the virion and the late endosome during the endocytic entry of SARS-CoV-2 which was subsequently confirmed by fusion assays employing lentiviral pseudotypes. It was previously suggested that RAB9A regulates the maturation of cathepsin proteases that are required for the proteolytic activation of the S protein during entry[167]. However, I was not able to confirm an involvement of RAB9A in cathepsin trafficking, and hence the acidity-dependent activation of these proteases. In addition, the proviral activity of RAB9A seems to depend on its ability to hydrolyze GTP which is supported by the RAB9A specific GEF DENND2D[122]. The exact mechanism by which RAB9A influences the ability of SARS-CoV-2 to induce membrane fusion remains to be determined, but given the involvement of RAB9A in the biogenesis of the lysosomal compartment, it seems likely that the right composition of the organelle is critical for successful fusion and that depletion of RAB9A disturbs the correct composition of the late endosome.

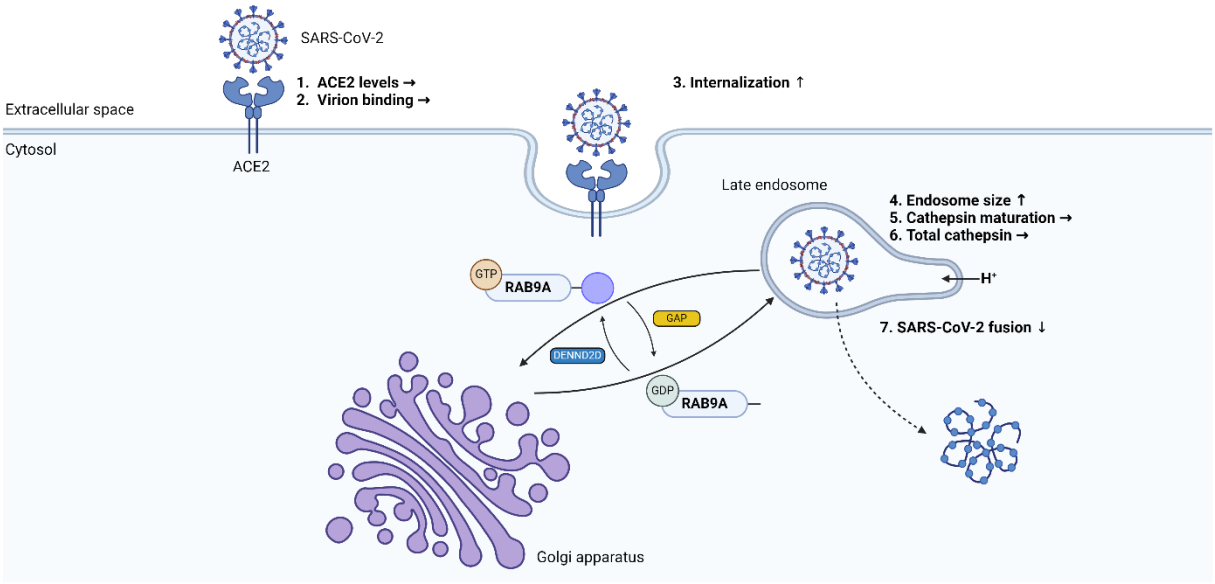

Figure 24: Schematic illustration of the suggested mode-of-action by which RAB9A supports the endocytic entry of SARS-CoV-2. Arrows refer to parameters that are upregulated (↑), downregulated (↓) or unaffected (→) by RAB9A depletion. The schematic was created using BioRender.com.

The available literature on the physiological function of RAB9A is limited. Available studies indicate an involvement of RAB9A in the retrograde transport of proteins from the late endosome to the trans-Golgi network[118,119,124]. RAB9A possesses a C-terminal dual cysteine residue that allows prenylation and insertion into cellular membranes, enabling the protein to traffic vesicles between different organelles[120]. RAB9A seems to act during the biogenesis of endosomes and lysosomes by regulating the organelles homeostasis of cholesterol. Specifically, ectopic RAB9A expression was shown to restore correct cholesterol trafficking in NPC1 deficient cells, which is the essential protein for the extraction of cholesterol from the endosomal membrane during the maturation of endosomes to late endosomes[125,126]. In addition, it was shown that cholesterol accumulations in the late endosomal compartment sequester RAB9A, suggesting a regulation of the endosomal lipid composition by RAB9A, which could in turn influence the efficiency of viral fusion[126].

Choi *et al.* demonstrated that the entry of human papillomavirus is promoted by GDP-bound RAB9A and restricted by its GTP-bound form[127]. Consequently, the depletion of DENND2D, the GEF that is responsible for exchanging GDP to GTP on RAB9A, increased HPV entry[127]. However, the mechanism by which non-enveloped papillomaviruses penetrate endosomal membranes differ greatly from the fusion mechanisms employed by enveloped viruses like SARS-CoV-2[131], which is also exemplified by the use of the RAB9A machinery for the same step of the viral life cycle using a different mode-of-action[127].

RAB9A is the second RAB GTPase that was characterized as a SARS-CoV-2 dependency factor: previously RAB7A, a protein with similar sequence, function and localization was shown to support SARS-CoV-2 entry by promoting ACE2 trafficking to the cell surface[79]. However, in addition to regulating the receptor levels on the plasma membrane, RAB7A is crucial for the correct trafficking and maturation of cathepsins required to proteolytically activate the S protein in the endocytic entry pathway[67,168] which was confirmed during this project. This highlights a second mode-of-action by which RAB7A supports SARS-CoV-2 infection. Furthermore, the correct maturation of cathepsins does not depend on the presence of RAB9A when RAB7A is available to compensate for the depletion of RAB9A[122]. This is in line with my observation that RAB7A depletion increases the intracellular expression of RAB9A which could partially compensate the function that is under normal conditions exercised by RAB7A. The presence of such feedback loops that control the intracellular levels of RAB9A and RAB7A would make these dependency factors reliable targets to support viral entry, since even the loss of one of such factors could enable viral entry to proceed without major restrictions.

Entry of SARS-CoV-2 into lung epithelial cells proceeds predominantly in a TMPRSS2 dependent manner, suggesting that RAB9A does not support the infection of these cells[54]. However, other cell populations have recently been shown to become infected *in vivo* that do not express TMPRSS2 and endocytose SARS-CoV-2 during entry[49,106,171–173]. Human cardiomyocytes have been shown to be susceptible to SARS-CoV-2 infection and replication intermediates have been detected in the myocardium of patients with severe COVID-19, highlighting the relevance of cardiac SARS-CoV-2 infection *in vivo*[49,173]. SARS-CoV-2 entry into human cardiomyocytes can be inhibited by both, the broad-spectrum cathepsin inhibitor E64-d and the lysosomotropic agent bafilomycin A1, but not by the TMPRSS2 inhibitor camostat, suggesting SARS-CoV-2 solely relies on the endocytic entry to infect human cardiomyocytes[171]. In addition to human cardiomyocytes, human monocytes and macrophages can be infected by opsonized SARS-CoV-2 in a FCγR dependent manner, resulting in an abortive replication cycle[106,172]. The entry into these cell populations is efficiently inhibited by treatment with E64-d, suggesting that it depends on cathepsin activity and therefore on the endocytic uptake of virions[106,172]. These findings suggest that the endocytic entry pathway is highly relevant *in vivo* and might be crucial for the development of myocardial complications or a contributing factor to the hyperinflammation that is often observed in severe COVID-19 cases. Moreover, recent virus isolates of the Omicron lineage possess an altered entry pathway preference with a higher tendency to enter cells through the endocytic pathway[174]. The

physiological relevance of this has yet to be determined, but the existence of two distinct entry pathways might be an important feature for the selection of future virus variants, since it could enable SARS-CoV-2 to infect previously non-susceptible cell populations.

In general, RAB GTPases are considered undruggable. The similarity in sequence and structure and complex regulatory mechanisms relying on GAPs, GEFs, adapter proteins (including motor proteins), SNARE proteins, kinases and phosphatases complicate the design of therapeutics targeting one specific RAB GTPase[175]. Another challenge stems from the lack of binding pockets that would allow the targeted design of a compound with high binding affinity to RAB GTPases while the binding affinity to GDP/GTP is extremely high[175]. This results in difficulties designing drugs with higher binding affinities that would allow the compound to compete with GTP. In addition, an inhibition of a RABs GTPase function would likely also target related RAB GTPases and could therefore result in unwanted side effects. A second strategy to inhibit the function of RABs is to interfere with the prenylation of the C-terminal cysteine residues that is required for membrane targeting[176,177]. However, a non-selective inhibition of cytoplasmic farnesyltransferases, the enzymes which execute the prenylation of RABs, would also interfere with the prenylation of many other RAB family members[175]. Nevertheless, it should be noted that some farnesyltransferase inhibitors like lonafarnib and tipifarnib have been shown to possess potent antiviral activity against SARS-CoV-2 which could be mediated by interfering with the function of RAB7A and/or RAB9A[178]. Moreover, many advances have recently been made to facilitate the development of RAB-targeting drugs, which include the elucidation of RAB structures to reveal potential hidden binding pockets that pose attractive targets for drug development[175]. With a high resolution structure of RAB9A now being publicly available, the development of therapeutics that could be potentially used as host-directed antiviral therapies seems now possible[179].

VI.2 TIMM17B restricts SARS-CoV-2 infection

Another factor that was discovered using the meta-analysis described above is TIMM17B, an essential component of the TIM23 complex that mediates the translocation of proteins across the inner mitochondrial membrane[134]. The TIM23 complex is a large protein complex with three essential components: TIM23, TIM17 and TIM50[134]. However, many other proteins have been described to be associated with the TIM23 complex that may possess regulatory functions[132]. The protein complex is embedded into the inner mitochondrial membrane and catalyzes the import of presequence-containing peptides into the mitochondrial matrix[134]. TIM23 seems to be sufficient to form a pore in the inner mitochondrial membrane that lacks the presequence

sensitivity[134,135]. Only in the presence of TIMM17B a physiological TIM23 complex structure containing a twin-pore can be observed, which was shown to depend on the C-terminal domain of TIMM17B[134,136]. In contrast, the N-terminal domain of TIMM17B seems to regulate the voltage gating of the TIM23 complex[134,136]. Therefore it can be postulated that TIMM17B regulates the presequence sensitivity of the mitochondrial import.

Surprisingly, TIMM17B did not support but restrict SARS-CoV-2 infection. It remains unclear why a moderate enrichment of TIMM17B depleted cells was observed in the CRISPR/Cas9 loss-of-function screenings. A potent restriction of SARS-CoV-2 infection was evident in A549-ACE2 and Calu-3 lung epithelial cells expressing TIMM17B which was not the case in HeLa-ACE2 cells, indicating some specificity of this phenotype for lung epithelial cells. While TIMM17B moderately restricts both SARS-CoV-2 entry pathways as evidenced by experiments employing propagation-deficient VSV pseudotypes, the increase in pseudovirus entry seems to be quite limited (~1.4-fold enhancement in TIMM17B depleted cells) when compared to the effect of TIMM17B knock-down on authentic SARS-CoV-2 infection without spread (~3-fold enhancement). This suggests an additional function of TIMM17B in restricting other stages of the viral life cycle such as viral replication that would also become evident in an authentic infection without the possibility of spread. However, further experiments are necessary to illuminate the precise function of TIMM17B during SARS-CoV-2 infection.

The literature provides some information on how TIMM17B might restrict SARS-CoV-2 infection. Intriguingly, significant interactions between SARS-CoV and SARS-CoV-2 ORF7b and TIMM17B were discovered in large interactome studies[180]. This is in line with the predominant mitochondrial localization of ORF7b[181]. The expression of ORF7b seems to induce the production of several proinflammatory cytokines and chemokines, such as IL8, IL11, CXCL1, IL6 and TNF[181,182]. This was shown to induce TNF-dependent apoptosis[181,182]. The relevance of ORF7b for the interferon response is still unclear as conflicting data on the expression of type I interferon and interferon-stimulated genes (e.g. OASL and IFIT1) in ORF7b expressing cells exists[181–184]. One study that reports an inhibition of interferon-β signaling upon ORF7b expression also shows an interaction of ORF7b with MAVS which results in the suppression of downstream signaling cascades[183]. Given the strong interaction between ORF7b and TIMM17B that seems to be conserved between SARS-CoV and SARS-CoV-2, it seems likely that the predominantly mitochondrial localization of ORF7b is mediated by interactions with TIMM17B or MAVS. The detailed mode-of-action by which TIMM17B

restricts SARS-CoV-2 infection and the relevance of ORF7b for this mechanism remain to be elucidated.

VII. References

1. Liu, Y. C., Kuo, R. L. & Shih, S. R. COVID-19: The first documented coronavirus pandemic in history. *Biomedical Journal* vol. 43 Preprint at https://doi.org/10.1016/j.bj.2020.04.007 (2020).

2. Wu, F. *et al.* A new coronavirus associated with human respiratory disease in China. *Nature* **579**, (2020).

3. Markov, P. V. *et al.* The evolution of SARS-CoV-2. *Nature Reviews Microbiology* vol. 21 Preprint at https://doi.org/10.1038/s41579-023-00878-2 (2023).

4. Gorbalenya, A. E. *et al.* The species Severe acute respiratory syndrome-related coronavirus: classifying 2019-nCoV and naming it SARS-CoV-2. *Nature Microbiology* vol. 5 Preprint at https://doi.org/10.1038/s41564-020-0695-z (2020).

5. Drosten, C. *et al.* Identification of a Novel Coronavirus in Patients with Severe Acute Respiratory Syndrome. *New England Journal of Medicine* **348**, (2003).

6. Milne-Price, S., Miazgowicz, K. L. & Munster, V. J. The emergence of the Middle East Respiratory Syndrome coronavirus. *Pathogens and Disease* vol. 71 Preprint at https://doi.org/10.1111/2049-632X.12166 (2014).

7. Delaune, D. *et al.* A novel SARS-CoV-2 related coronavirus in bats from Cambodia. *Nat Commun* **12**, (2021).

8. Zhou, H. *et al.* Identification of novel bat coronaviruses sheds light on the evolutionary origins of SARS-CoV-2 and related viruses. *Cell* **184**, (2021).

9. Wacharapluesadee, S. *et al.* Evidence for SARS-CoV-2 related coronaviruses circulating in bats and pangolins in Southeast Asia. *Nat Commun* **12**, (2021).

10. Murakami, S. *et al.* Detection and Characterization of Bat Sarbecovirus Phylogenetically Related to SARS-CoV-2, Japan. *Emerg Infect Dis* **26**, (2020).

11. Temmam, S. *et al.* Bat coronaviruses related to SARS-CoV-2 and infectious for human cells. *Nature* **604**, (2022).

12. Huang, C. *et al.* Clinical features of patients infected with 2019 novel coronavirus in Wuhan, China. *The Lancet* **395**, (2020).

13. Schindell, B. G., Allardice, M., McBride, J. A. M., Dennehy, B. & Kindrachuk, J. SARS-CoV-2 and the Missing Link of Intermediate Hosts in Viral Emergence - What We Can Learn From Other Betacoronaviruses. *Frontiers in Virology* vol. 2 Preprint at https://doi.org/10.3389/fviro.2022.875213 (2022).

14. Worobey, M. *et al.* The Huanan Seafood Wholesale Market in Wuhan was the early epicenter of the COVID-19 pandemic. *Science (1979)* **377**, (2022).

15. Sparrer, M. N. *et al.* Role of Spillover and Spillback in SARS-CoV-2 Transmission and the Importance of One Health in Understanding the Dynamics of the COVID-19 Pandemic. *Journal of Clinical Microbiology* vol. 61 Preprint at https://doi.org/10.1128/jcm.01610-22 (2023).

16. Xu, R. H. *et al.* Epidemiologic clues to SARS origin in China. *Emerg Infect Dis* **10**, (2004).

17. Zhou, H. *et al.* A Novel Bat Coronavirus Closely Related to SARS-CoV-2 Contains Natural Insertions at the S1/S2 Cleavage Site of the Spike Protein. *Current Biology* **30**, (2020).

18. Zhou, P. *et al.* A pneumonia outbreak associated with a new coronavirus of probable bat origin. *Nature 2020 579:7798* **579**, 270–273 (2020).

19. Yuan, S., Jiang, S. C. & Li, Z. L. Analysis of Possible Intermediate Hosts of the New Coronavirus SARS-CoV-2. *Front Vet Sci* **7**, (2020).

20. CDC Museum COVID-19 Timeline | David J. Sencer CDC Museum | CDC. https://www.cdc.gov/museum/timeline/covid19.html.

21. COVID-19 deaths | WHO COVID-19 dashboard. https://data.who.int/dashboards/covid19/deaths?n=c.

22. Kushwaha, N. D. *et al.* A comprehensive review on the global efforts on vaccines and repurposed drugs for combating COVID-19. *Eur J Med Chem* **260**, 115719 (2023).

23. WHO chief declares end to COVID-19 as a global health emergency | UN News. https://news.un.org/en/story/2023/05/1136367.

24. Wei, W. E. *et al.* Presymptomatic Transmission of SARS-CoV-2 — Singapore, January 23–March 16, 2020. *Morbidity and Mortality Weekly Report* **69**, 411 (2020).

25. V'kovski, P., Kratzel, A., Steiner, S., Stalder, H. & Thiel, V. Coronavirus biology and replication: implications for SARS-CoV-2. *Nature Reviews Microbiology 2020 19:3* **19**, 155–170 (2020).

26. Duval, D. *et al.* Long distance airborne transmission of SARS-CoV-2: rapid systematic review. *BMJ* **377**, (2022).

27. Kutter, J. S. *et al.* SARS-CoV and SARS-CoV-2 are transmitted through the air between ferrets over more than one meter distance. *Nature Communications 2021 12:1* **12**, 1–8 (2021).

28. Manathunga, S. S., Abeyagunawardena, I. A. & Dharmaratne, S. D. A comparison of transmissibility of SARS-CoV-2 variants of concern. *Virol J* **20**, 1–11 (2023).

29. Madewell, Z. J., Yang, Y., Longini, I. M., Halloran, M. E. & Dean, N. E. Household Secondary Attack Rates of SARS-CoV-2 by Variant and Vaccination Status: An Updated Systematic Review and Meta-analysis. *JAMA Netw Open* **5**, e229317 (2022).

30. Shi, P.-Y. *et al.* Spike mutation D614G alters SARS-CoV-2 fitness and neutralization susceptibility. *Res Sq* rs.3.rs-70482 (2020) doi:10.21203/RS.3.RS-70482/V1.

31. Coronavirus disease 2019 (COVID-19) - Complications | BMJ Best Practice US. https://bestpractice.bmj.com/topics/en-us/3000168/complications.

32. Berber, E., Sumbria, D. & Çanakoğlu, N. Meta-analysis and comprehensive study of coronavirus outbreaks: SARS, MERS and COVID-19. *J Infect Public Health* **14**, (2021).

33. Xia, Q. *et al.* Case fatality rates of COVID-19 during epidemic periods of variants of concern: A meta-analysis by continents. *International Journal of Infectious Diseases* **141**, (2024).

34. Luo, X. *et al.* Clinical manifestations of COVID-19: An overview of 102 systematic reviews with evidence mapping. *J Evid Based Med* **15**, 201–215 (2022).

35. Abbasinia, M. *et al.* Clinical Manifestations of Gastrointestinal Symptoms in COVID-19 Patients: An Integrative Review. *Gastroenterol Nurs* **44**, E1–E10 (2021).

36. Parasa, S. *et al.* Prevalence of Gastrointestinal Symptoms and Fecal Viral Shedding in Patients With Coronavirus Disease 2019: A Systematic Review and Meta-analysis. *JAMA Netw Open* **3**, (2020).

37. Guerrero, J. I. *et al.* Central and peripheral nervous system involvement by COVID-19: a systematic review of the pathophysiology, clinical manifestations, neuropathology, neuroimaging, electrophysiology, and cerebrospinal fluid findings. *BMC Infect Dis* **21**, 515 (2021).

38. de Melo, G. D. *et al.* Neuroinvasion and anosmia are independent phenomena upon infection with SARS-CoV-2 and its variants. *Nature Communications 2023 14:1* **14**, 1–14 (2023).

39. Gibson, P. G., Qin, L. & Puah, S. H. COVID-19 acute respiratory distress syndrome (ARDS): clinical features and differences from typical pre-COVID-19 ARDS. *Med J Aust* **213**, 54 (2020).

40. Karakike, E. *et al.* Coronavirus Disease 2019 as Cause of Viral Sepsis: A Systematic Review and Meta-Analysis*. *Crit Care Med* **49**, 2042 (2021).

41. Radivojevic, A. *et al.* A Systematic Review of SARS-CoV-2-Associated Hepatic Dysfunction and the Impact on the Clinical Outcome of COVID-19. *Cureus* **14**, e26852 (2022).

42. Li, G. *et al.* Is liver involvement overestimated in COVID-19 patients? A meta-analysis. *Int J Med Sci* **18**, 1285–1296 (2021).

43. Raina, R. *et al.* Incidence and Outcomes of Acute Kidney Injury in COVID-19: A Systematic Review. *Blood Purif* **51**, 199–212 (2022).

44. Sabatino, J., de Rosa, S., Di Salvo, G. & Indolfi, C. Impact of cardiovascular risk profile on COVID-19 outcome. A meta-analysis. *PLoS One* **15**, e0237131 (2020).

45. Tan, B. K. *et al.* Arterial and venous thromboembolism in COVID-19: a study-level meta-analysis. *Thorax* **76**, 970–979 (2021).

46. Gendron, N. *et al.* Lupus Anticoagulant Single Positivity During the Acute Phase of COVID-19 Is Not Associated With Venous Thromboembolism or In-Hospital Mortality. *Arthritis and Rheumatology* **73**, 1976–1985 (2021).

47. Parotto, M. *et al.* Post-acute sequelae of COVID-19: understanding and addressing the burden of multisystem manifestations. *Lancet Respir Med* **11**, 739–754 (2023).

48. Ranucci, M. *et al.* The procoagulant pattern of patients with COVID-19 acute respiratory distress syndrome. *Journal of Thrombosis and Haemostasis* **18**, 1747–1751 (2020).

49. Lindner, D. *et al.* Association of Cardiac Infection With SARS-CoV-2 in Confirmed COVID-19 Autopsy Cases. *JAMA Cardiol* **5**, 1281–1285 (2020).

50. Xiao, F. *et al.* Evidence for Gastrointestinal Infection of SARS-CoV-2. *Gastroenterology* **158**, 1831 (2020).

51. Gandhi, M. Post-viral sequelae of COVID-19 and influenza. *Lancet Infect Dis* **24**, 218–219 (2024).

52. Bull-Otterson, L. *et al.* Post–COVID Conditions Among Adult COVID-19 Survivors Aged 18–64 and ≥65 Years — United States, March 2020–November 2021. *MMWR Morb Mortal Wkly Rep* **71**, 713–717 (2022).

53. Wang, M. Y. *et al.* SARS-CoV-2: Structure, Biology, and Structure-Based Therapeutics Development. *Front Cell Infect Microbiol* **10**, (2020).

54. Hoffmann, M. *et al.* SARS-CoV-2 Cell Entry Depends on ACE2 and TMPRSS2 and Is Blocked by a Clinically Proven Protease Inhibitor. *Cell* **181**, 271-280.e8 (2020).

55. Jackson, C. B., Farzan, M., Chen, B. & Choe, H. Mechanisms of SARS-CoV-2 entry into cells. *Nature Reviews Molecular Cell Biology 2021 23:1* **23**, 3–20 (2021).

56. Peacock, T. P. *et al.* The furin cleavage site in the SARS-CoV-2 spike protein is required for transmission in ferrets. *Nature Microbiology 2021 6:7* **6**, 899–909 (2021).

57. Zhang, Z. *et al.* Structure of SARS-CoV-2 membrane protein essential for virus assembly. *Nature Communications 2022 13:1* **13**, 1–12 (2022).

58. Cao, Y. *et al.* Characterization of the SARS-CoV-2 E Protein: Sequence, Structure, Viroporin, and Inhibitors. *Protein Sci* **30**, 1114 (2021).

59. Bai, Z., Cao, Y., Liu, W. & Li, J. The SARS-CoV-2 Nucleocapsid Protein and Its Role in Viral Structure, Biological Functions, and a Potential Target for Drug or Vaccine Mitigation. *Viruses* **13**, 1115 (2021).

60. Edalat, F. *et al.* Immunological mechanisms of the nucleocapsid protein in COVID-19. *Scientific Reports 2024 14:1* **14**, 1–9 (2024).

61. Oh, S. J. & Shin, O. S. SARS-CoV-2 Nucleocapsid Protein Targets RIG-I-Like Receptor Pathways to Inhibit the Induction of Interferon Response. *Cells* **10**, 1–13 (2021).

62. Wu, F. *et al.* A new coronavirus associated with human respiratory disease in China. *Nature* **579**, 265 (2020).

63. Zhu, N. *et al.* A Novel Coronavirus from Patients with Pneumonia in China, 2019. *N Engl J Med* **382**, 727 (2020).

64. Wu, C. rong, Yin, W. chao, Jiang, Y. & Xu, H. E. Structure genomics of SARS-CoV-2 and its Omicron variant: drug design templates for COVID-19. *Acta Pharmacologica Sinica 2022 43:12* **43**, 3021–3033 (2022).

65. Zhou, P. *et al.* A pneumonia outbreak associated with a new coronavirus of probable bat origin. *Nature* **579**, 270–273 (2020).

66. Koch, J. *et al.* TMPRSS2 expression dictates the entry route used by SARS-CoV-2 to infect host cells. *EMBO J* **40**, 107821 (2021).

67. Zhao, M. M. *et al.* Cathepsin L plays a key role in SARS-CoV-2 infection in humans and humanized mice and is a promising target for new drug development. *Signal Transduction and Targeted Therapy 2021 6:1* **6**, 1–12 (2021).

68. Yadati, T., Houben, T., Bitorina, A. & Shiri-Sverdlov, R. The Ins and Outs of Cathepsins: Physiological Function and Role in Disease Management. *Cells* **9**, (2020).

69. Dai, W. *et al.* Structure-based design of antiviral drug candidates targeting the SARS-CoV-2 main protease. *Science* **368**, eabb4489 (2020).

70. Shin, D. *et al.* Papain-like protease regulates SARS-CoV-2 viral spread and innate immunity. *Nature* **587**, 657–662 (2020).

71. Schubert, K. *et al.* SARS-CoV-2 Nsp1 binds the ribosomal mRNA channel to inhibit translation. *Nat Struct Mol Biol* **27**, 959–966 (2020).

72. Cortese, M. *et al.* Integrative Imaging Reveals SARS-CoV-2-Induced Reshaping of Subcellular Morphologies. *Cell Host Microbe* **28**, 853-866.e5 (2020).

73. Zimmermann, L. *et al.* SARS-CoV-2 nsp3 and nsp4 are minimal constituents of a pore spanning replication organelle. *Nature Communications 2023 14:1* **14**, 1–12 (2023).

74. Wolff, G. *et al.* A molecular pore spans the double membrane of the coronavirus replication organelle. *Science* **369**, 1395 (2020).

75. Ghosh, S. *et al.* β-Coronaviruses Use Lysosomes for Egress Instead of the Biosynthetic Secretory Pathway. *Cell* **183**, 1520 (2020).

76. Bock, C. *et al.* High-content CRISPR screening. *Nature Reviews Methods Primers 2022 2:1* **2**, 1–23 (2022).

77. Wei, J. *et al.* Genome-wide CRISPR Screens Reveal Host Factors Critical for SARS-CoV-2 Infection. *Cell* **184**, 76-91.e13 (2021).

78. Wang, R. *et al.* Genetic Screens Identify Host Factors for SARS-CoV-2 and Common Cold Coronaviruses. *Cell* **184**, 106-119.e14 (2021).

79. Daniloski, Z. *et al.* Identification of Required Host Factors for SARS-CoV-2 Infection in Human Cells. *Cell* **184**, 92-105.e16 (2021).

80. Schneider, W. M. *et al.* Genome-Scale Identification of SARS-CoV-2 and Pan-coronavirus Host Factor Networks. *Cell* **184**, 120-132.e14 (2021).

81. Hoffmann, H. H. *et al.* Functional interrogation of a SARS-CoV-2 host protein interactome identifies unique and shared coronavirus host factors. *Cell Host Microbe* **29**, 267 (2020).

82. Zhu, Y. *et al.* A genome-wide CRISPR screen identifies host factors that regulate SARS-CoV-2 entry. *Nature Communications 2021 12:1* **12**, 1–11 (2021).

83. Baggen, J. *et al.* Genome-wide CRISPR screening identifies TMEM106B as a proviral host factor for SARS-CoV-2. *Nature Genetics 2021 53:4* **53**, 435–444 (2021).

84. Rebendenne, A. *et al.* Bidirectional genome-wide CRISPR screens reveal host factors regulating SARS-CoV-2, MERS-CoV and seasonal HCoVs. *Nature Genetics 2022 54:8* **54**, 1090–1102 (2022).

85. Grodzki, M. *et al.* Genome-scale CRISPR screens identify host factors that promote human coronavirus infection. *Genome Med* **14**, 1–18 (2022).

86. Biering, S. B. *et al.* Genome-wide bidirectional CRISPR screens identify mucins as host factors modulating SARS-CoV-2 infection. *Nature Genetics 2022 54:8* **54**, 1078–1089 (2022).

87. Israeli, M. *et al.* Genome-wide CRISPR screens identify GATA6 as a proviral host factor for SARS-CoV-2 via modulation of ACE2. *Nat Commun* **13**, 2237 (2022).

88. Chan, K. *et al.* Survival-based CRISPR genetic screens across a panel of permissive cell lines identify common and cell-specific SARS-CoV-2 host factors. *Heliyon* **9**, e12744 (2022).

89. Danziger, O., Patel, R. S., DeGrace, E. J., Rosen, M. R. & Rosenberg, B. R. Inducible CRISPR activation screen for interferon-stimulated genes identifies OAS1 as a SARS-CoV-2 restriction factor. *PLoS Pathog* **18**, e1010464 (2022).

90. Mac Kain, A. *et al.* Identification of DAXX as a restriction factor of SARS-CoV-2 through a CRISPR/Cas9 screen. *Nat Commun* **13**, 2442 (2022).

91. Ugalde, A. P. *et al.* Autophagy-linked plasma and lysosomal membrane protein PLAC8 is a key host factor for SARS-CoV-2 entry into human cells. *EMBO J* **41**, e110727 (2022).

92. Feng, F. *et al.* A CRISPR activation screen identifies genes that enhance SARS-CoV-2 infection. *Protein Cell* **14**, 64–68 (2023).

93. Pagis, A. *et al.* Genome-wide loss-of-function screen using human pluripotent stem cells to study virus-host interactions for SARS-CoV-2. *Stem Cell Reports* **18**, 1766 (2023).

94. Yousefi, M. *et al.* Betacoronaviruses SARS-CoV-2 and HCoV-OC43 infections in IGROV-1 cell line require aryl hydrocarbon receptor. *Emerg Microbes Infect* **12**, 2256416 (2023).

95. Loo, L. *et al.* Fibroblast-expressed LRRC15 is a receptor for SARS-CoV-2 spike and controls antiviral and antifibrotic transcriptional programs. *PLoS Biol* **21**, e3001967 (2023).

96. Bragazzi Cunha, J. *et al.* Type I interferon signaling induces a delayed antiproliferative response in respiratory epithelial cells during SARS-CoV-2 infection. *J Virol* **97**, e01276-23 (2023).

97. Hossain, M. S., Kerkvliet, J. G. & Hoppe, A. D. Whole genome CRISPR screening strategy to identify genes contributing to SARS-CoV-2 spike and VSV-G mediated entry. *J Med Virol* **95**, e29087 (2023).

98. Sakai, M. *et al.* Genome-scale CRISPR-Cas9 screen identifies host factors as potential therapeutic targets for SARS-CoV-2 infection. *iScience* **27**, (2024).

99. Yan, K. *et al.* TMEM106B-mediated SARS-CoV-2 infection allows for robust ACE2-independent infection in vitro but not in vivo. *Cell Rep* **43**, (2024).

100. Frasson, I. *et al.* Identification of druggable host dependency factors shared by multiple SARS-CoV-2 variants of concern. *J Mol Cell Biol* **16**, mjae004 (2024).

101. Steiner, S. *et al.* SARS-CoV-2 biology and host interactions. *Nature Reviews Microbiology 2024 22:4* **22**, 206–225 (2024).

102. Prasad, V. *et al.* Enhanced SARS-CoV-2 entry via UPR-dependent AMPK-related kinase NUAK2. *Mol Cell* **0**, (2023).

103. Baggen, J. *et al.* TMEM106B is a receptor mediating ACE2-independent SARS-CoV-2 cell entry. *Cell* **186**, 3427-3442.e22 (2023).

104. Cantuti-Castelvetri, L. *et al.* Neuropilin-1 facilitates SARS-CoV-2 cell entry and infectivity. *Science (1979)* **370**, (2020).

105. Wang, K. *et al.* CD147-spike protein is a novel route for SARS-CoV-2 infection to host cells. *Signal Transduct Target Ther* **5**, 283 (2020).

106. Junqueira, C. *et al.* FcγR-mediated SARS-CoV-2 infection of monocytes activates inflammation. *Nature 2022 606:7914* **606**, 576–584 (2022).

107. Infante, R. E. *et al.* NPC2 facilitates bidirectional transfer of cholesterol between NPC1 and lipid bilayers, a step in cholesterol egress from lysosomes. *Proc Natl Acad Sci U S A* **105**, 15287–15292 (2008).

108. Klein, Z. A. *et al.* Loss of TMEM106B Ameliorates Lysosomal and Frontotemporal Dementia-Related Phenotypes in Progranulin-Deficient Mice. *Neuron* **95**, 281-296.e6 (2017).

109. Ji, M. *et al.* VMP1 and TMEM41B are essential for DMV formation during β-coronavirus infection. *J Cell Biol* **221**, (2022).

110. Brown, M. S. & Goldstein, J. L. A proteolytic pathway that controls the cholesterol content of membranes, cells, and blood. *Proc Natl Acad Sci U S A* **96**, 11041–11048 (1999).

111. Zhang, S., Wang, J. & Cheng, G. Protease cleavage of RNF20 facilitates coronavirus replication via stabilization of SREBP1. *Proc Natl Acad Sci U S A* **118**, (2021).

112. Lee, S. *et al.* The SARS-CoV-2 RNA interactome. *Mol Cell* **81**, 2838-2850.e6 (2021).

113. Schmidt, N. *et al.* The SARS-CoV-2 RNA-protein interactome in infected human cells. *Nat Microbiol* **6**, 339–353 (2021).

114. Murigneux, E. *et al.* Proteomic analysis of SARS-CoV-2 particles unveils a key role of G3BP proteins in viral assembly. *Nature Communications 2024 15:1* **15**, 1–17 (2024).

115. Flynn, R. A. *et al.* Discovery and functional interrogation of SARS-CoV-2 RNA-host protein interactions. *Cell* **184**, 2394-2411.e16 (2021).

116. Labeau, A. *et al.* Characterization and functional interrogation of the SARS-CoV-2 RNA interactome. *Cell Rep* **39**, (2022).

117. Homma, Y., Hiragi, S. & Fukuda, M. Rab family of small GTPases: an updated view on their regulation and functions. *FEBS J* **288**, 36 (2021).

118. Barbero, P., Bittova, L. & Pfeffer, S. R. Visualization of Rab9-mediated vesicle transport from endosomes to the trans-Golgi in living cells. *J Cell Biol* **156**, 511–518 (2002).

119. Lombardi, D. *et al.* Rab9 functions in transport between late endosomes and the trans Golgi network. *EMBO J* **12**, 677–682 (1993).

120. Soldati, T., Shapiro, A. D., Dirac Svejstrup, A. B. & Pfefffer, S. R. Membrane targeting of the small GTPase Rab9 is accompanied by nucleotide exchange. *Nature 1994 369:6475* **369**, 76–78 (1994).

121. Pfeffer, S. & Aivazian, D. Targeting Rab GTPases to distinct membrane compartments. *Nat Rev Mol Cell Biol* **5**, 886–896 (2004).

122. Yoshimura, S. I., Gerondopoulos, A., Linford, A., Rigden, D. J. & Barr, F. A. Family-wide characterization of the DENN domain Rab GDP-GTP exchange factors. *Journal of Cell Biology* **191**, 367–381 (2010).

123. Riederer, M. A., Soldati, T., Shapiro, A. D., Lin, J. & Pfeffer, S. R. Lysosome biogenesis requires Rab9 function and receptor recycling from endosomes to the trans-Golgi network. *J Cell Biol* **125**, 573–582 (1994).

124. Ganley, I. G., Carroll, K., Bittova, L. & Pfeffer, S. Rab9 GTPase regulates late endosome size and requires effector interaction for its stability. *Mol Biol Cell* **15**, 5420–5430 (2004).

125. Walter, M., Chen, F. W., Tamari, F., Wang, R. & Ioannou, Y. A. Endosomal lipid accumulation in NPC1 leads to inhibition of PKC, hypophosphorylation of vimentin and Rab9 entrapment. *Biol Cell* **101**, 141–153 (2009).

126. Ganley, I. G. & Pfeffer, S. R. Cholesterol accumulation sequesters Rab9 and disrupts late endosome function in NPC1-deficient cells. *J Biol Chem* **281**, 17890–17899 (2006).

127. Choi, J. & DiMaio, D. Noncanonical Rab9a action supports retromer-mediated endosomal exit of human papillomavirus during virus entry. *PLoS Pathog* **19**, (2023).

128. A, L. *et al.* Genome-wide siRNA screen identifies the retromer as a cellular entry factor for human papillomavirus. *Proc Natl Acad Sci U S A* **110**, 7452–7457 (2013).

129. G, S. *et al.* Human genome-wide RNAi screen reveals a role for nuclear pore proteins in poxvirus morphogenesis. *Proc Natl Acad Sci U S A* **110**, 3519–3524 (2013).

130. CM, F. *et al.* The master regulator of the cellular stress response (HSF1) is critical for orthopoxvirus infection. *PLoS Pathog* **10**, (2014).

131. Winter, S. L. & Chlanda, P. The Art of Viral Membrane Fusion and Penetration. *Subcell Biochem* **106**, 113–152 (2023).

132. Schmidt, O., Pfanner, N. & Meisinger, C. Mitochondrial protein import: from proteomics to functional mechanisms. *Nature Reviews Molecular Cell Biology 2010 11:9* **11**, 655–667 (2010).

133. Chaudhuri, M. *et al.* Tim17 Updates: A Comprehensive Review of an Ancient Mitochondrial Protein Translocator. *Biomolecules* **10**, 1643 (2020).

134. Demishtein-Zohary, K. & Azem, A. The TIM23 mitochondrial protein import complex: function and dysfunction. *Cell Tissue Res* **367**, 33–41 (2017).

135. Truscott, K. N. *et al.* A J-protein is an essential subunit of the presequence translocase–associated protein import motor of mitochondria. *J Cell Biol* **163**, 707 (2003).

136. Martinez-Caballero, S., Grigoriev, S. M., Herrmann, J. M., Campo, M. L. & Kinnally, K. W. Tim17p regulates the twin pore structure and voltage gating of the mitochondrial protein import complex TIM23. *Journal of Biological Chemistry* **282**, 3584–3593 (2007).

137. Fielden, L. F. *et al.* Central role of Tim17 in mitochondrial presequence protein translocation. *Nature 2023 621:7979* **621**, 627–634 (2023).

138. Henkel, L., Rauscher, B., Schmitt, B., Winter, J. & Boutros, M. Genome-scale CRISPR screening at high sensitivity with an empirically designed sgRNA library. *BMC Biol* **18**, 1–21 (2020).

139. Zettl, F. *et al.* Rapid Quantification of SARS-CoV-2-Neutralizing Antibodies Using Propagation-Defective Vesicular Stomatitis Virus Pseudotypes. *Vaccines (Basel)* **8**, 1–13 (2020).

140. Nakabayashi, H., Taketa, K., Miyano, K., Yamane, T. & Sato, J. Growth of human hepatoma cells lines with differentiated functions in chemically defined medium . *Cancer Res.* **42**, 3858–3863 (1982).

141. Benning, L. *et al.* Neutralizing antibody response against the B.1.617.2 (delta) and the B.1.1.529 (omicron) variants after a third mRNA SARS-CoV-2 vaccine dose in kidney transplant recipients. *American Journal of Transplantation* **22**, 1873 (2022).

142. Stirling, D. R. *et al.* CellProfiler 4: improvements in speed, utility and usability. *BMC Bioinformatics* **22**, 1–11 (2021).

143. Stirling, D. R., Carpenter, A. E. & Cimini, B. A. CellProfiler Analyst 3.0: accessible data exploration and machine learning for image analysis. *Bioinformatics* **37**, 3992–3994 (2021).

144. Ritter, C. *et al.* Multi-Channel Colocalization Analysis and Visualization of Viral Proteins in Fluorescence Microscopy Images. *IEEE Access* **11**, (2023).

145. Berg, S. *et al.* ilastik: interactive machine learning for (bio)image analysis. *Nature Methods 2019 16:12* **16**, 1226–1232 (2019).

146. Bolte, S. & Cordelières, F. P. A guided tour into subcellular colocalization analysis in light microscopy. *J Microsc* **224**, 213–232 (2006).

147. Li, W. *et al.* MAGeCK enables robust identification of essential genes from genome-scale CRISPR/Cas9 knockout screens. *Genome Biol* **15**, 554 (2014).

148. R Core Team. R: A language and environment for statistical computing. Preprint at (2021).

149. Korotkevich, G. *et al.* Fast gene set enrichment analysis. *bioRxiv* 060012 (2021) doi:10.1101/060012.

150. Wickham, H. *et al.* Welcome to the Tidyverse. *J Open Source Softw* **4**, 1686 (2019).

151. Hart, T. *et al.* High-Resolution CRISPR Screens Reveal Fitness Genes and Genotype-Specific Cancer Liabilities. *Cell* **163**, 1515–1526 (2015).

152. Wüst, S., Schad, P., Burkart, S. & Binder, M. Comparative analysis of six IRF family members in alveolar epithelial cell-intrinsic antiviral responses. *Cells* **10**, (2021).

153. Eckhardt, M. *et al.* A SNAP-tagged derivative of HIV-1-A versatile tool to study virus-cell interactions. *PLoS One* **6**, (2011).

154. Henkel, L., Rauscher, B., Schmitt, B., Winter, J. & Boutros, M. Genome-scale CRISPR screening at high sensitivity with an empirically designed sgRNA library. *BMC Biol* **18**, 1–21 (2020).

155. Rebendenne, A. *et al.* Bidirectional genome-wide CRISPR screens reveal host factors regulating SARS-CoV-2, MERS-CoV and seasonal HCoVs. *Nature Genetics 2022 54:8* **54**, 1090–1102 (2022).

156. Zárate, S., Romero, P., Espinosa, R., Arias, C. F. & López, S. VP7 Mediates the Interaction of Rotaviruses with Integrin αvβ3 through a Novel Integrin-Binding Site. *J Virol* **78**, 10839 (2004).

157. Vermeire, J. *et al.* Quantification of Reverse Transcriptase Activity by Real-Time PCR as a Fast and Accurate Method for Titration of HIV, Lenti- and Retroviral Vectors. *PLoS One* **7**, (2012).

158. Sid Ahmed, S. *et al.* An Environmental Restriction impairs HIV-1 virion fusion and triggers innate immune recognition. doi:10.1101/2023.11.22.568261.

159. M, H. *et al.* SARS-CoV-2 Cell Entry Depends on ACE2 and TMPRSS2 and Is Blocked by a Clinically Proven Protease Inhibitor. *Cell* **181**, 271-280.e8 (2020).

160. Collins, M. P. & Forgac, M. Regulation and function of V-ATPases in physiology and disease. *Biochimica et Biophysica Acta - Biomembranes* vol. 1862 Preprint at https://doi.org/10.1016/j.bbamem.2020.183341 (2020).

161. Yadati, T., Houben, T., Bitorina, A. & Shiri-Sverdlov, R. The Ins and Outs of Cathepsins: Physiological Function and Role in Disease Management. *Cells* **9**, (2020).

162. Stenmark, H. Rab GTPases as coordinators of vesicle traffic. *Nature Reviews Molecular Cell Biology 2009 10:8* **10**, 513–525 (2009).

163. Delorey, T. M. *et al.* COVID-19 tissue atlases reveal SARS-CoV-2 pathology and cellular targets. *Nature 2021 595:7865* **595**, 107–113 (2021).

164. F, Z. *et al.* Rapid Quantification of SARS-CoV-2-Neutralizing Antibodies Using Propagation-Defective Vesicular Stomatitis Virus Pseudotypes. *Vaccines (Basel)* **8**, 1–13 (2020).

165. Clausen, T. M. *et al.* SARS-CoV-2 Infection Depends on Cellular Heparan Sulfate and ACE2. *Cell* **183**, 1043-1057.e15 (2020).

166. Zerial, M. & McBride, H. Rab proteins as membrane organizers. *Nat Rev Mol Cell Biol* **2**, 107–117 (2001).

167. Díaz-Salinas, M. A., Silva-Ayala, D., López, S. & Arias, C. F. Rotaviruses Reach Late Endosomes and Require the Cation-Dependent Mannose-6-Phosphate Receptor and the Activity of Cathepsin Proteases To Enter the Cell. *J Virol* **88**, 4389 (2014).

168. Homma, Y. *et al.* Comprehensive knockout analysis of the Rab family GTPases in epithelial cells. *J Cell Biol* **218**, 2035 (2019).

169. Xu, C. *et al.* Human defensins inhibit SARS-CoV-2 infection by blocking viral entry. *Viruses* **13**, (2021).

170. Cavrois, M., De Noronha, C. & Greene, W. C. A sensitive and specific enzyme-based assay detecting HIV-1 virion fusion in primary T lymphocytes. *Nat Biotechnol* **20**, (2002).

171. Bermejo, J. A. P. *et al.* SARS-CoV-2 infection of human iPSC derived cardiac cells reflects cytopathic features in hearts of patients with COVID-19. *Sci Transl Med* **13**, (2021).

172. Jalloh, S. *et al.* CD169-mediated restrictive SARS-CoV-2 infection of macrophages induces proinflammatory responses. *PLoS Pathog* **18**, (2022).

173. Bojkova, D. *et al.* SARS-CoV-2 infects and induces cytotoxic effects in human cardiomyocytes. *Cardiovasc Res* **116**, (2020).

174. Zhao, H. *et al.* SARS-CoV-2 Omicron variant shows less efficient replication and fusion activity when compared with Delta variant in TMPRSS2-expressed cells. *Emerg Microbes Infect* **11**, 277–283 (2022).

175. Yin, G. *et al.* Targeting small GTPases: emerging grasps on previously untamable targets, pioneered by KRAS. *Signal Transduction and Targeted Therapy 2023 8:1* **8**, 1–39 (2023).

176. Okamoto, S. *et al.* Zoledronic acid induces apoptosis and S-phase arrest in mesothelioma through inhibiting Rab family proteins and topoisomerase II actions. *Cell Death Dis* **5**, (2014).

177. Roelofs, A. J. *et al.* Selective inhibition of Rab prenylation by a phosphonocarboxylate analogue of risedronate induces apoptosis, but not S-phase arrest, in human myeloma cells. *Int J Cancer* **119**, 1254–1261 (2006).

178. Weber, L. *et al.* Effect of farnesyltransferase inhibitors on SARS-CoV-2. *J Glob Antimicrob Resist* **32**, 164 (2023).

179. Chen, L. *et al.* High resolution crystal structure of human Rab9 GTPase. A novel antiviral drug target. *Journal of Biological Chemistry* **279**, 40204–40208 (2004).

180. Stukalov, A. *et al.* Multilevel proteomics reveals host perturbations by SARS-CoV-2 and SARS-CoV. *Nature 2021 594:7862* **594**, 246–252 (2021).

181. García-García, T. *et al.* Impairment of antiviral immune response and disruption of cellular functions by SARS-CoV-2 ORF7a and ORF7b. *iScience* **25**, 105444 (2022).

182. Yang, R. *et al.* SARS-CoV-2 Accessory Protein ORF7b Mediates Tumor Necrosis Factor-α-Induced Apoptosis in Cells. *Front Microbiol* **12**, 654709 (2021).

183. Xiao, X. *et al.* Inhibition of the RLR signaling pathway by SARS-CoV-2 ORF7b is mediated by MAVS and abrogated by ORF7b-homologous interfering peptide. *J Virol* **98**, e01573-23 (2024).

184. Shemesh, M. *et al.* SARS-CoV-2 suppresses IFNβ production mediated by NSP1, 5, 6, 15, ORF6 and ORF7b but does not suppress the effects of added interferon. *PLoS Pathog* **17**, (2021).

VIII. Publications and conference contributions

VIII.1 Publications

Meta-analysis of genome-wide CRISPR screenings reveals host dependency and restriction factors of the SARS-CoV-2 replication cycle

Y. Stahl*, B. Cerikan, F. Heigwer, L. Henkel, S. Denolly, S. Sid Ahmed, V. Prasad, H. Kim, O. T. Fackler, M. Boutros, R. Bartenschlager*

Manuscript in preparation

RAR/RXR pathway inhibition disrupts SARS-CoV-2 infection in hiPS-derived cardiomyocytes

M. Bencun, ***Y. Stahl****, E. Boileau, L. Spreyer, J. Eschenbach, R. Bartenschlager, C. Dieterich*

Manuscript in preparation

Contribution: Validation and characterization of RXRA as a SARS-CoV-2 dependency factor in hiPS-derived cardiomyocytes.

An orally efficacious coronavirus assembly inhibitor that targets the viral M protein

M. Laporte, D. Jochmans, D. Bardiot, L. Desmarets, O. Debski-Antoniak, G. Mizzon, R. Abdelnabi, P. Leyssen, W. Chiu, Z. Zhang, N. Nomura, S. Boland, U. Ohto, ***Y. Stahl****, J. Wuyts, S. De Jonghe, A. Stevaert, M. van Hemert, B. Bontes, P. Wanningen, G. J. M. Groenewold, A. Zegar, K. Owczarek, S. Joshi, M. Koukni, P. Arzel, H. Klaassen, N. Cremers, K. Donckers, T. Francken, T. Van Buyten, J. Rymenants, J. Schepers, K. Pyrc, R. Hilgenfeld, J. Dubuisson, B.-J. Bosch, F. van Kuppeveld, C. Eydoux, E. Decroly, B. Canard, L. Naesens, E. Snijder, S. Belouzard, T. Shimizu, R. Bartenschlager, D. Hurdiss, A. Marchand, P. Chaltin, I. Vandecaetsbeek, B. Weynand, J.-C. Vanherck, J. Neyts*

Nature, accepted for publication

Contribution: Infection of A549-ACE2-TMPRSS2 cells (treated with CIM-834 or DMSO) with SARS-CoV-2 BavPat1/2020 for the analysis of DMV formation and virion assembly by electron microscopy and electron tomography.

Enhanced SARS-CoV-2 entry via UPR-dependent AMPK-related kinase NUAK2

V. Prasad, B. Cerikan, ***Y. Stahl****, K. Kopp, V. Magg, N. Acosta-Rivero, H. Kim, K. Klein, C. Funaya, U. Haselmann, M. Cortese, F. Heigwer, J. Bageritz, D. Bitto, S. Jargalsaikhan, C. Neufeldt, F. Pahmeier, M. Boutros, Y. Yamauchi, A. Ruggieri, R. Bartenschlager*

Molecular Cell, 83(14), 2559–2577.e8, https://doi.org/10.1016/j.molcel.2023.06.020

Contribution: Functional validation of the importance of NUAK2 for SARS-CoV-2 infection and coronavirus entry and determination of antiviral properties of the NUAK2 inhibitor WZ-4003.

Convergent use of phosphatidic acid for hepatitis C virus and SARS-CoV-2 replication organelle formation

*K. Tabata, V. Prasad, D. Paul, J.-Y. Lee, M.-T. Pham, W.-I. Twu, C. Neufeldt, M. Cortese, B. Cerikan****, Y. Stahl****, S. Joecks, C. S. Tran, C. Lüchtenborg, P. V'kowski, K. Hör,amm, A. C. Müller, C. Zitzmann, U. Haselmann, J. Beneke, L. Kerdali, H.Erfle, V. Thiel, V. Lohmann, G. Superti-Furga, B. Brügger, R. Bartenschlager*

Nature Communications 12, 7276, 2021, https://doi.org/10.1038/s41467-021-27511-1

Contribution: Establishment and validation of a VSV pseudovirus system allowing the quantification of SARS-CoV-2 entry.

VIII.2 Presentations and conference contributions

Meta-analysis of CRISPR screens reveals RAB9A as a factor involved in SARS-CoV-2 entry

***Y. Stahl**, B. Cerikan, F. Heigwer, L. Henkel, S. Denolly, V. Prasad, H. Kim, M. Boutros, R. Bartenschlager*

33rd Annual Meeting of the Society for Virology, Vienna, Austria, 2024

Oral presentation

Meta-analysis of genome-wide CRISPR screens reveals RAB9A as a SARS-CoV-2 entry factor

***Y. Stahl**, B. Cerikan, F. Heigwer, L. Henkel, S. Denolly, V. Prasad, H. Kim, M. Boutros, R. Bartenschlager*

8th European Congress of Virology, Gdansk, Poland, 2023

Poster presentation